2011-07-21

Innovative Methods to Determine Material Properties of Cartilaginous Tissues and Application for Tissue Engineering

Tai-Yi Yuan
University of Miami, taiyiyuan@gmail.com

UNIVERSITY OF MIAMI

INNOVATIVE METHODS TO DETERMINE MATERIAL PROPERTIES OF
CARTILAGINOUS TISSUES AND APPLICATION FOR TISSUE ENGINEERING

By

Tai-Yi Yuan

A DISSERTATION

Submitted to the Faculty
of the University of Miami
in partial fulfillment of the requirements for
the degree of Doctor of Philosophy

Coral Gables, Florida

August 2011

UNIVERSITY OF MIAMI

A dissertation submitted in partial fulfillment of
the requirements for the degree of
Doctor of Philosophy

INNOVATIVE METHODS TO DETERMINE MATERIAL PROPERTIES OF
CARTILAGINOUS TISSUES AND APPLICATION FOR TISSUE ENGINEERING

Tai-Yi Yuan

Approved:

_____
Weiyong Gu, Ph.D.
Professor of Biomedical
Engineering

_____
Terri A. Scandura, Ph.D.
Dean of the Graduate School

_____
Chun-Yuh Huang, Ph.D.
Assistant Professor of Biomedical
Engineering

_____
Jorge Bohorquez, Ph.D.
Assistant Professor of
Professional of Biomedical
Engineering

_____
Fotios Andreopoulos, Ph.D.
Associate Professor of Biomedical
Engineering

_____
Xiangyang Zhou, Ph.D.
Assistant Professor of
Mechanical and Aerospace
Engineering

YUAN, TAI-YI   (Ph.D., Biomedical Engineering)

<u>Innovative Methods to Determine Material Properties</u>   (August 2011)
<u>of Cartilaginous Tissues and Application</u>
<u>for Tissue Engineering</u>

Abstract of a dissertation at the University of Miami.

Dissertation supervised by Professor Weiyong Gu.
No. of pages in text. (152)

Low back pain is one of the major health concerns in the US. It affects up to 80% of the population at some time during their lives. It not only causes discomfort to patients and affects their physical ability but also has a huge economic impact on society. Although the cause of low back pain is still poorly understood, it is implicated that degeneration of the intervertebral disc is the primary factor.

Currently, researchers are trying to use tissue engineering approaches to develop new treatments capable of removing the degenerated disk and replacing it with a biological substitute. However, to create such a biological substitute, we need to first understand the structure-function relationship of the tissue. Only when we understand the function of the tissue, can we begin creating biological substitutes. While culturing a biological substitute, we also need methods to determine how the substitute responds to its environment. At present, there are many different types of bioreactors developed for cartilaginous tissues. However, there is a lack of a system that can detect the chemical, electrical and mechanical response noninvasively with control feedback in real-time. It is hard to provide the optimal culture environment to the substitute without knowing its response in real-time.

The objective of this dissertation is to develop new methods to investigate the transport property, oxygen consumption rate and mechano-electrochemical and mechanical properties of the tissue. Because cells are responsible for the tissue health, it is necessary to understand how they can obtain nutrients under different environments, e.g. under different loading condition. In addition, with the use of a bioreactor with the capability of detecting the real-time response combined with a feedback control system, we can provide the most favorable conditions for tissue or biological substitutes to grow.

The new measurement methods developed in this dissertation can contribute to further understanding the function of the tissue. The methods outlined in this dissertation can also provide new tools for future tissue engineering applications. Moreover, the findings in this dissertation can provide information for developing a more comprehensive theoretical model to elucidate the etiology of disc degeneration.

Acknowledgements

I have to thank a lot of people for helping me to accomplish something that I have been working towards for many years.

I am extremely grateful for my parents and family. I would never have been able to do this without their support and love. I cannot put in words how much I appreciate and love them. I have to thank my high school teacher, Chienp Chen, and his family. They treat me and love me just like their own family. Thanks to Dr. Gu, for teaching me not only things in school but lessons in life, even though I may have disappointed him many times. Dr. Huang, I have to thank you for teaching me and guiding me with patience, and also thank you for introducing me to a whole new field. Thanks to Dr. Andreopoulos, Dr. Bohorquez and Dr. Zhou for their support and guidance. Dr. Yao, thanks for your friendship and your support. Thanks to Madge for her support and friendship over the years. Thanks to Alicia for her support and help through some difficult times. Thanks to Andre for his help and keep me laughing all the time. Thanks to Peter for being a great roommate and friend. Thanks to Hanan for her friendship and help. I really wish I could have known you earlier, you are a great friend. Thanks to Ben, Daniel, Daniela, Edith, Erdem, Francesco, Jessica, Nelson, Nuri, Pedro, Qian, Ray, Selma, Taka, Terry, Vida and Yesy for their support and help. I am thankful to know each one of you, and you make me a better person.

I also want to thank one of the most important people in my life, Seven. It is my honor to know you, and I will always remember you even though you are gone.

TABLE OF CONTENTS

LIST OF FIGURES

LIST OF TABLES

CHAPTER 1. GENERAL INTRODUCTION

1.1 INTRODUCTION

Low back pain is one of the major public health problems in the United States (NIH, 1997). It is estimated that "In the United States, people spend almost $50 billion on back pain every year" (National Institutes of Health., 2004). It is widely accepted that almost every person will experience some symptom or variety of back pain during his or her lifetime, regardless of sex. More than seventy percent of people have experienced back pain at some time in their life, with the annual prevalence of back pain ranging from fifteen to forty-five percent. Studies have indicated that the populations between ages 30 to 50 are the most prone to lower back pain. Moreover, back pain is the most frequent cause of activity limitation in people below 45 years of age and is a common reason for visiting a health care provider (Kelsey et al., 1978; Kelsey and White, 1980; Kelsey et al., 1979; NIH, 1997; Kelsey et al., 1992).

Among the causes of lower back pain (LBP) are herniated discs, spinal stenosis, skeletal irregularities, and others. While most incidents of LBP are ignored or unreported, doctors often examine patients through physical and blood tests. Physicians also diagnose LBP using modern technology equipment such as X-ray imaging, discography, computerized tomography (CT), Magnetic resonance imaging (MRI), electrodiagnostic procedures, bone scans, and ultrasound imaging. Although treatment choices and procedures have improved over time, causes of LBP are still poorly understood (Deyo, 1998).

Nonetheless, while the exact cause of low back pain is still unclear, scientists and physicians have reached a popular assumption that its cause can be primarily traced to the

degeneration of the intervertebral disc (Eyre et al., 1989; Acaroglu et al., 1995; Buckwalter, 1995; Gruber and Hanley, Jr., 2002; Kelsey et al., 1992; Kelsey et al., 1978; Kelsey and White, 1980; Kelsey et al., 1979; Nerlich et al., 1998; White, 1981; White and Panjabi, 1978). The intervertebral disc (IVD) is the largest avascular cartilaginous tissue in the human body. As a result, nutrient supply into the IVD is mainly through diffusion of small solutes from the peripheral blood vessels (Urban et al., 1978; Maroudas, 1975; Urban et al., 1982). Therefore, it is imperative to understand the transport property (i.e., diffusivity) of small molecules (i.e., oxygen) within the tissue.

IVDs, like most tissues, lack the ability to self-repair and restore original function after damage due to injury or disease. Conventionally, prescription medications and even surgery have been used to reinstate tissue functions to their pre-injury status. Injecting healthy cells into damaged organs or replacing the injured tissue with properly engineered constructs are alternative ways of restoring organ function. Hence, the definition of tissue engineering or regenerative medicine is 'an interdisciplinary field that applies the principles of engineering and life sciences toward the development of biological substitutes for the repair or regeneration of tissue or organ function' (Nerem, 1991; Arosarena, 2005; Skalak Richard and Fox C.Fred, 1988).

These substitutes possess similar biochemical activity, microstructure, mechanical integrity and biostability to the original tissues or organs (Portner et al., 2005; Langer and Vacanti, 1993). These substitutes have to be cultivated under conditions that are close to the original environments of organs. Bioreactors are devices which enable control of desired environments (e.g., environment within the body) for engineered tissues, or constructs, to grow. The conditions (e.g., pH, temperature, oxygen tension, nutrient

supply and waste removal) inside the bioreactors are well controlled to ensure constructs are well cultivated (Portner et al., 2005; Martin et al., 2004; Darling and Athanasiou, 2003; Concaro et al., 2009; Marsano et al., 2006; Wendt et al., 2003; Bancroft et al., 2003; Freed et al., 1998; LeBaron and Athanasiou, 2000; Mahmoudifar and Doran, 2005). Engineered tissues and constructs in the bioreactors need to be constantly monitored (e.g. water content and proteoglycan content) in order to assess their growth. Furthermore, the environments within the bioreactors can be adjusted to different conditions depending on the engineered constructs growth.

In order to grow appropriate engineered constructs to replace injured or degenerated tissue, we need to first understand the structure-function relationship of native tissue. It is important to know this relationship, so we can create similar biological substitutes. Current methods to evaluate the engineered tissue growth usually require extra samples. Samples are generally devastated by chemical assays or mechanical assessment in order to determine tissue properties. Therefore, in this dissertation, new measurement methods were proposed to investigate tissue properties and to determine physicochemical signals within the tissue noninvasively and in real-time.

1.2 SPECIFIC AIMS

The ultimate goal of this research is to elucidate tissue degeneration and using the engineering approaches to create biological substitutes. The focus of this dissertation is on the development of new measurement methods in order to accomplish this ultimate goal. In particular, the specific aims of this dissertation are:

- To design and construct an oxygen diffusion chamber to determine the transport property (oxygen diffusivity) in IVD tissues.

- To design and construct an oxygen metabolism chamber to determine the oxygen consumption rate in IVD cells.

- To design and construct a novel measurement system to online-characterize the mechano-electrochemical properties of the cartilaginous tissues and engineered tissues.

- To design and construct a loading apparatus in order to determine the mechanical property of the tissue.

1.3 SIGNIFICANCE OF THIS STUDY

The goal of tissue engineering is to create biological substitutes to replace degenerated tissue. Before creating biological substitutes, we first have to understand IVD tissue structure and function. Only after understanding the fundamental structure-function relationship can we develop effective biological substitutes for the IVD. Therefore, the objective of this dissertation is to develop new measuring methods to facilitate investigating IVD tissue properties and also to determine tissue properties noninvasively and in real time.

What makes the IVD a unique structure is its matrix. However, cells within the IVD are the most important component because they produce and maintain the matrix. Since cells require nutrient supply in order to survive, it is crucial to understand how cells obtain nutrients. Due to the unique composition and structure of the matrix and the complexity of the mechano-electrochemical coupling phenomena in IVD tissues, there is a lack of knowledge on transport properties of human IVDs. For instance, one does not know how mechanical stress affects nutrient transport mechanisms. Therefore, in Chapter 3, a measuring technique is proposed to determine the transport properties of IVD tissue.

One of the causes of disc degeneration is thought to be poor nutrition. Because of the avascular character of IVDs, cells rely on diffusion to obtain nutrients. However, rates of nutrient consumption are high compared to rates of diffusion through the matrix. Cells in the center of the IVD obtain less nutrients than the cells in the periphery (Bibby et al., 2005). Therefore, it is important to understand how cells respond to the low nutrient condition. Thus, in Chapter 4, a new method is developed to measure the oxygen consumption rate of IVD cells under low glucose concentrations.

Knowledge of mechano-electrochemical signals is essential for understanding mechanotransduction mechanisms such as tissue growth, nutrition, and degeneration of cartilaginous tissues under physical forces. It is important to develop a measurement method to study these mechano-electrochemical signals noninvasively and in real-time. Conventionally, tissues or engineered constructs have to be removed from bioreactors at various time points (e.g., one week, two weeks, one months, or three months from the starting point) in order to evaluate the changes within the tissue or constructs (e.g., glycosaminoglycan and collagen accumulation, water volume fraction change, gene expression). Current methods to investigate these property changes are usually invasive and require the destruction of the construct. Therefore, engineered constructs and tissue samples need to be destroyed or extra samples need to be prepared. Having extra samples means more time and money need to be invested. Furthermore, taking samples in and out of bioreactors also increases the chance of contamination. Therefore, in Chapter 5 a novel quantitative technique is proposed to characterize tissue properties noninvasively and in real time. With the development of this technique, one can create a new generation of

bioreactors where the engineered constructs can be long-term cultured and the properties of constructs can be determined noninvasively and in real-time.

The primary function of cartilaginous tissue is to support loads. Thus, it is important to understand the mechanical properties of cartilaginous tissue. In Chapter 6, a mechanical loading device is developed to determine the mechanical properties (i.e., tensile and compressive modulus) of tissue or constructs.

The development of the proposed measurement methods will provide information to further the understanding of the mechanisms of IVD degeneration. These methods will also provide new tools for investigating the tissue's response to its environment.

CHAPTER 2. BACKGROUND

2.1 STRUCTURE AND COMPOSITION OF IVD TISSUES

To understand the cause of disc degeneration, we need to first understand the structure and composition of IVDs. IVDs are located in between the vertebral bodies, linking them together. Around one-third of the spinal column is occupied by IVDs. They play an important role in mechanical support, as they constantly transmit loads arising from body weight and muscle activity through the spinal column (Urban and Roberts, 2003). They also provide spinal column flexibility, so they allow the spinal column to have the ability to perform bending, flexion and torsion.

IVDs are comprised of three major components: annulus fibrosus (AF), nucleus pulposus (NP), and cartilaginous end-plate (CEP) (Figure 2-1). The composition of the IVD varies with age and also with the location in the spinal column (Urban and Maroudas, 1980). In a normal and healthy disc, NP is usually oval shaped and composed of randomly oriented collagen fibrils embedded in a highly hydrated proteoglycan gel. From a superior view of a transversely sliced disc, one can see that NP occupies around 50 to 60 percent of the cross-sectional area of the disc and is surrounded on its periphery by the AF and superiorly and inferiorly by CEPs (Lundon and Bolton, 2001; Guiot and Fessler, 2000). The primary function of NP is to redistribute applied loads.

AF is formed by a series of concentric lamellae which consist of collagen fibers running in the same direction within each lamella but opposite to those in adjacent lamellae, at approximately ±30° to the horizontal axis (Hickey and Hukins, 1980; Marchand and Ahmed, 1990). There is a loose connection between these lamellae layers. This relatively loose interconnection is thought to allow IVD deformation during flexion

and extension (Bibby et al., 2001). The AF lamellae enclose and contain the NP laterally. When loads are applied to disc, the pressure varies with posture and activity and transmits vertical stresses evenly to the outer AF and to the vertebrae (Urban and Roberts, 1995).

CEP is a thin layer of cartilage surrounding the cranial and caudal surfaces of the central regions of the disc. CEP is composed of two types of cartilage: hyaline and fibro cartilage (Lundon and Bolton, 2001). CEPs form thin and incomplete boundaries between IVDs and vertebral bodies. The primary functions of CEP are to prevent disc extrusion into the vertebral body as well as to evenly distribute the load to the vertebral body (Ferguson and Steffen, 2003). Moreover, CEPs are important routes for nutrients entering the disc. Since there are no blood vessels in the discs, nutrients can only enter discs by diffusion and convection of interstitial fluid flow. For the outer AF, water and small solutes can diffuse through the blood vessels surrounding the periphery of the annulus. However, the CEP route is the main route for water and solutes between discs and vertebral bodies for NP (Urban et al., 1978; Nachemson et al., 1970; Urban et al., 1977; Ogata and Whiteside, 1981).

IVDs are mostly comprised of water (65-90 percent wet weight) with significant quantities of collagen (15-65 percent dry weight), proteoglycan (10-60 percent dry weight) and other matrix proteins (15-45 percent dry weight) (Kraemer et al., 1985; Johnstone et al., 1992; Hendry, 1958; Gu et al., 1999b; Eyre et al., 1989; Panagiotacopulos et al., 1987; Pearce, 1993). Due to the low cell density of IVDs, most of the water exists in extracellular fluid (Urban and Maroudas, 1980). The water content also depends on age and varies by region. The composition of IVDs is summarized in Table 2-1.

Vertebral body →

Cartilaginous end plate (CEP)

Intervertebral disc (IVD) →

Nucleus pulposus (NP)

Anulus fibrosus (AF)

Vertebral body →

Sagital section

Anulus fibrosus

Lamellae

Nucleus pulposus
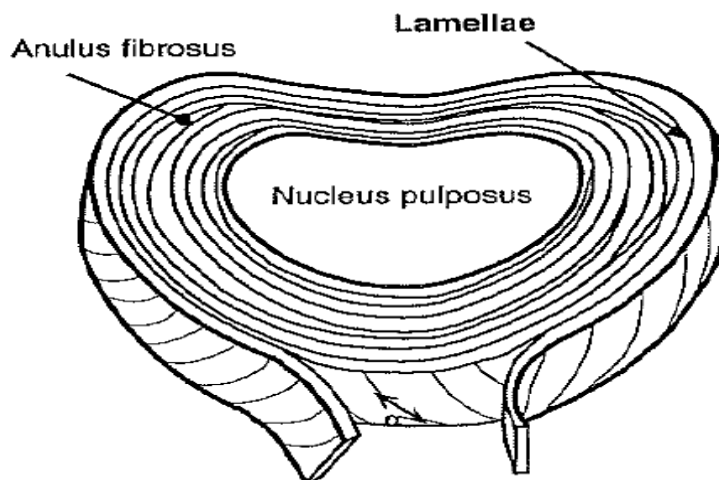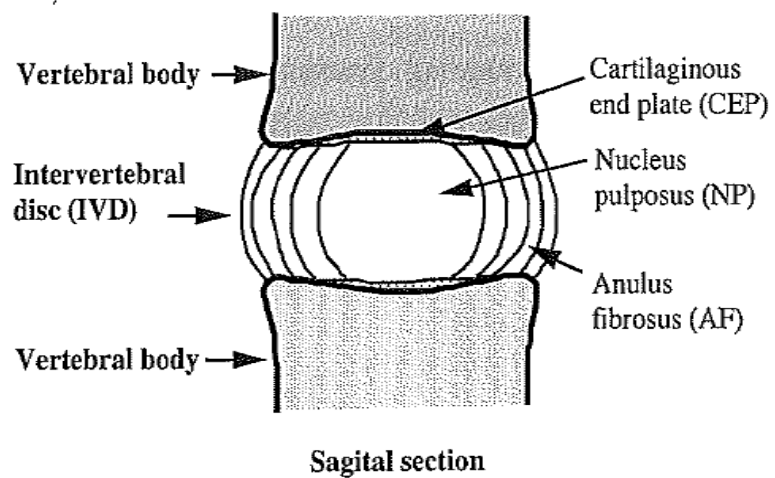
Figure 2-1: Anatomy of the intervertebral disc.

Table 2-1: Composition of the human AF and NP (Gu et al., 1997b; Hendry, 1958; Kraemer et al., 1985; Pearce, 1993; Panagiotacopulos et al., 1987; Johnstone et al., 1992; Heinegard et al., 1981). Other matrix proteins (not shown) are found in the IVD in relatively small amounts. PG content and hydration are known to decrease in degenerated discs, particularly in the NP (Lyons et al., 1981; Mitchell et al., 1961).

Composition	Annulus Fibrosus	Nucleus Pulposus
Water (% wet wt.)	60-70%	70-90%
Proteoglycan (% dry wt.)	10-20%	~50%
Collagen (% dry wt.)	50-70%	15-25%
Cell density	9000 cells/mm^3	4000 cells/mm^3

Collagen, which provides mechanical strength, is the most abundant fibrous protein in the connective tissues. In most tissues, it is also one of the major components of the extracellular matrix (ECM). There are many different types of collagen, and the composition varies within different tissues. In the IVD, type I and type II are the principal collagens. The outer AF is predominantly type I collagen, while the inner AF is primarily type II. Type II is only found in healthy NP. The collagen composition of the CEP is almost exclusively type II, with similar concentration and organization to that of articular cartilage (Roberts et al., 1989; Setton et al., 1993).

Proteoglycans (PGs) constitute glycoproteins covalently linked to one or more glycosaminoglycan (GAG) side chains, which are long, linear polymers of specific repeating carboxyl or sulfated disaccharides. Moreover, multiple PGs can link together, called aggrecan, with hyaluronan to form very large aggregates in cartilage (Figure 2-2). PGs of the intervertebral disc are made of a core protein covalently attached to side chains of chondroitin sulfate (CS) and of keratin sulfate (KS). The disaccharides comprising CS are glucuronic acid and N-acetyl-D-galactosamine, while the disaccharides comprising KS are galactose and N-acetyl-D-glucosamine (Figure 2-3). The carboxyl group on the glucuronic acid and sulfate group on the N-acetyl-D-galactosamine make CS carry two negative charges, while the sulfate group on the N-acetyl-D-glucosamine makes KS carry one negative charge. Therefore, each GAG chain bears many negative charges.
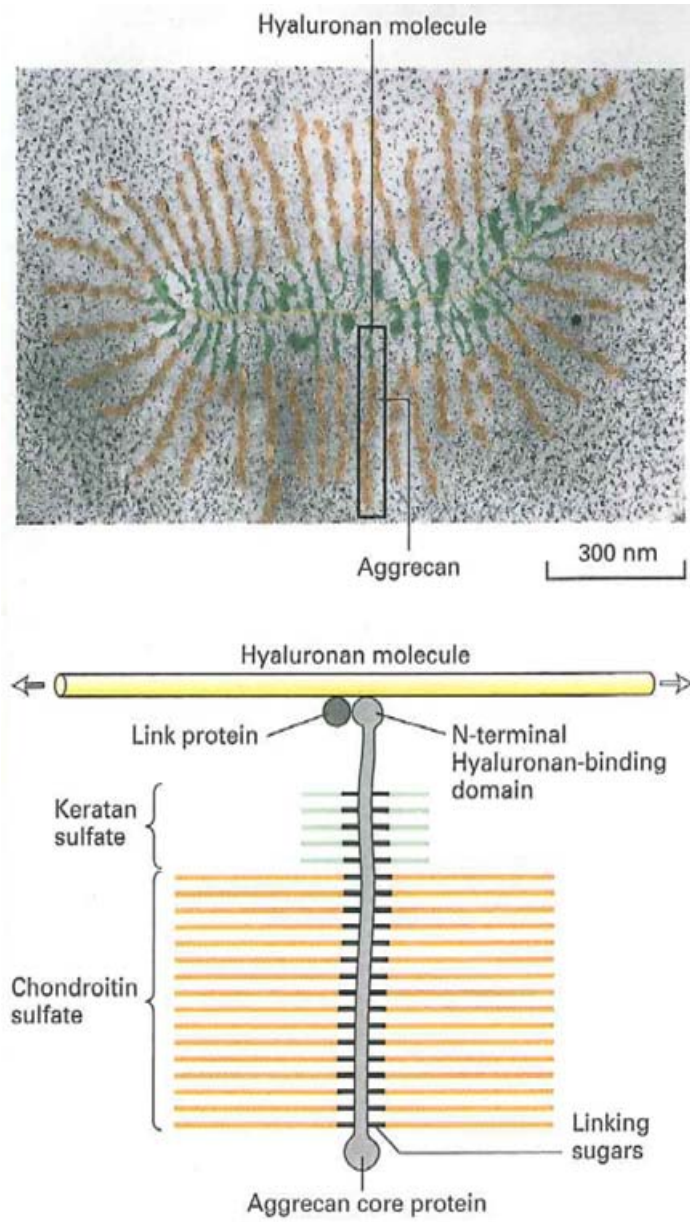
Figure 2-2: Structure of proteoglycan aggregate from cartilage (Harvey Lodish et al., 2003).
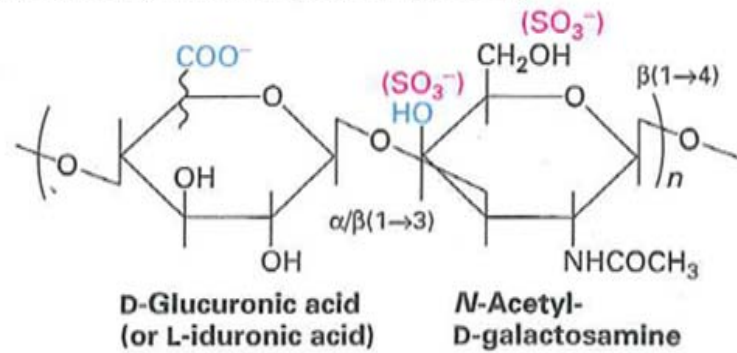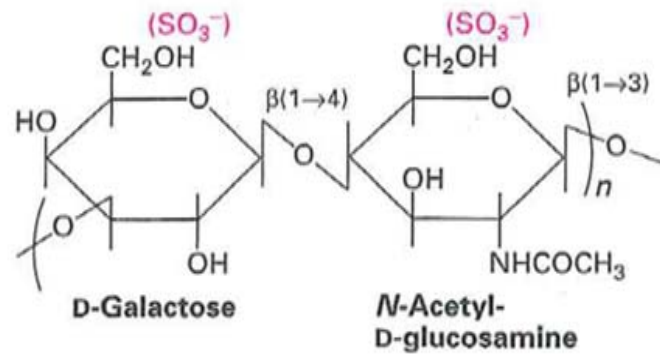
Figure 2-3: Structure of two major cartilaginous tissue GAGs: chondroitin sulfate and keratin sulfate (Harvey Lodish et al., 2003).

In addition, the IVDs' negatively charged material property is due to the carboxyl and sulfate groups of the glycosaminoglycans (Antoniou et al., 1996; Cole et al., 1986; Eyre et al., 1989; Guiot and Fessler, 2000; Jahnke and McDevitt, 1988; Lundon and Bolton, 2001; Lyons et al., 1981; Pearce, 1993; Roberts et al., 1994; Urban and Maroudas, 1980). The glycosaminoglycans are considered "fixed" in the extracellular matrix because aggrecans are entangled and restrained within the collagen network. Hence, electrostatic interactions between immobile, fixed charges (on the solid matrix) and mobile, free ions (in the interstitial fluid) give rise to physicochemical and electrokinetic effects, such as Donnan osmotic pressure and swelling, streaming potential and current, negative osmosis, and electro-osmosis effects (Eisenberg and Grodzinsky, 1985; Eisenberg and Grodzinsky, 1987; Frank and Grodzinsky, 1987a; Frank et al., 1987; Gu et al., 1998; Gu et al., 1997a; Gu et al., 1999b; Lai et al., 1991; Urban and Maroudas, 1981; Urban and McMullin, 1985; Urban and McMullin, 1988). Therefore, such a distinct structure renders IVDs capable of transmitting large loads between vertebrates.

2.2 CELLS FROM DIFFERENT REGIONS OF IVD

There are three visibly distinct cellular regions in discs: NP, AF and transition zone (TZ) (Figure 2-4). In vivo, NP cells (Figure 2-5) are spherical, surrounded by capsules and significantly larger than cells in AF and TZ (Maldonado and Oegema, Jr., 1992; Guilak et al., 1999). There are at least two different cell populations identified in the early lifetime of NP. One is a small round cell similar to chondrocytes, and the other is a much bigger cell, notochord, which has a vacuolated appearance. The notochord cells in the NP disappear with age and are replaced by fibrochondrocyte-like cells (Oegema, Jr., 1993). The disappearance of notochord cells as a result of low nutrient supplies may

signal the beginning of the degeneration process (Aguiar et al., 1999). Additionally, the decreased capacity of NP cells for repair and/or an inclination to more readily lose matrix components make the nucleus more vulnerable to degeneration than the annulus (Cs-Szabo et al., 2002). The primary function of NP is to maintain the extensive extracellular matrix of IVD.

Cells from AF (Figure 2-6) are derived from mesenchyme tissue. The cell population in outer AF is mainly fibroblastic, and they are elongated in appearance and position themselves parallel to the predominant collagen fibril orientation (O'Halloran and Pandit, 2007). The cells in the inner AF and TZ display characteristics of both fibroblast and chondrocyte-like cells (Walker and Anderson, 2004).

The cell population of IVDs is lower when compared to that of cartilage, and cells are distributed inhomogeneously in IVD. Cells are scattered in the NP and have a cell density between 3300 to 4700 cells/mm^3. On the contrary, cells are abundant in the AF and have a density between 7000 to 12000 cells/mm^3 (Maroudas et al., 1975; Horner et al., 2002). However, cells form only 1 percent of the disc by volume. Despite the low volume percentage of IVD cells, they are critical to maintaining healthy tissue, since they produce both extracellular matrix components and the compounds responsible for matrix breakdown and are decisive for tissue composition and turnover (Bibby et al., 2001).
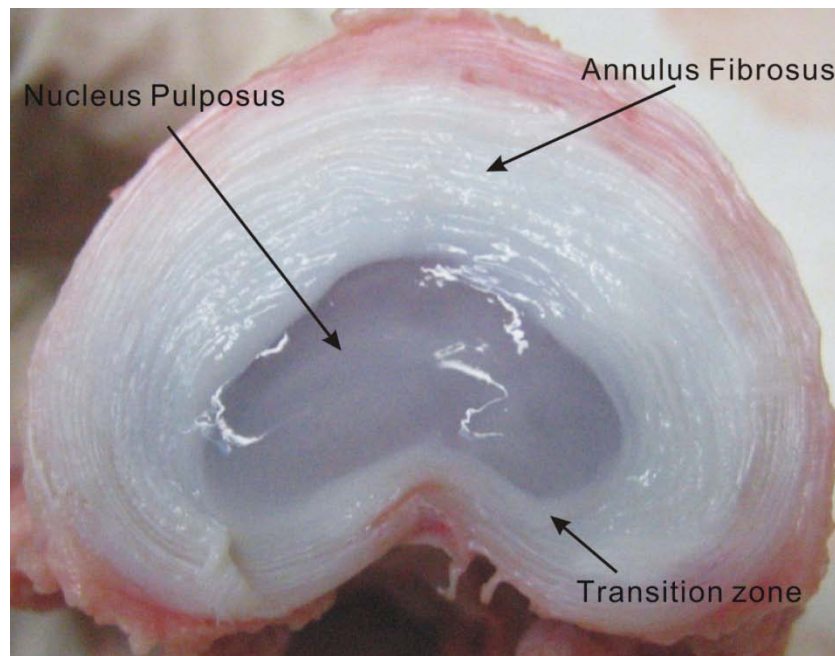
Figure 2-4: Porcine lumbar disc. Three distinct regions, NP, AF and TZ, can be seen clearly from picture.
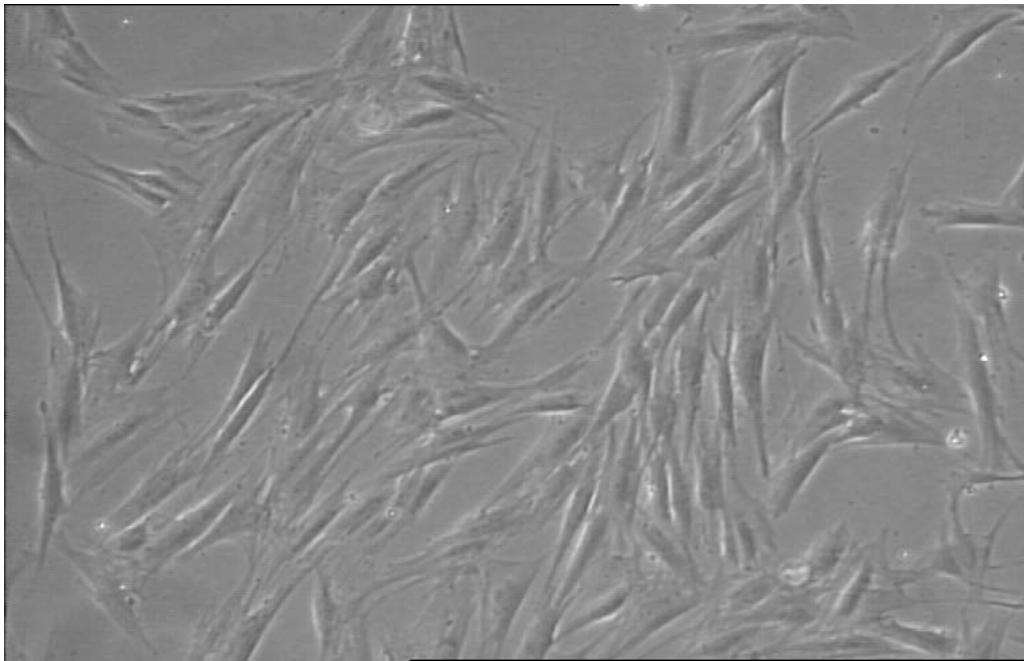
Figure 2-5: NP cells from 6 months old porcine lumbar.
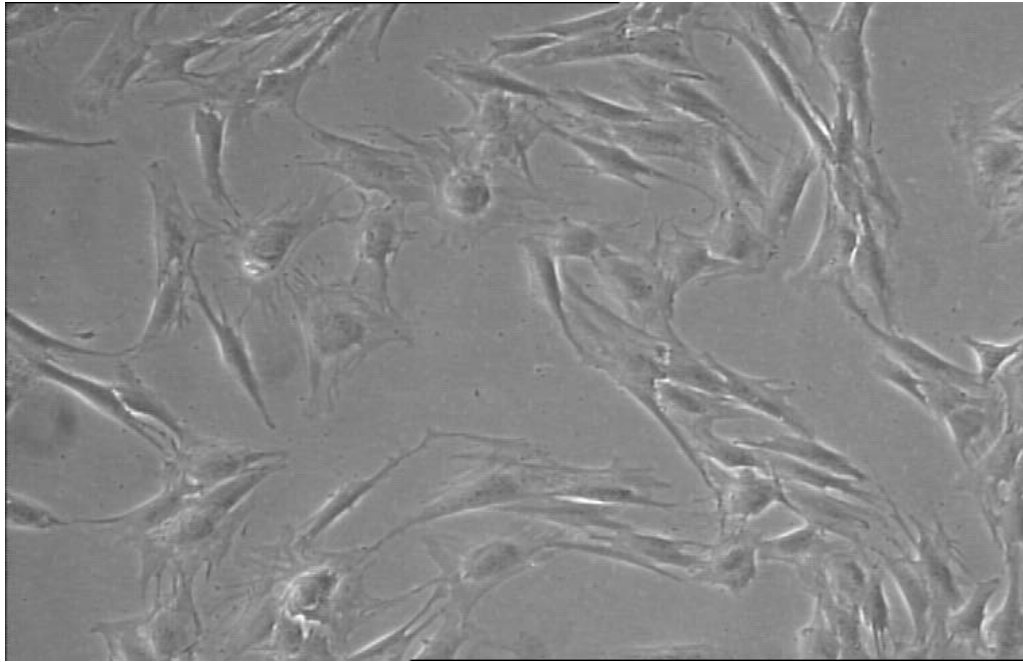
Figure 2-6: AF cells from 6 months old porcine lumbar.

2.3 IVD DEGENERATION

As previously mentioned, low back pain is strongly associated with IVD degeneration. It is believed that disc degeneration usually begins as early as the second decade of life and increases in severity with age (Nerlich et al., 1997). Disc degeneration occurs far earlier in IVDs than in other musculoskeletal tissues (Boos et al., 1993; Miller et al., 1988). About 20% of people in their teens have developed signs of mild disc degeneration. Degeneration is also related to age: 97% of lumbar discs show evidence of degeneration by age 50 or older, and 10% of these discs are severely degenerated. By age 60, approximately 60% of lumbar discs are severely degenerated (Miller et al., 1988). With disc degeneration, changes in disc morphology, biochemistry, function, and material properties occur.

NP and inner AF are avascular throughout life, but blood vessels from adjacent vertebral bodies penetrate into CEP and outer AF. Although the volume of IVDs grow rapidly from the age of three to four, the total number of blood vessels that supply IVDs decreases considerably (Urban and Roberts, 1995). The thickness of CEP also decreases with age and injury. The CEP also becomes calcified. This leads to a decrease in tissue permeability to water and solute. The decline in the number of vessels, as well as permeability decreasing, hinders the nutrient supplies to NP. As a result, the number of notochord cells in the NP decreases and are replaced by fibrochondrocyte-like cells. Furthermore, the number of necrotic and apoptotic cells increases with age: from only two percent of necrotic cells in the fetal population to more than fifty percent in the adult cell population (Gruber and Hanley, Jr., 1998).

With age, NP gradually loses its translucency and becomes firm, white and less hydrated. NP becomes more collagenous, and the transition zone between NP and inner AF becomes indistinct as well. Cleft formation occurs in NP and AF. The thickness of AF lamellae increases and becomes progressively more fibrillated. Clefts in the AF disrupt lamellae and make it less organized. This impairs AF load-bearing function and leads to IVD rupture. Furthermore, IVDs become discolored with an accumulation of brown and yellow age pigments (Urban and Roberts, 1995).

Two major macromolecular components are responsible for IVD mechanical function: collagen and proteoglycans. In healthy discs, the hydrophilic property of PG helps discs retain water and withstand compressive load, while collagen provides IVD the tensile stiffness. However, the concentrations of PG and collagen decrease in aged and degenerated discs. The most significant biochemical change seen in the degenerated disc is the loss of proteoglycans (Lyons et al., 1981).

The concentration of PGs in the NP decreases with age as well as the rate of synthesis of PGs. The concentration of PGs can change tissue permeability and diffusion rates. Furthermore, these two parameters can affect the exchange of nutrients and waste in and out of tissue (Cassinelli et al., 2001). Moreover, the proportion of nonaggregated PGs progressively increases and the size of PGs dramatically decreases because of a decline in link proteins (Buckwalter, 1995). The smaller size of PGs makes it easier for them to leach out of IVDs. The loss of PGs is believed to be responsible for the decrease in osmotic pressure and tissue hydration (Urban and McMullin, 1988), resulting in the loss of load-support capability of the disc (Adams et al., 1996). The decrease in tissue hydration also affects the movement of molecules into and out of the disc (Maroudas et

al., 1975). The changes in collagen with disc degeneration are not as obvious as those in the PGs (Urban and Roberts, 2003).

Enzyme activity is also an indicator for biochemical change of IVD degeneration (Urban and Roberts, 2003). Cells of IVDs not only produce molecules to synthesize ECM, but also produce enzymes (such as MMPs and aggrecanases) to break down ECM (Urban and Roberts, 2003). The balance between synthesis and break-down is well maintained in the healthy discs, but it is disrupted in degenerated IVD. In the degenerated IVD, MMPs and aggrecanases show higher levels of activity than in healthy discs.

2.4 TISSUE ENGINEERING IN IVD

Low back pain is not a life threatening disease. Nonetheless, psychological distress and physical disability could cause patients to spend large amounts of money in an attempt to relieve the pain. Current treatments focus on pain control while overlooking the root of the problem. Currently, there are many pain-relieving therapies commonly used, such as: pain-relieving pharmaceuticals, transcutaneous electrical nerve stimulation, physical manipulation, exercise therapy and behavior therapy (Bogduk, 2004; Kalson et al., 2008). The effects of these therapies remain in question, despite the large number of clinical trials and studies performed (van der et al., 2005). When patients do not respond to the previously mentioned therapies, surgery becomes a viable option. A common surgical procedure is the removal of the degenerated disc, or discectomy. However, a discectomy may alter the biomechanics of the contiguous spine motion segments and may cause stress to adjacent discs (Kalson et al., 2008; Errico, 2005; Hilibrand and Robbins, 2004).

As a result, there is a need to develop new treatments capable of removing the degenerated disc and replacing it with a healthy one. Using tissue engineering techniques to create biological substitutes has the potential to provide a means for replacing degenerated discs. In order to create a cartilaginous tissue, the engineered construct has to be cultured in a sterile environment capable of mimicking in vivo conditions native to IVDs. The role of bioreactor systems is to mimic the in vivo conditions of a tissue (Concaro et al., 2009).

Currently, there have been many different types of bioreactors developed for cartilaginous tissues: spinner flask, rotating-wall vessel, direct perfusion bioreactor, hydrodynamic focusing bioreactor, hollow-fiber bioreactor, and compression bioreactors.

The spinner flask is a bioreactor designed to overcome diffusion limitations and enhance mass transfer into the engineered constructs. Inside the spinner flask, the medium is mixed mechanically by a magnetic stirring bar, and some of the flasks even have holes for gas exchange (Tognana et al., 2005; Vunjak-Novakovic and Freed, 1998; Freyria et al., 2004; Vunjak-Novakovic et al., 1996; Vunjak-Novakovic et al., 1998).

Rotating-wall vessel is another commonly used bioreactor. The entire bioreactor is rotated in order to balance the external forces on the constructs and improve mass transfer while maintaining low shear stress profiles, unlike the previously mentioned spinner flask (Vunjak-Novakovic and Freed, 1998; Pei et al., 2002; Vunjak-Novakovic et al., 1998; Vunjak-Novakovic et al., 1999; Martin et al., 2000; Martin et al., 1999; Freed and Vunjak-Novakovic, 1995).

Direct perfusion bioreactor has the ability to force the medium into the bioreactor continuously. The engineered construct is confined inside the perfusion chamber, and the

culture medium is forced through the construct instead of going around it. Consequently, mass transfer is dramatically increased by enabling the uptake of nutrients by convection, instead of depending on the slower diffusion process. In addition to enabling convection, medium flow also exerts mechanical stimulus by applying shear stress on the cells. Since shear stress is a function of flow rate, mechanical stimuli can be controlled by adjusting the flow rate (Freyria et al., 2005; Bancroft et al., 2002; Minuth et al., 2001; Strehl et al., 2005; Pazzano et al., 2000; Tsao and Gonda, 1999; Mizuno et al., 2001).

Hydrodynamic focusing bioreactors are capable of localizing fluid flow and allowing for adjustable shear (Tsao and Gonda, 1999). Hollow-fiber bioreactors, in which semi-permeable tubes are used, have the potential to increase the transportation of nutrients and oxygen (Concaro et al., 2009).

Last but not least, compression bioreactors can apply mechanical loading to the constructs. Such compression loading can be static or dynamic, and some can even allow for multiple forces, such as compression and shear (Frank et al., 2000). Overall, a successful bioreactor for cartilaginous tissue engineering should take advantage of the mechanical stimuli in conjunction with good mass transport properties to create an environment suitable for long-term tissue growth.

CHAPTER 3. STRAIN-DEPENDENT OXYGEN DIFFUSIVITY IN ANNULUS FIBROSUS TISSUE

3.1 BACKGROUND

Because IVDs are avascular tissues, capillaries and nerves only penetrate into the outermost regions of the disc. Therefore, the supply of nutrients and removal of metabolic wastes at the margin of IVD is dependent on blood vessels of surrounding IVDs. However, for the NP and most of the AF cells, nutrients are supplied by the capillary network of the adjacent vertebral bodies. Nutrients are transferred from the capillaries of the vertebral bodies through the end-plate of the IVD into the cells.

IVDs are the largest avascular structures in the human body. In adult lumbar discs, cells can be as far as 8 mm away from the closest blood supply (Bibby et al., 2001). Due to its avascular nature, nutrition supply into IVDs is mainly through the diffusion of small solutes such as oxygen and glucose from the peripheral blood vessels (Urban et al., 1978; Maroudas, 1975; Urban et al., 1982). Transport property is an important index for IVD tissue health. By determining the transport properties, we can learn whether or not cells have enough nutrient supply to survive. Transport property is also an important key for tissue engineering applications. When tissues or engineered constructs are growing in the bioreactors, the transport property of tissues or cell matrix constructs are changing as well. This will not only alter the rate of fluid and solutes transport within tissues or constructs, but also affect their growth and health.

One of the primary causes of disc degeneration is thought to be failure of nutrient supply to the disc cells (Nachemson et al., 1970). Poor nutrition is believed to be an important factor leading to the onset of disc degeneration (Nachemson et al., 1970; Holm and

Nachemson, 1982; Horner and Urban, 2001; Bibby et al., 2002; Urban, 2001). Adams and Hutton (1986) used radioactive tracers to study mechanical loading effects on diffusion of small negatively and positively charged solutes. Holm and Nachemson (1982) used canine model to study fused and unfused spine discs metabolites profiles. Bibby et al. (2002) investigated the cell viability of the human scoliotic disc in relation to concentrations of metabolites and extracellular matrix components.

While previous studies have aimed at analyzing the effects of mechanical loading on water content, chemical composition, and nutritional levels in the IVD (Holm and Nachemson, 1982; Bibby et al., 2002; Adams and Hutton, 1986), to our knowledge, no study has investigated the effect of mechanical compression on oxygen diffusivity in the IVD tissue. Cells consume glucose and oxygen to produce adenosine triphosphate (ATP) which is the major energy form in the cell. IVD cells, like all cell types, require nutrients such as oxygen and glucose to remain alive and active (Urban and Roberts, 2003).

Therefore, the objective of this study was to investigate the effects of mechanical loading on oxygen transport in IVD tissue by determining oxygen diffusivity in human annulus fibrosus (AF) under 3 levels of compressive strain (5%, 15%, and 25%). It was also hypothesized that the diffusion of oxygen in AF is anisotropic (i.e., direction-dependent) as a result of the layered structure of AF tissue. Subsequently, the oxygen diffusivity in human AF tissue in three principal directions (i.e., axial, radial and circumferential) was also investigated.

3.2 THEORETICAL BACKGROUND

The diffusion coefficient can be determined by a one-dimensional steady-state diffusion experiment (Figure 3-1). It is noted that similar methods have been employed to determine solute diffusivities in cartilage (Maroudas et al., 1968; Malda et al., 2004) and in bovine IVD (Jackson et al., 2008). The diffusive flux (J) within the tissue is governed by Fick's law, and during a steady state, J (defined as the mass flow rate of solute ΔQ, per unit area, A) can be obtained by calculating the difference in concentration of solute between the upstream and downstream chambers:

$$J = \frac{\Delta Q}{A} = D \frac{K\left(C_{up} - C_{down}\right)}{h} \, , \tag{3-1}$$

where D is the diffusivity, C_{up} is the oxygen concentration in the upstream compartment, C_{down} is the concentration of oxygen in the downstream compartment, A is the diffusion area, and h is the thickness of the sample after compression. K is the partition coefficient; in this study, it was assumed to be unity ($K = 1$) since oxygen is a small molecule. The flux is also related to the concentration in the downstream chamber by conservation of mass:

$$J = \frac{V_{down} dC_{down}}{A dt} \, , \tag{3-2}$$

where V_{down} is the volume of solution in the downstream compartment, and t=time.

Therefore, From Fick's Law and conservation of mass, we can derive the following differential equation:

$$\frac{V_{down}\, dC_{down}}{A\, dt} = D\frac{(C_{up} - C_{down})}{h} \quad ,$$

(3-3)

In arriving to equation (3-3), a linear distribution of concentration within the specimen has been assumed. The oxygen diffusivity may be calculated by (Malda et al., 2004; Jackson et al., 2008):

$$D = ln\left[\frac{C_{up} - C_{down}(t_o)}{C_{up} - C_{down}(t)}\right]\frac{V_{down}\, h}{A(t - t_o)}$$

(3-4)

where $C_{down}(t_o)$ and $C_{down}(t)$ are the concentrations of oxygen in the downstream chamber at time t_o (initial time) and t, respectively.
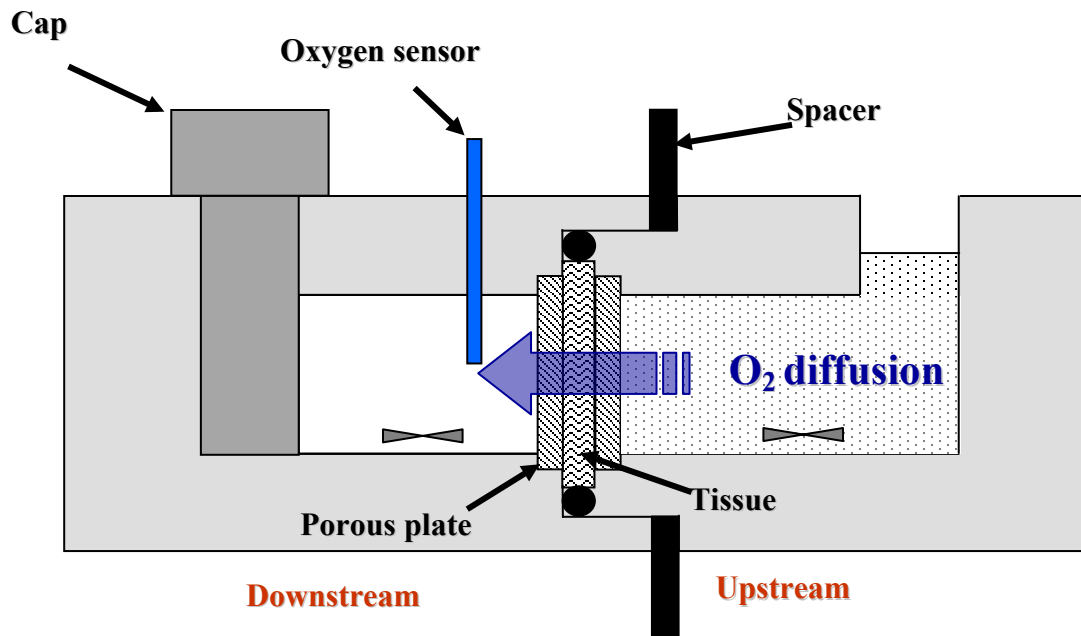
Figure 3-1: Schematic of the custom-designed diffusion apparatus. Oxygen diffusion occurs from upstream chamber (right), across the tissue specimen, and into the downstream chamber (left), where the oxygen concentration is measured using an oxygen sensor.

3.3 MATERIALS AND METHODS

Oxygen diffusion chamber. In order to accurately measure the strain-dependent diffusivity of oxygen in IVD tissue, an acrylic diffusion chamber was custom-designed and built (Figure 3-2). The diffusion chamber consisted of two compartments divided by a specimen holder located in the middle. Internal volumes of upstream and downstream compartments were 0.24 ml and 0.2 ml, respectively. Prior to the start of the experiment, deoxygenated phosphate buffered solution (PBS) (P4417, Sigma-Aldrich Corp., St. Louis, MO) was prepared by introducing nitrogen gas into 2 ml PBS solution for one hour (Bibby et al., 2005).

The specimen was compressed between two porous plates (hydrophilic porous polyeth sheet, SmallParts, Settle, WA) with 50-90 μm pore size and 50% porosity, and sealed with an o-ring. The amount of compression was controlled by the thickness of the spacer (shim washer, MSC, Melville, NY) (0.5 mm, 0.45 mm and 0.4 mm). The AF specimen was first confined to 5% nominal compressive strain, and the downstream compartment was filled with the deoxygenated PBS solution while the upstream compartment was filled with air-saturated PBS. To maintain a constant oxygen concentration upstream, the PBS solution in it was replaced periodically (about every 2 minutes) with fresh solution. Real-time oxygen concentration downstream was recorded using NeoFox Optic oxygen sensor system (Ocean Optics Inc., Dunedin, FL).

Oxygen measurement system. NeoFox Optic Oxygen Sensor System (Ocean Optics Inc., Dunedin, FL), which consists of a fiber optic fluorescence probe, was used to measure oxygen concentration. The FOXY fiber oxygen sensor uses the fluorescence of a ruthenium complex in a sol-gel to measure the partial pressure of oxygen. The quenching

behavior of the probe is described by the Stern-Volmer equation, where the fluorescence

is related quantitatively to the partial pressure of oxygen:

$$\frac{I_0}{I} = 1 + k \times [O_2],$$ (3-5)

where I_0 is the intensity of fluorescence at zero pressure of oxygen, I is the intensity of

fluorescence at a pressure p of oxygen, and k is the Stern-Volmer constant (Ocean Optics

& OOISensors Fiber Optic Sensors System Installation and Operation Manual, 2006).

Prior to conducting the oxygen diffusion experiment, a two-point method (with

deoxygenated PBS solution represented the 0% oxygen concentration and air represented

the 21% oxygen concentration) was used to calibrate the oxygen sensor system to verify

that the system was functioning properly.

Oxygen chamber validation. Bovine AF tissue was used to validate the oxygen

diffusion chamber. Previous studies have shown that the composition, mechanical

properties, and synthesis rates of bovine coccygeal discs are similar to those for human

IVD (Ohshima et al., 1993; Beckstein et al., 2008). In order to meet our objective of

investigating the strain-dependent behavior of oxygen diffusivity using a tissue similar to

human IVD, bovine coccygeal IVD were used in this study as they are easily obtainable

at a low cost.

A total of three fresh bovine tails (~6 months old) were obtained from a local

supermarket. After carefully removing the excess tissue and ligaments surrounding the

discs, a total of five coccygeal IVD (S2-3 and S3-4) were harvested. A total of 20 axial

AF samples were prepared using a corneal trephine (Biomedical Research Instruments,

Inc., Silver Spring, MD) and sledge microtome (Model SM2400, Leica Instruments,

Nussloch, Germany) with freezing stage (Model BFS-30, Physitemp Instruments, Inc., Clifton, NJ) (Figure 3-3). The cylindrical samples were 6 mm in diameter and approximately 0.5 mm in thickness. Note that the thickness of each specimen was measured using a custom-designed current sensing micrometer (accuracy: ± 3 μm) (Figure 3-4) (Gu and Justiz, 2002), and used for calculating the level of compressive strain (i.e., engineering strain) in the testing chamber. Each of the 20 specimens was tested to measure oxygen diffusivity at 3 different levels of nominal compressive strain (5%, 15%, and 25%)

Human AF tissue. Two L2-L3 discs (ages 41 and 63, Thompson grades I and III, respectively) were harvested from two human lumbar spines obtained from the Tissue Bank at the University of Miami Miller School of Medicine. Cylindrical specimens having an approximate height of 0.5 mm and a diameter of 6 mm were prepared using a corneal trephine and microtome with freezing stage. Specimen height was measured using a custom-designed current sensing micrometer as mentioned previously (Fig. 3-4). From each disc, specimens were prepared in each of three principal directions: axial, circumferential and radial (see Fig. 3-5). Three tests, corresponding to three levels of compression, were performed on each specimen.

To ensure that concentration distribution within the tissue is linear, oxygen diffusivity was calculated from the measured data using the final 15 minutes of the experiment (i.e., $t_o = 45$ minutes and $t - t_o = 15$ minutes). The experiment was repeated for 15% and 25% (nominal) compressive strains on the same tissue specimen.
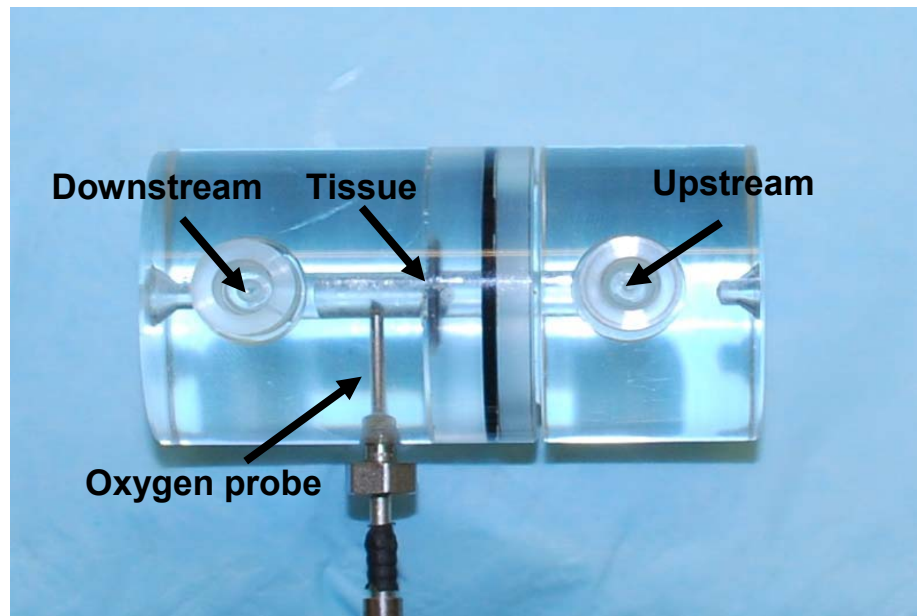
Figure 3-2: Photograph of the oxygen diffusion chamber

Figure 3-3: Photograph of the sledge microtome with freezing stage

Figure 3-4: Photograph of the current sensing micrometer
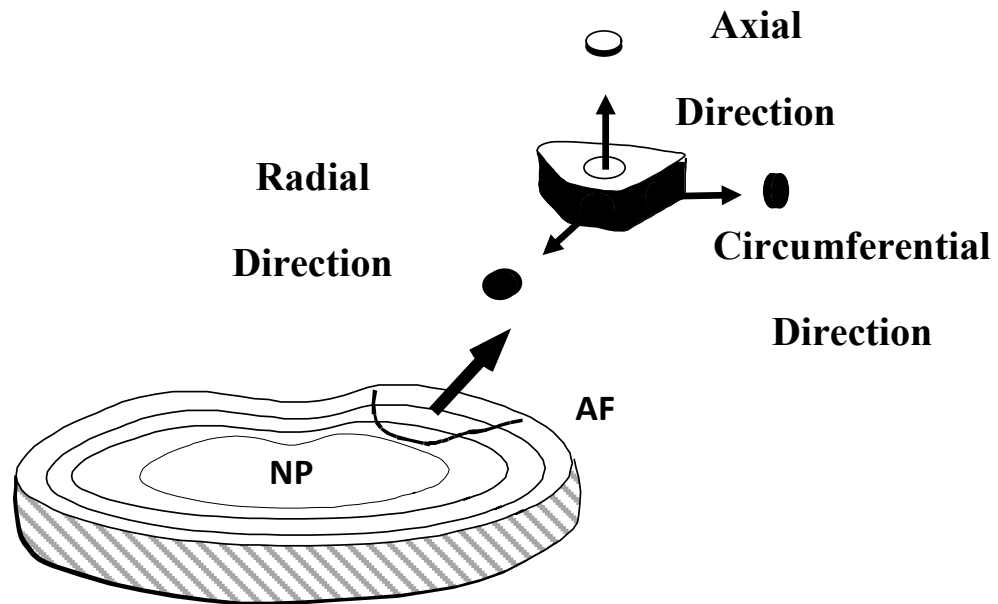
Figure 3-5: Schematic showing annulus fibrosus (AF) and nucleus pulposus (NP) regions of disc and three principal directions for specimen preparation.

3.4 RESULTS

Bovine AF. A sample of raw experimental data showing the change in the oxygen concentration in the downstream chamber with elapsed time is shown in Figure 3-6. The oxygen diffusivity was calculated using equation (3-4). The results, shown in Figure 3-6, indicate that the oxygen diffusivity in AF decreased with increasing compressive strain. The average oxygen diffusivity (mean ± SD) of bovine AF in the axial direction is shown in Figure 3-7 and data is listed in Table 3.1. Measurements were carried out at room temperature ($22.2^oC \pm 0.45^oC$). To estimate the value of diffusivity at zero-strain, a linear regression line was used to fit the experiment data. It was found that the oxygen diffusivity in bovine AF at 0% compression was 1.73×10^{-5} cm^2/s (Figure 3-8). The mean height of the specimens under zero compression condition was 0.525 ± 0.009 mm.

A one-way analysis of variance (ANOVA) test was used to analyze the data and showed that oxygen diffusivity was significantly affected by the level of compression ($P<0.05$). A Student-Newman-Keuls post-hoc test showed a significant difference between oxygen diffusivity in the compressive strain group ($P<0.05$).

Human AF. The results for the diffusivity of oxygen in human AF tissue are shown in Table 3-2. The strain was calculated based on the initial and confined heights of the specimen. A one-way ANOVA analysis for each direction showed that there was a significant decrease in diffusivity with increasing compressive strain for all directions investigated ($p<0.05$) (Figure 3-9). However, there was no significant difference in diffusion coefficients in the three different directions. The oxygen diffusivity values in human AF at 0% compression were found to be: 1.22, 1.33 and 1.23×10^{-5} cm^2/s in the axial, circumferential, and radial directions, respectively (Figure 3-10).

Table 3.1: Results for average strain and oxygen diffusivity of bovine AF in axial direction.

Strain (%)	Oxygen diffusivity ($\times 10^{-5}$ cm^2/s)
4.68 ± 1.67	1.43 ± 0.242
14.2 ± 1.50	1.05 ± 0.282
23.7 ± 1.34	0.77 ± 1.63
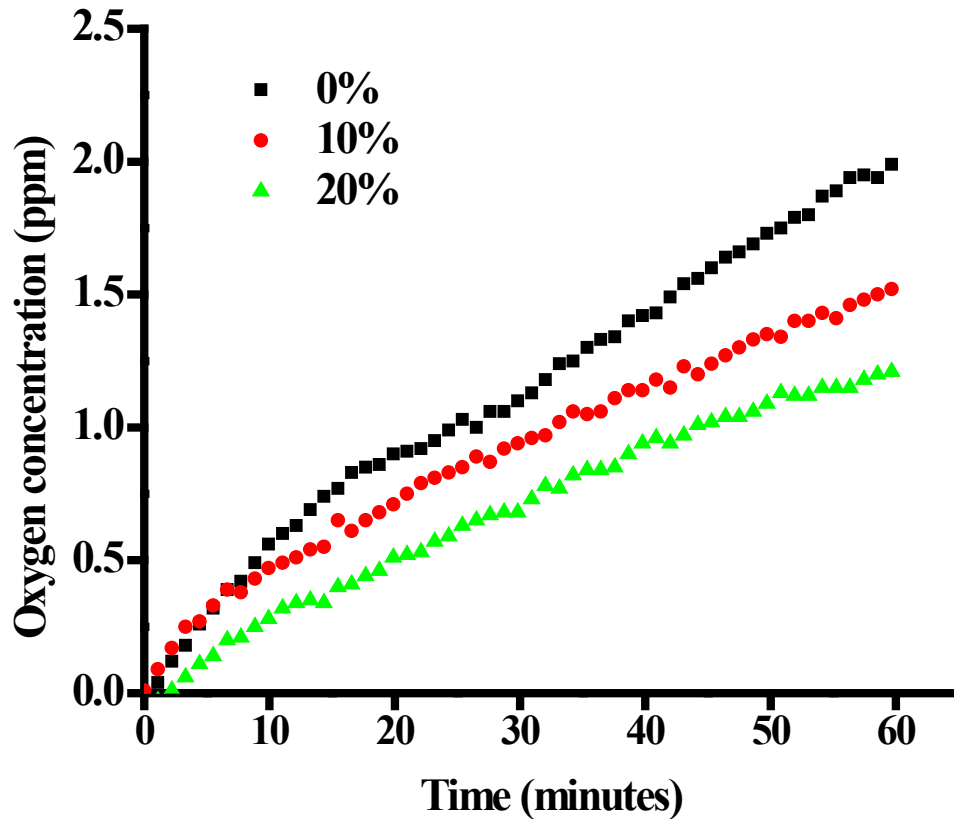
Figure 3-6: An example of raw experimental data showing the change in the oxygen concentration in the downstream chamber with elapsed time. For this particular specimen, the actual levels of compression were 1.4%, 11.2%, and 21.1%. The diffusivity was calculated using equation (3-4). Note the decrease in slope with increasing compressive strain, indicating the strain-dependent behavior of oxygen diffusivity.
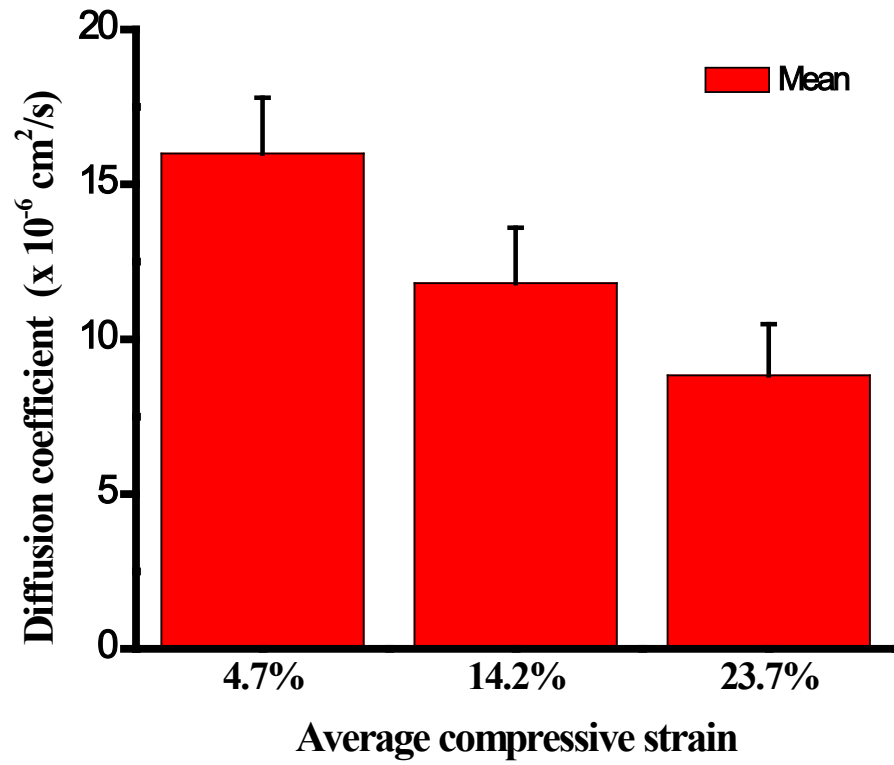
Figure 3-7: Strain-dependent oxygen diffusivity in bovine AF.
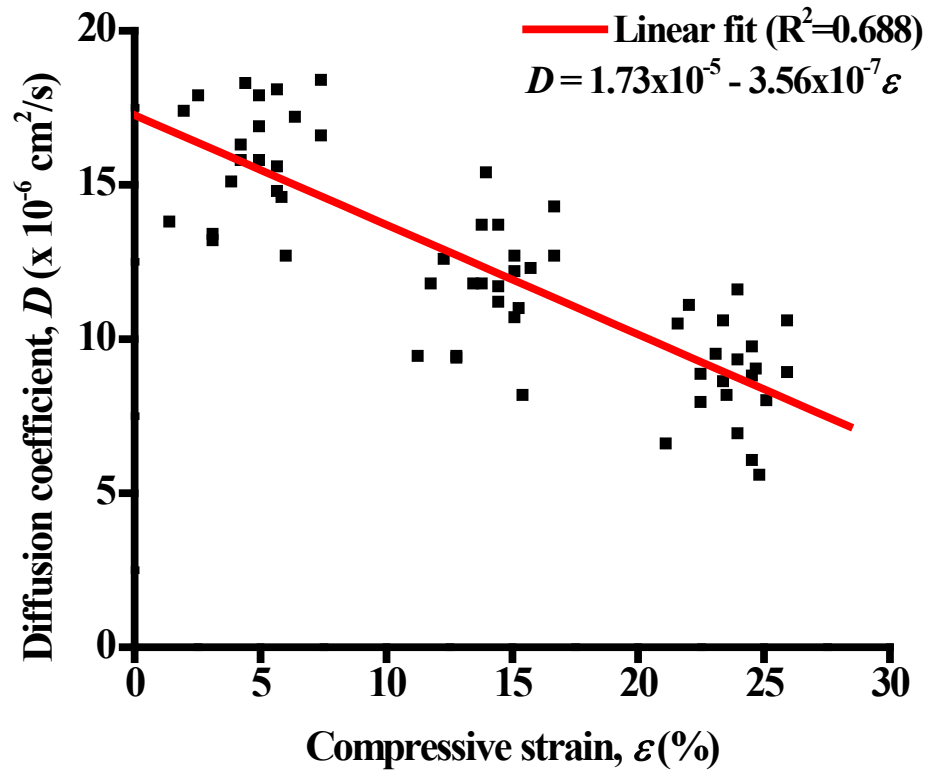
Figure 3-8: Variation in diffusivity of oxygen with applied strain at room temperature (22.2°C ± 0.45°C). A linear regression (R^2 = 0.562, n=60) was used to estimate the diffusivity at zero stain. In the linear regression, *D* is the diffusivity and ε is the applied compression (%). From this, the oxygen diffusivity in bovine AF at 0% compression (i.e., ε = 0) was determined to be 1.56 x 10^{-5} cm^2/s.

Table 3-2: Results for diffusivities of oxygen in human AF in three principle directions and at three levels of strain.

	n	Strain (%)	D (×10⁻⁵ cm²/s)
	8	0.86±0.88	1.21±0.33
Axial	8	10.3±0.8	0.84±0.40
	8	19.3±3.1	0.65±0.20
	4	0.24±0.49	1.41±0.37
Circum.	4	9.8±0.6	1.01±0.16
	4	19.3±0.8	0.80±0.22
	4	0.89±0.70	1.25±0.22
Radial	4	10.0±0.3	0.79±0.20
	4	19.1±0.2	0.60±0.13
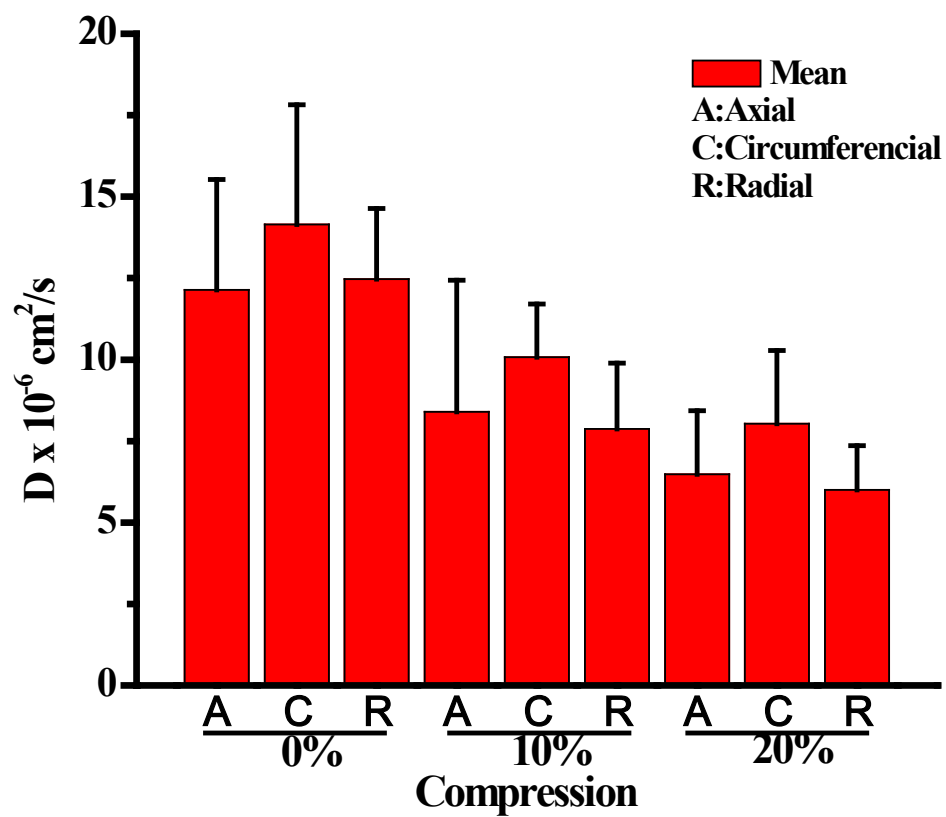
Figure 3-9: Strain-dependent oxygen diffusivity in human AF.
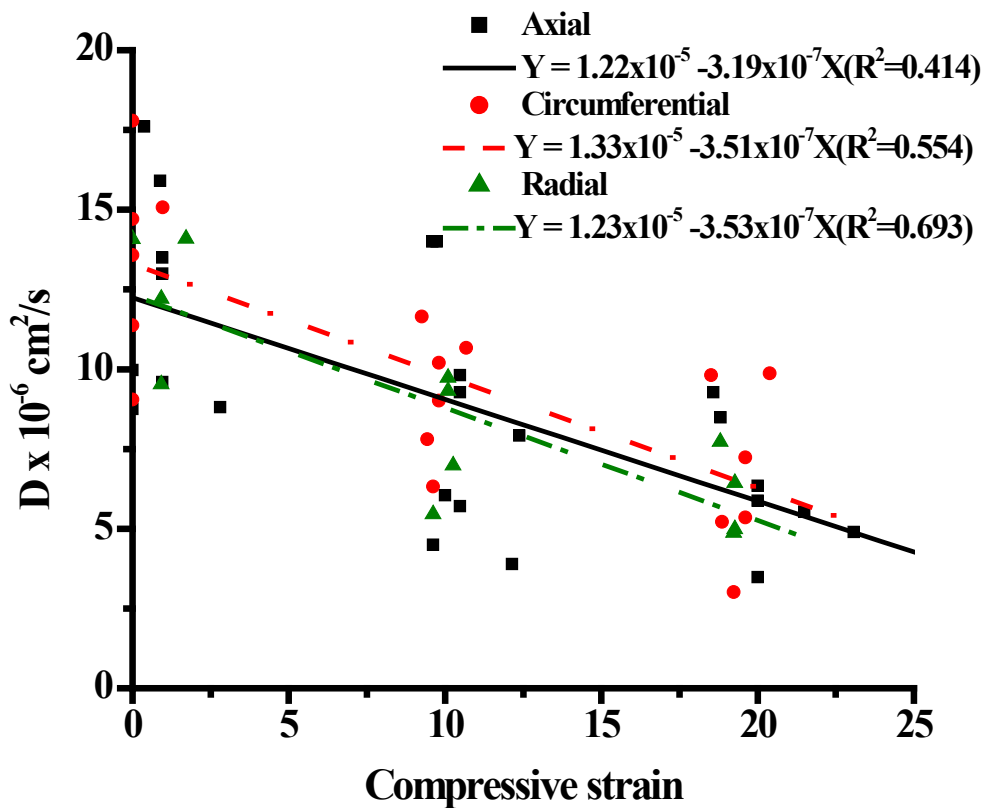
Figure 3-10: Oxygen diffusivity of human AF at 0% compression in all three directions. 1.22×10^{-5} cm^2/s in axial, 1.33×10^{-5} cm^2/s in circumferential and 1.23 in the radial direction.

3.5 DISCUSSION

There are few studies in the literature that have focused on oxygen diffusivity of IVD and cartilage tissues (Malda et al., 2004; Haselgrove et al., 1993; O'Hare et al., 1991; Macpherson et al., 1997). Previous studies have reported the strain-dependent diffusivity behavior of different solutes in articular cartilage and IVD tissues (Burstein et al., 1993; Quinn et al., 2000; Quinn et al., 2001; Ngwa et al., 2002; Chiu et al., 2001; Drew et al., 2004; Jackson et al., 2008), but no study has investigated the stain-dependent behavior of oxygen diffusivity in IVD.

Our previous study (Gu et al., 2004) showed that the diffusivity (D) of small and macro molecules in gel and cartilaginous tissue could be estimated by the following model:

$$\frac{D}{D_o} = exp\left[-\alpha\left(\frac{r_S}{\sqrt{\kappa}}\right)^\beta\right], \tag{3-6}$$

where r_s is the solute Stokes radius, κ is the tissue Darcy permeability, α and β are two positive parameters that depend on the structure of the tissue, and D_o is the solute diffusivity in water at the same temperature. While the values of both D and D_o are sensitive to temperature, the value of the relative diffusivity (D/D_o) should not be, assuming the structure and composition of the tissue do not change with temperature. One previous study showed that the relative oxygen diffusivity (D/D_o) for porcine AF was between 0.3 to 0.6 (O'Hare et al., 1991), and the other studies showed that the relative oxygen diffusivities for bovine and avian articular cartilage were ~0.71 ($\sim2.2\times10^{-5}$ cm²/s in tissue at 37°C) and ~0.66 ($\sim2.0\times10^{-5}$ cm²/s in tissue at 35°C),

respectively (Malda et al., 2004; Haselgrove et al., 1993). Using the value (2.2×10^{-5} cm^2/s) of oxygen diffusivity in water at 22°C (Himmelblau D.M., 1964), and experimental data from the current study in bovine tissue, it was found that the relative oxygen diffusivity for AF at zero compression was 0.71, which is in agreement with the result reported for bovine articular cartilage (Malda et al., 2004).

The results from current experiment showed that oxygen diffusivity decreased as the compressive strain increased. IVD tissue may be considered as a porous material with various sizes of pores, which are filled with water. The overall porosity of tissue can be measured by the value of water volume fraction. The average size of the pores in the tissue can be estimated by the square root of its Darcy permeability (Gu et al., 2004; Gu et al., 2003), which is at nanometer scale for cartilaginous tissues (Gu et al., 2003). For these tissues, the Darcy permeability (or average pore size) is related to the volume fraction of water (or water content) (Gu et al., 2003). When a tissue is compressed, fluid exudation leads to a reduction in tissue water content. For bovine coccygeal AF, our previous study showed that water content was 76% at zero compression, and was estimated to decrease to 75%, 72%, and 68% under 5%, 15%, and 25% compressive strains, respectively (Jackson et al., 2008). A decrease in the water content of IVD tissue results in decreased pore size of the tissue (Holm and Nachemson, 1982; Bibby et al., 2002; Adams and Hutton, 1986; Drew et al., 2004; Kraemer et al., 1985; Ohshima et al., 1989; Adams and Hutton, 1983; Iatridis and ap Gwynn, 2004; Jackson et al., 2008). Because the main factor governing the relative diffusivity in cartilaginous tissues is the ratio of solute size to the pore size of the tissue (Gu et al., 2004; Maroudas et al., 1975) see equation (3-6), compression would contribute to a decrease in the diffusivity of

oxygen in the tissue. Recent studies have also shown the existence of microtubes, which are small (~10 μm in diameter) tubular structures that extend along the direction of collagen fiber bundles, in bovine and murine AF (Iatridis and ap Gwynn, 2004; Travascio and Gu, 2007; Jackson et al., 2008). These microtubes have been suggested as a pathway for solute transport through AF tissue (Jackson et al., 2008; Travascio and Gu, 2007). We believe that, when compression is applied to the tissue, tissue compaction may also cause a reduction in the size of the microtubes which, in turn, leads to a decrease in the solute diffusivity in the tissue. Therefore, the strain-dependence of oxygen diffusivity in bovine AF can likely be attributed to the decreased tissue porosity and pore size, at both the nano- and micro-levels, caused by compression.

The results for oxygen diffusivity in human AF tissue are similar to those found in bovine AF in the current study, as well as results reported in a recent study (Jackson et al., 2008), with differences being attributed to microscopic differences in the tissue structure for human and bovine AF. The results from the current study did not show a significant difference in oxygen diffusivity among the three principal directions in human AF tissue. However, previous studies have shown that transport of other molecules in IVD tissues is anisotropic (i.e., direction-dependent) (Jackson et al., 2008; Chiu et al., 2001; Travascio and Gu, 2007; Jackson et al., 2006; Hsu and Setton, 1999; Travascio et al., 2009). For instance, earlier studies have shown that, for bovine AF tissue, diffusivity in the axial direction is approximately 1.5 times that in the radial direction (Jackson et al., 2008; Travascio and Gu, 2007). Although there was no significant anisotropic trend found for oxygen diffusivity, this is likely due to the low number of samples used, and the high standard deviation resulting from variability in human tissue specimens. Therefore, these

studies will be continued using more human discs and a greater number of specimens, in order to better determine if an anisotropic trend exists.

It was also determined that mechanical compression reduces diffusivity of oxygen in human AF tissue. This is similar to previous results for diffusion of oxygen and glucose in bovine AF tissue (Jackson et al., 2008), as well as results for water diffusivity in ovine IVD tissues (Drew et al., 2004). The reduction in diffusivity in compressed tissue is likely the result of water exudation and structural changes caused by mechanical strain.

In summary, this study measured the oxygen diffusivity of bovine AF in the axial direction, and was the first study to report stain-dependent oxygen diffusivity in AF. This is also the first study to investigate the anisotropic and strain dependent behavior of oxygen diffusion in human AF tissue. Results in the current study show that mechanical loading affects the oxygen diffusivity in both bovine and human IVD tissue, decreasing as the compression increases. The findings from this study provide an additional insight into the nutrition transport in IVD under mechanical loading and highlight the importance of approaching and understanding mechanisms of nutrient transport in IVD tissue. This information is important to the development of numerical models for nutritional transport in IVD tissues.

CHAPTER 4. EFFECTS OF LOW GLUCOSE CONCENTRATIONS ON OXYGEN CONSUMPTION RATES OF INTERVERTEBRAL DISC CELLS

4.1 BACKGROUND

Transfer of water and small solutes such as glucose and oxygen, from the blood vessels surrounding the periphery of the disc and vertebral body, is mainly accomplished by diffusion (Urban et al., 1982; Katz et al., 1986). The balance between the rate of solute diffusion through the matrix and the rate of consumption by NP and AF cells determines the resulting concentration gradient inside the disc. Studies show that when end-plate permeability or solute diffusivity decreases, concentrations of glucose, oxygen, and pH levels decrease towards the center of the disc (Selard et al., 2003). The lowest concentrations of glucose and oxygen will be in the center of disc. The highest metabolite concentration of lactic acid, resulting in the low pH, will be in the center, too. Therefore, nutrient supply could fall to such a low level that cells do not have enough nutrients to maintain viability. Eventually, if the permeability of the end-plate decreases the cells in the center of the disc may die.

To our knowledge there are only a few studies that have appeared in the literature that investigate the rates of oxygen and glucose consumption of IVDs (Holm et al., 1981; Bibby et al., 2005; Ishihara and Urban, 1999). Bibby et al examined the isolated bovine NP cells at varying oxygen, glucose, and pH levels in vitro. They found that there was no effect of glucose concentration on oxygen consumption over the range of 1 to 5 mmol/L. However, the oxygen consumption rate was pH dependent. When pH value decreased, the oxygen consumption rate at high oxygen concentration also decreased. At low oxygen concentration, this effect was less significant than at high oxygen concentration (Bibby et

al., 2005). Ishihara and Urban found that oxygen consumption rate fell when oxygen concentration decreased from 21% to 1% at constant glucose concentration and pH levels (Ishihara and Urban, 1999).

However, the oxygen consumption rate of AF cells at in vivo levels of glucose has not been investigated. Previous theoretical analysis showed a steep gradient of glucose concentration within the AF region (Selard et al., 2003). Based on the previous theoretical analysis, the objectives of this chapter are to develop a new method to determine the rate of oxygen consumption of NP and outer AF cells and to obtain quantitative information for oxygen consumption rates of cells under different glucose concentrations.

4.2 THEORY

The rates of oxygen consumption can be calculated using the Michaelis-Menten equation, which can be expressed as follows:

$$R = \frac{V_{max} \times [O_2]}{K_m + [O_2]} \rho \qquad (4\text{-}1)$$

where R is oxygen consumption rate (unit: μM/ hr), V_{max} is the maximum oxygen consumption rate (unit: nmoles/ million cells/ hr), K_m is the Michaelis-Menten constant, $[O_2]$ is the oxygen concentration, and ρ is the cell density in the chamber. The rate of oxygen consumption was also defined as the amount of oxygen concentration changed within the time,

$$R = -\frac{d[O_2]}{dt} \qquad (4\text{-}2)$$

The analytical solution can be derived from equation 4-1, and 4-2

$$t = \frac{K_m}{V_{max}\rho}\ln\left(\frac{[O_2]_0}{[O_2]}\right) + \frac{[O_2]_0 - [O_2]}{V_{max}\rho} + t_0 \qquad (4\text{-}3)$$

During the metabolism experiment, oxygen concentrations in medium were recorded in ppm. The ppm is defined as

$$ppm = \frac{mg}{L} \qquad (4\text{-}4)$$

Mole is defined as

$$mol = \frac{g}{Molecular\ Weight\ (M.W.)} \qquad 4\text{-}5)$$

We then changed the ppm to nmol

$$nmol = \frac{ppm}{M.W.} \times \mu L \qquad (4\text{-}6)$$

The solubility of oxygen is defined as

$$C_{O_2} = HP_{O_2} \qquad (4\text{-}7)$$

where C_{O_2} is the concentration of dissolved oxygen in solution, H is the Bunsen solubility coefficient, and P_{O_2} is the partial pressure of oxygen in the gas phase.

The solubility of oxygen in water at 37°C and one atmosphere (1.013×10^5 Pa) is 1.00×10^{-11} mole ml^{-1} Pa^{-1}. The partial pressure of oxygen at 37°C and one atmosphere is 21% of air pressure; thus the partial pressure of oxygen is 2.1×10^4 Pa. We can get the

concentration of dissolved oxygen in solution at 37°C and one atmosphere by using the equation (3-7),

$$C_{O_2} = 1.00 \times 10^{-11} \frac{mole}{ml\ Pa} \times 2.1 \times 10^4\ Pa$$
$$= 2.1 \times 10^{-7} \frac{mole}{ml}$$
$$= 2.1 \times 10^{-4} \frac{mole}{L}$$
$$= 2.1 \times 10^{-4}\ M$$

By using the same method, we also can get 5% oxygen pressure at 37°C and one atmosphere is 50μM.

4.3 MATERIALS AND METHODS

Cell isolation. Porcine lumbar spines were used for this experiment. Pigs, more than 3 months old and weighing approximately 200 lb, were obtained from a local slaughterhouse and dissected within 4 hours of death.

After carefully removing the excess tissue and ligaments surrounding the discs, each disc was removed. Lumbar spines were then washed with phosphate-buffered saline (PBS) (14190; Invitrogen Corp., Carlsbad, CA) with 1% antibiotic-antimycotic (15240, Invitrogen Corp., Carlsbad, CA) 3 to 4 times. The spines were then moved to biological safety cabinets. Before opening the discs, spines were wiped with 70% isopropyl alcohol. Discs were dissected into NP and AF from the outer IVD region. NP and outer AF tissues were placed in cold Hank's balanced salt solution without calcium or magnesium (HBSS) (14170, Invitrogen Corp., Carlsbad, CA) plus 1% antibiotic-antimycotic. AF from the outer IVD region were chopped extra finely. Cells isolated from NP and outer AF were

then centrifuged at 1000 rpm for 15 min, re-suspended in enzyme solution and placed at 37°C overnight. Tissues were digested by adding the following to 1 ml of Dulbecco's Modified Eagle Medium (DMEM) (12430, Invitrogen Corp, Carlsbad, CA): 1 mg Collagenase type II (4176, Worthington Biochemical Corp., Lakewood, NJ), 0.6 mg protease type I (P4630, Sigma Aldrich Corp., St. Louis, MO) and 1% antibiotic-antimycotic (Maldonado and Oegema, Jr., 1992).

At the end of the digestion period, cells were centrifuged at 1000 rpm for 15 min and washed three times in PBS. The resulting digestions were then passed through a sterile 70 μm cell strainer (352350, BD Biosciences, Bedford, MA) and re-suspended in DMEM containing 10% fetal bovine serum (FBS) (16000, Invitrogen Corp Carlsbad, CA) and 1% antibiotic-antimycotic.

Agarose disc sample preparation. Isolated cells were re-suspended in DMEM containing 10% FBS and 1% antibiotic-antimycotic and adjusted to have the density of twenty million cells per milliliter. A 4% low melting agarose (A9045, Sigma Aldrich Corp., St. Louis, MO) solution was made in sterile phosphate-buffered saline to mix with the isolated cells in 1:1 volume to obtain the final concentration of 2% agarose solution at a nominal density of ten million cells per milliliter. The solution was then poured into a mold to make agarose discs with the dimensions of 8 mm diameter and 1 mm thickness (Figure 4-1). After waiting for agarose gel to reach the room temperature, discs were then removed from the mold and placed in the culture dish. Those discs were then incubated for one day in DMEM containing 10% FBS, and 1% antibiotic-antimycotic at 37°C. Three-dimensional agarose culture has been shown to maintain the phenotype of IVD cells (Gruber et al., 1997; Gruber et al., 2004) .
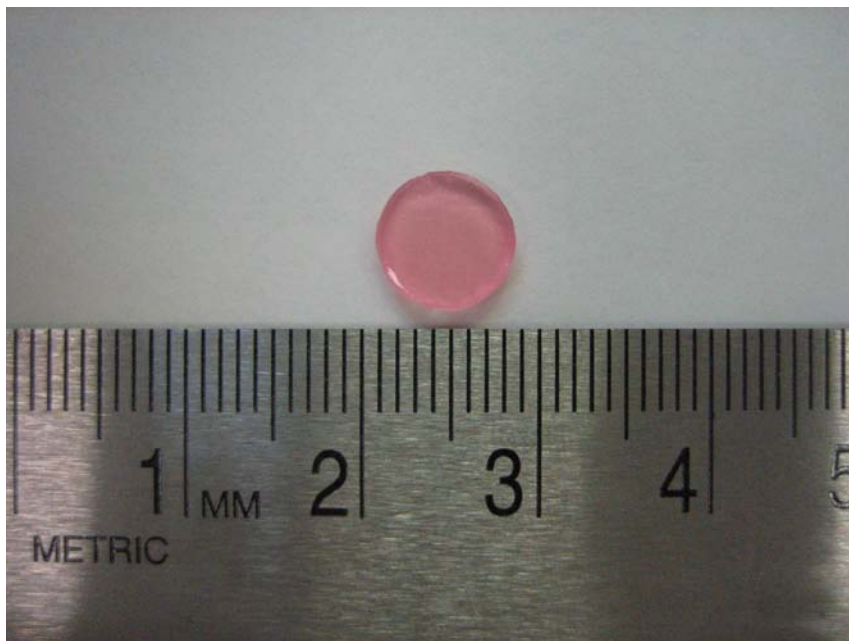
Figure 4-1: 2% agarose disc with 10 million AF cells of porcine lumbar inside. The dimensions of disc are 8 mm diameter and 1 mm thickness

Metabolism chamber. A custom-made acrylic (Small parts, Miami Lake, FL) metabolism chamber was designed and built to measure oxygen concentrations during cell metabolism (Figure 4-2). The metabolism chamber consists of a main center compartment with the volume of 330μl. Discs were placed in the center compartment during the cell metabolism experiment. An opening through a hole at the bottom of the center compartment was connected to a constant temperature circulator (Fisher Scientific International Inc., Hampton, NH) to maintain a constant temperature of 37°C. Two other holes were made on the side of center compartment. The hole on the upper side was used to release air bubbles and to release the pressure produced by closing the lid of the center compartment, and the lower side hole was used to insert the oxygen probe into the main center compartment. A 5 × 2 mm micro stir bar (Chemglass, Vineland, NJ) was placed inside the center compartment during the experiment in order to maintain the uniformity of the solution. The whole chamber was placed in a Styrofoam box, used to maintain a constant temperature during the experiment.

Experiment protocol. After agarose discs were made, they were incubated in DMEM containing 10% FBS and 1% antibiotic-antimycotic with glucose concentrations of 25 mM at 37°C for one day. Discs were then transferred to DMEM with different glucose concentrations. Each disc was provided with 4 ml of DMEM plus 1% antibiotic-antimycotic and 10% FBS but with glucose concentrations of 1, 2.5, 5, and 25 mM. Discs were then incubated for 24 hours to allow cellular glycogen levels to adapt to low glucose concentrations.
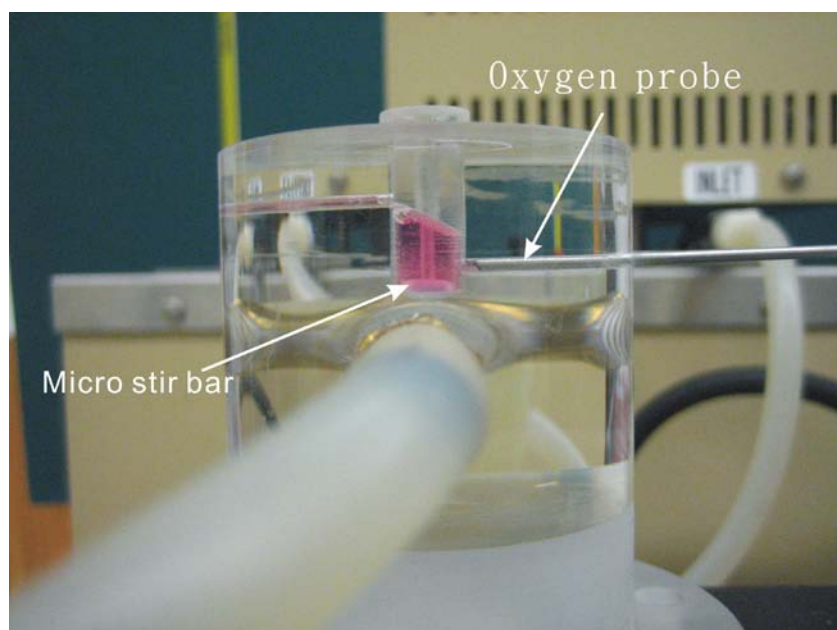
Figure 4-2: Custom-made acrylic metabolism chamber.
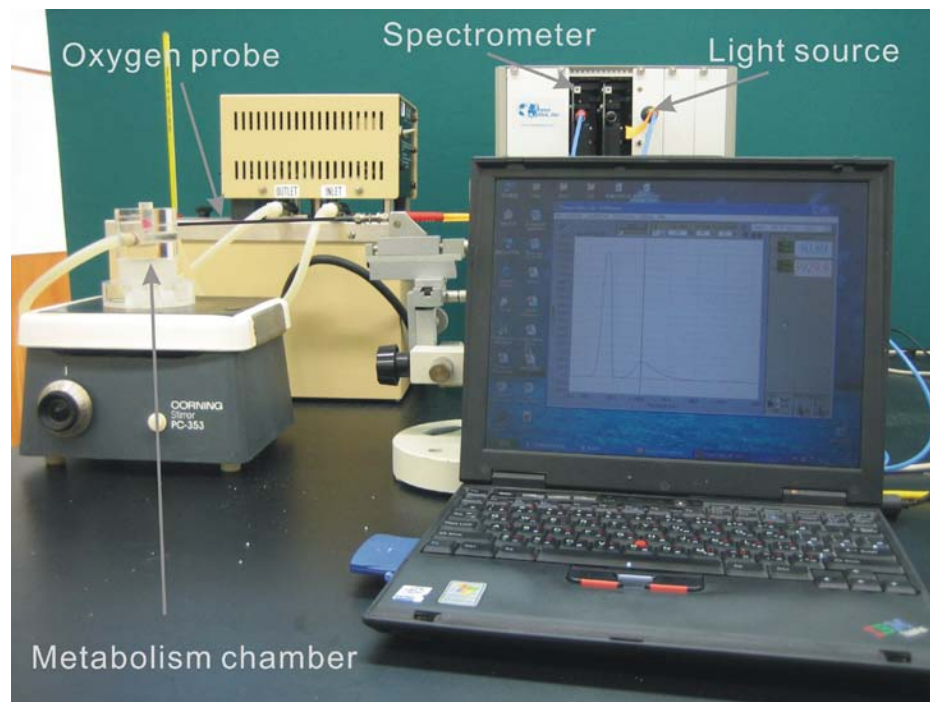
Figure 4-3: Foxy Fiber Optic Oxygen Sensor System.

Before beginning the experiment, several steps were taken to set up the oxygen metabolism chamber. First, the oxygen metabolism chamber and the lid were exposed to UV light for several hours, and the oxygen probe was washed with 10% bleach and then washed with sterile PBS to remove the extra bleach solution.

After the probe was inserted into the oxygen chamber, the whole apparatus was fixed in position to reduce error caused by moving the oxygen probe. The oxygen probe was then calibrated using the two-point method. The whole procedure was done in the manner similar to that discussed in the oxygen measurement (see section 3.3).

As soon as the calibration was done, the chamber was filled with fresh DMEM with the same concentrations as in the 24-hr incubation and pH 7.4 at 37°C. The agarose disc was then cut into small pieces (about 1 mm cubes) in order to minimize the concentration gradient of glucose and oxygen within the agarose gel and then placed into oxygen metabolism chamber. The chamber was sealed after allowing cells to calm down for several minutes. Care was taken when sealing the oxygen metabolism chamber to ensure that air bubbles, which could greatly affect the oxygen concentration, were not created when closing the chamber. The real time oxygen concentration was recorded by the oxygen sensor system during the whole experiment until the oxygen concentrations achieved equilibrium.

At the end of the experiments, the glucose concentration of the culture medium was measured using a quantitative enzymatic assay (G3293, Sigma Aldrich, St. Louis, MO) and the pH of the culture medium was examined using a pH meter (Φ340 pH, Beckman Coulter, Inc, Fullerton, CA). In this study, decrease in glucose concentration was found to be minimal whereas pH in the culture medium did not alter after the

experiment. Furthermore, cells were released from agarose samples by the 3-hr digestion in 2 ml PBS containing 200 μg/ml agarase (A6306, Sigma Aldrich, St. Louis, MO) at 37°C. Total number of cells was determined again and cell viability was examined by trypan blue (25-900-CI, Mediatech, Inc., Herndon, VA) exclusion. The average of cells number per disc was 1.2×10^6 cells and more than 90% of cells were viable. The cells did not proliferate much in the agarose gel since the average cell density did not have much difference before and after the experiments.

4.4 RESULTS

Typical results, showing the experiment data and theoretical curve fittings plotted for experiments of NP and AF cells, are shown in Figure 4-4. Values of oxygen concentration were recorded every two seconds. There was good agreement between the experimental data and the theoretical curve fitting for AF (R^2=0.994 ± 0.005) and NP (R^2=0.997 ± 0.003) cells.

V_{max} and K_m were determined by curve-fitting the experimental data with equation (4-3) using MATLAB (MathWorks, Natick, MA). V_{max} of different regions under different glucose levels is shown in Figure 4-5. There was a significant difference in V_{max} of AF cells found between different glucose levels of medium. AF cells cultured at low glucose concentration (1mM) had a higher V_{max} than cells cultured at high glucose concentration (25mM). However, there was no significant difference found in V_{max} of NP cells cultured under different glucose levels.

K_m of different regions under different glucose levels is shown in Figure 4-6. There was no significant difference found for K_m under different glucose levels for either NP or AF cells.

The average V_{max} and K_m of AF and NP cells are shown in Figures 4-7 and 4-8. There was a significant difference, found in average K_m of different regions. K_m and V_{max} of the AF cells was found to be significantly greater than NP cells (p<0.001). V_{max} of the NP cells was found to be significantly greater than AF cells. V_{max} and K_m determined for outer AF and NP cells from theoretically curve fitting are shown in Table 4-1.

Figure 4-9 shows the rate of oxygen consumption of cells in different regions under different glucose levels at the level of 5 % oxygen tension (i.e., in vivo condition). The oxygen consumption was lower for outer AF cells cultured in the highest glucose medium (25mM) than outer AF cells cultured in the lowest glucose medium (1mM) (p=0.035) (Figure 4-9). The total average of oxygen consumption at 5% oxygen tension is shown in Figure 4-10. The rates of oxygen consumption of NP cells were significantly higher than those of the outer AF cells (p<0.001).
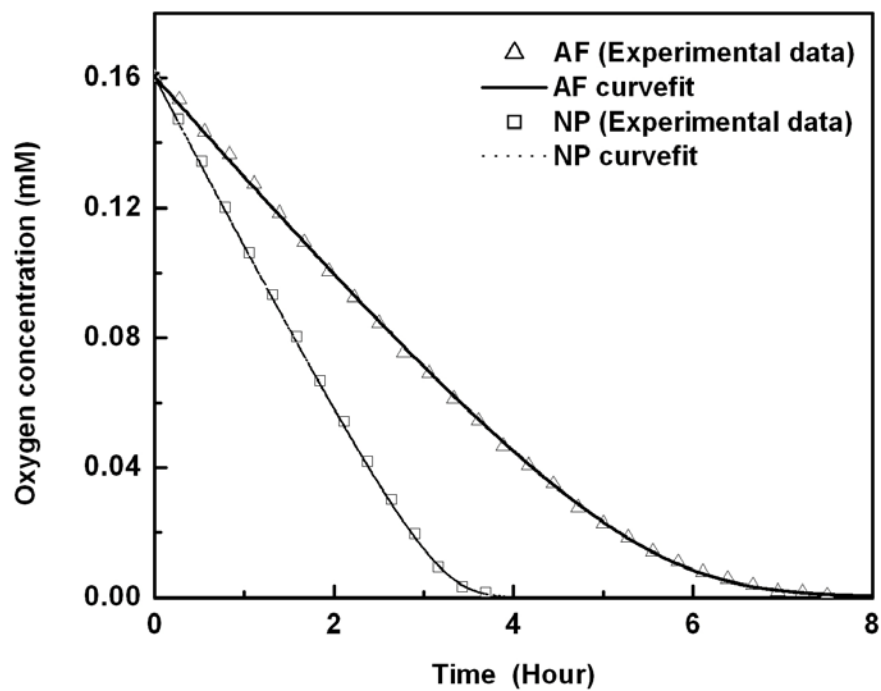
Figure 4-4: Typical curve-fit results by using Eq. 4-3. Plots of experimental data and theoretical curve-fitting of NP and AF cells both cultured under glucose concentration of 1mM.
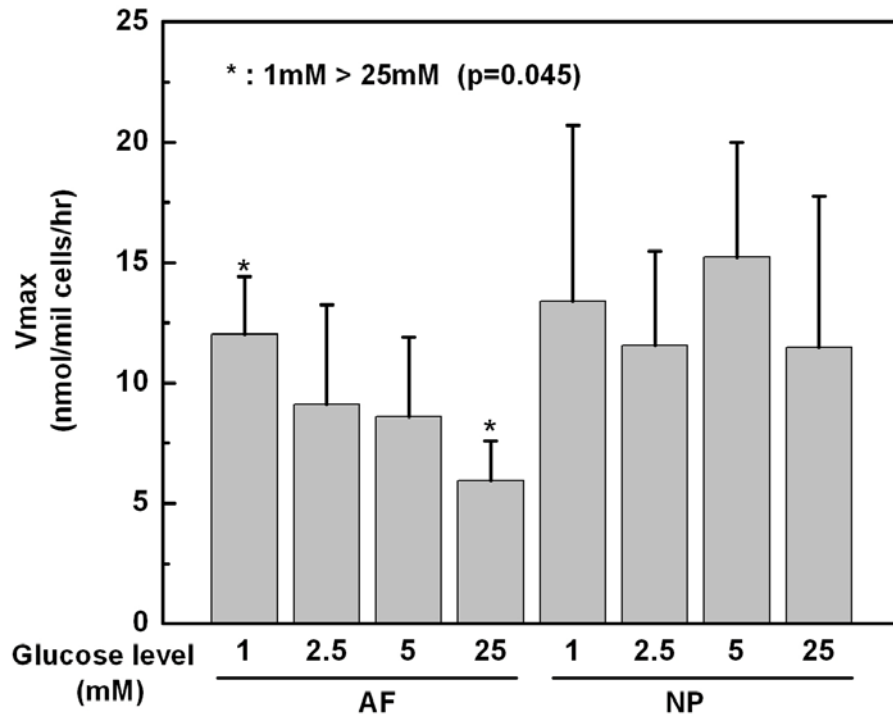
Figure 4-5: Comparison of V_{max} among the outer AF or NP cells cultured in the media with different glucose concentrations (n=5 for each group)
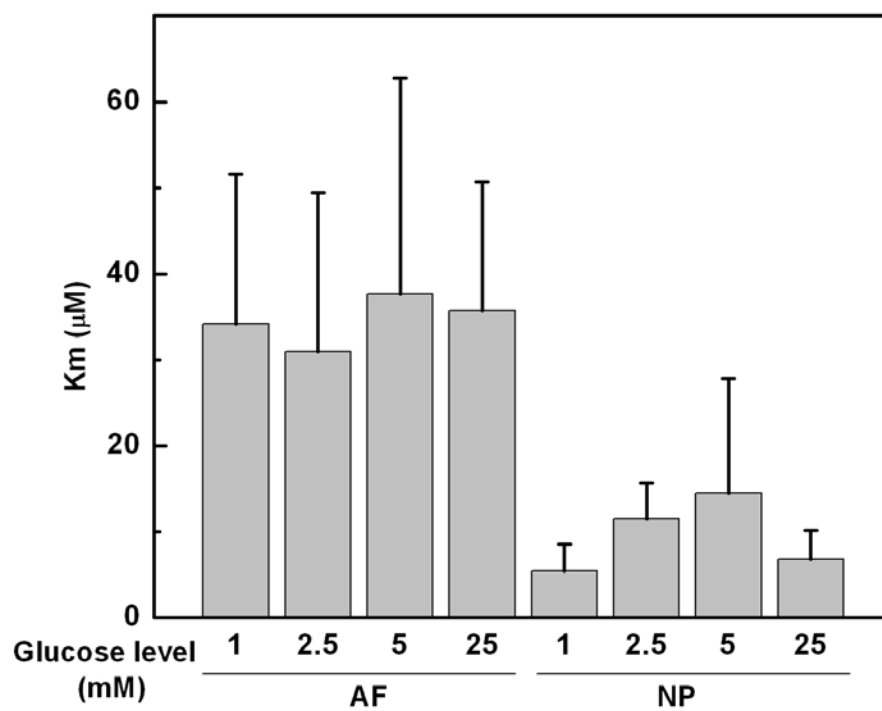
Figure 4-6: Comparison of K_m among the outer AF or NP cells cultured in the media with different glucose concentrations (n=5 for each group)
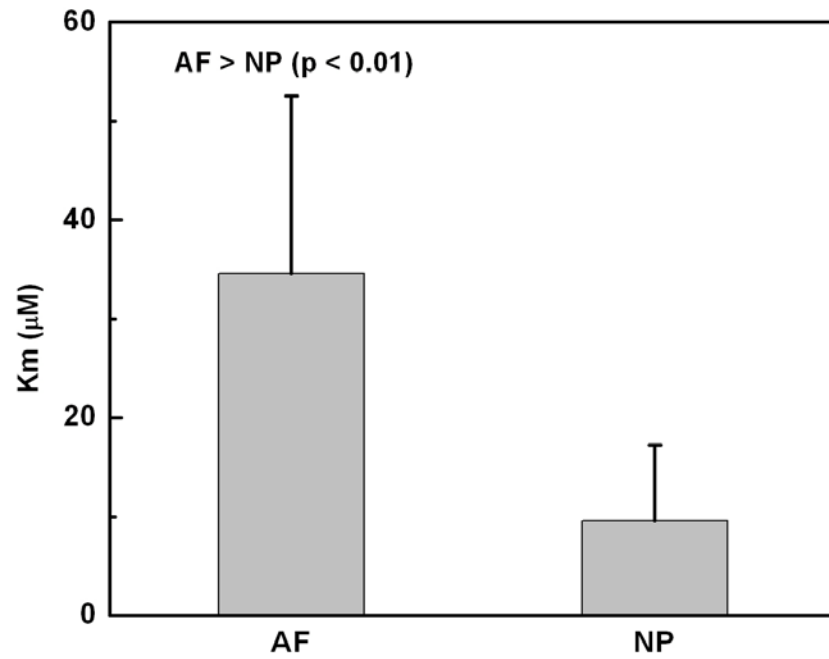
Figure 4-7: Comparison of the average of K_m between the outer AF or NP cells (n=20 for each group).
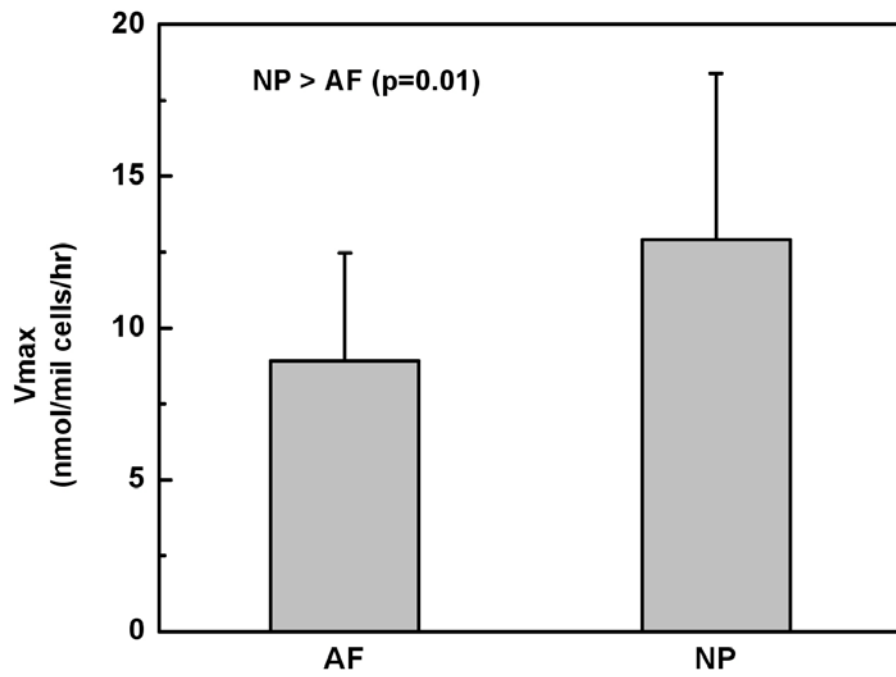
Figure 4-8: Comparison of the average of V_{max} between the outer AF or NP cells (n=20 for each group).
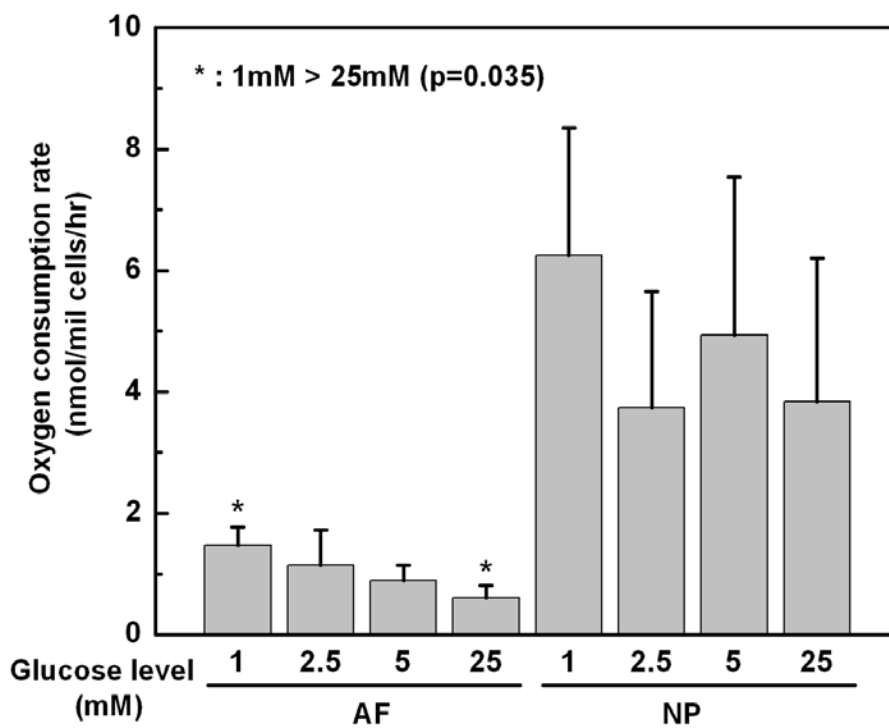
Figure 4-9: Comparison of oxygen consumption rate at 5% (50μM) oxygen tension among the outer AF or NP cells cultured in the media with different glucose concentrations (n=5 for each group). The oxygen consumption rate was calculated using equation (4-1) based on V_{max} and K_m which were determined from theoretical curve fitting.
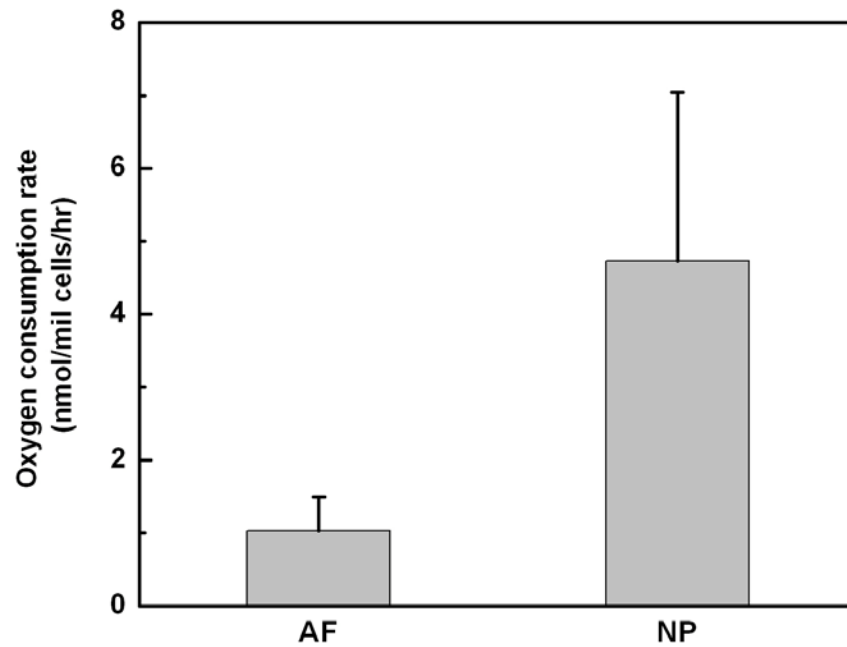
Figure 4-10: Comparison of oxygen consumption rate at 5% (50μM) oxygen tension between the outer AF and NP cells (n=20 for each group). The oxygen consumption rate was calculated using equation (4-1) based on V_{max} and K_m which were determined from theoretical curve fitting.

Table 4-1: V_{max} (nmol/million cells/ hr) and K_m (µM) of NP and AF cells

Glucose concentration	Outer AF		NP	
	V_{max}	K_m (µM)	V_{max}	K_m (µM)
1 mM	12.0±2.4	34.1±17.5	13.4±7.3	5.5±3.1
2.5 mM	9.1±4.2	31.0±18.4	11.6±3.9	11.5±4.2
5 mM	8.6±3.3	37.7±25.1	15.2±4.8	14.5±13.3
25 mM	6.0±1.6	35.7±14.9	11.5±6.3	6.8±3.3
Average	8.9±3.6	34.6±17.9	12.9±5.5	9.6±7.7

4.5 DISCUSSION

Bibby et al. (2005) found previously that the rate of oxygen consumption of bovine NP cells was not regulated by glucose levels. The results of the current study also showed that different glucose levels did not affect the rate of oxygen consumption of NP cells as expected. However, AF cells have a lower rate of oxygen consumption when they cultured in the high glucose medium compared to those cultured in the low glucose medium. There was no significant difference found when AF cells were cultured at physiological levels of glucose such as 1 mM, 2.5 mM, 5 mM glucose. In general, the rate of oxygen consumption of NP and AF cells was not affected by the different glucose levels when cultured at physiological levels.

The effect of oxygen tension on the rate of oxygen consumption is shown in Figure 4-11. In both regions of the disc, the rate of oxygen consumption fell as the oxygen concentration decreased. The oxygen consumption rate of the NP cells in the current study was found to be similar to canine NP cells but higher than that of bovine NP cells (Figure 4-11). The rates of oxygen consumption of all NP cells were higher than AF cells. This indicates that the oxygen consumption rate of inner and outer AF cells may be different. Although the rate of oxygen consumption of bovine NP cells is lower than those of NP cells of porcine and canine lumbar discs, they are of the same order of magnitude. The differences may be due to different species and harvest sites.

The rate of oxygen consumption of AF cells remained more or less constant until oxygen tension decreased to 5% and then fell steeply as the oxygen tension decreased. This is similar to the study by Ishihara et al (Ishihara and Urban, 1999). They found that the oxygen consumption rate of the outer AF tissue of bovine caudal disc remained

constant at high level of oxygen tension but strongly depended on the level of oxygen tension when oxygen tension was lower than 5%.

Although the oxygen consumption rate of outer AF tissue of bovine caudal disc cannot be compared to the data of this study because of the lack of information about its cell density, the oxygen consumption rate of porcine AF cells at high oxygen tension (i.e. V_{max}) in this study is comparable to that of cells in other avascular tissue such as articular chondrocytes, reported in the range of 1.7–17 nmol/million cells/hr in recent studies (Malda et al., 2004; Heywood et al., 2006; Chen et al., 2006).

Osmolarity (ranging from 316–600 mOsm) was shown to have little effect on the oxygen consumption rate of bovine articular chondrocytes (Heywood et al., 2006). In this study, since osmolarity of medium with different glucose concentrations was found to be in a small range (314-335 mOsm), it was assumed to have minimal effects on the measurement of oxygen consumption rate.

The effects of pH on the rate of oxygen consumption in AF and NP cells were not investigated in the current study; however, the rate of oxygen consumption of bovine cells was regulated by pH in the previous study (Bibby et al., 2005). Therefore, it could be expected that the rate of consumption of AF cells be also regulated by pH.
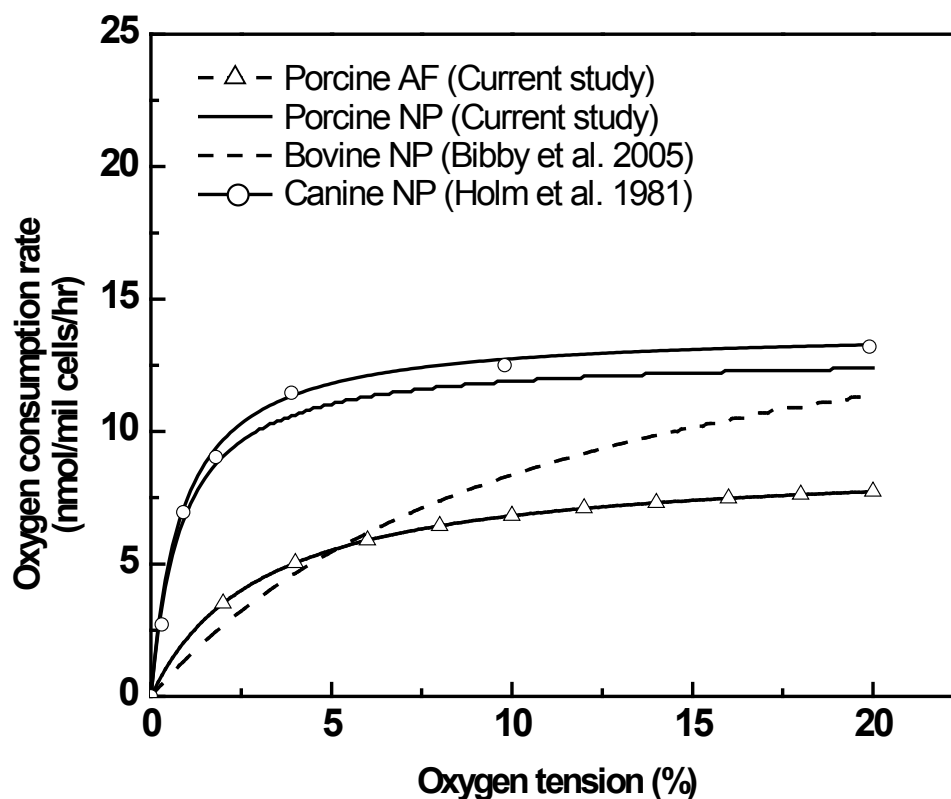
Figure 4-11: Comparison on oxygen consumption rate within the range of oxygen tension from 0 to 20% (i.e., 0 to 210 μM) between this study and literatures. The consumption rate of bovine NP cells at pH 7.4 was calculated based on the modified Michaelis-Menten equation proposed in the study of Bibby et al. The oxygen consumption rate of canine NP cells was converted from the oxygen consumption of canine NP tissue based on its cell density reported in the study of Holm et al.

Based on the modified Michaelis-Menten equation used to describe the pH dependent oxygen consumption rate of bovine NP cells (Bibby et al., 2005), V_{max} and K_m will decrease to zero at pH 4.95 and pH 4.59, respectively. A similar equation can be proposed to describe possible pH dependence for oxygen consumption rate of porcine NP and AF cells based on the average values of V_{max} and K_m and expressed on a per cell basis as:

$$R_o = \frac{V'_{max}(pH - 4.95)C}{K'_m(pH - 4.59) + C}$$

(4-8)

where V′max (pH-4.95) is the pH dependent maximum consumption rate (V′max= 5.27 nmol/million cells/hr for NP cells and 3.64 nmol/million cells/hr for outer AF cells), K′m (pH-4.59) is the pH dependent Michaelis-Menten constant (K′m = 3.4 μM for NP cells and 12.3 μM for outer AF cells), and the unit of oxygen concentration C is the same as K′m. This can be utilized in the theoretical analysis on oxygen transport in the IVD tissue.

The method used to determine the rate of oxygen consumption from previous studies was to determine the "average" rate of oxygen consumption of cells for the oxygen tension of interest by taking the ratio of the change in oxygen concentration over a short time period. However, this method may not precisely describe the rate of oxygen consumption at K_m because the rate of oxygen consumption would change promptly when oxygen tension was around K_m.

In the current study, an analytical solution derived from the Michaelis-Menten equation was used to accurately describe the V_{max} and K_m. Oxygen concentration was recorded every other two seconds throughout the metabolism experiment, and all the

experimental data points (at least 20,000 data points) from the oxygen concentration measurement were used in theoretical curve fitting. This large number of data points provided a high degree of reliability on theoretical curve fitting. There were very good agreements between the experimental data and the theoretical curve fitting for AF (R^2=0.994±0.005) and NP (R^2=0.997±0.003) cells; therefore, V_{max} and K_m are believed to have been accurately determined. The results of oxygen consumption rate in the current study were consistent with the results from previous studies; therefore, a new method to determine the rate of oxygen consumption has developed. This new method can be an alternative method for determining rate of oxygen consumption.

CHAPTER 5. ONLINE CHARACTERIZATION OF MECHANO-ELECTROCHEMICAL PROPERTIES OF CARTILAGINOUS TISSUES

5.1 BACKGROUND

Cartilaginous tissues (e.g., articular cartilage and intervertebral disc) are avascular, charged, hydrated soft tissues (Grodzinsky, 1983; Maroudas, 1979; Mow et al., 1992). The complex and unique extracellular matrix (ECM) structure make cartilaginous tissues able to function during our daily activity. ECM of cartilaginous tissues consists of a collagen-proteoglycan network, abundant interstitial water (~80%), and ions- mainly sodium (Na^+) and chloride (Cl^-). The charged nature of the ECM is derived from the charged groups on the glycosaminoglycan (GAG) chains of proteoglycans (PGs) (Grodzinsky, 1983; Maroudas, 1979; Mow et al., 1992; Muir, 1983; Muir, 1980). These charges are fixed to the ECM, thereby being known as fixed charge density (FCD), and attract opposite ions in the interstitial fluid to give rise to physicochemical effects within tissues, such as Donnan osmotic pressure and swelling (Eisenberg and Grodzinsky, 1985; Lai et al., 1991; Urban and Maroudas, 1981; Urban and McMullin, 1985; Urban and McMullin, 1988; Donnan, 1924; Eisenberg and Grodzinsky, 1987; Gu et al., 1997a; Gu et al., 1993). PGs contribute significantly to load support and swelling behavior (Akizuki et al., 1987; Armstrong and Mow, 1982b; Eisenberg and Grodzinsky, 1985; Lai et al., 1989; Lai et al., 1991; Maroudas, 1975; Maroudas, 1979; Myers et al., 1984; Armstrong and Mow, 1982a), and are synthesized by chondrocytes within the tissue (Bayliss and Johnstone, 1992). The cell population in cartilaginous tissue accounts for less than 1% of the total volume in the tissue (Stockwell, 1979). Because of the avascular nature of cartilaginous tissues, proper cellular nutrition is dependent upon adequate transport of

fluids and solutes through the tissue. The ECM plays an important role in maintaining cell survival because it controls the transport of these fluids and solutes.

Cartilaginous tissues do not have the ability to self-regenerate when damage occurs. Tissue engineering offers an alternative to the conventional approach of medications and surgical procedures to repair or replace injured tissues through the use of engineered constructs. In order to understand the complex phenomena associated with engineered constructs, highly specialized apparatuses must be designed to monitor the mechano-electrochemical signals present in the surrounding environment (Mow et al., 1999). Bioreactors can be utilized to monitor and control these signals. Before these stimuli can be manipulated to create an optimal cell environment, several material properties (such as water volume fraction and FCD) must be measured in real time. Current bioreactor technology requires engineered constructs to be removed and tested via chemical assay in order to determine their material properties. Therefore, the objective of this project is to develop a novel measurement method that is capable of noninvasively online-characterizing the material properties and biochemical signals within an engineered tissue. The system was designed to work with cartilaginous tissue engineering applications and will enhance the understanding of connective soft tissue mechanobiology, mechanisms of signal transduction, and etiology of tissue degeneration.

5.2 THEORETICAL BACKGROUND

Streaming potential is a mechanical-to-electrical transduction phenomenon in charged porous materials (Helfferich, 1962; Katchalsky and Curran, 1975). The negatively charged groups on the proteoglycans within the cartilaginous tissues are responsible for the streaming potential. The measured streaming potential ($\Delta\psi$) of

charged tissue in a steady permeation test is related to the hydraulic permeability (k), electrical conductivity (χ), applied pressure (Δp) and fixed charge density (FCD, c^F) by (Maroudas, 1968; Helfferich, 1962; Katchalsky and Curran, 1975; Gu et al., 1993):

$$\Delta \psi = \frac{-F_c c^F k \Delta p}{\chi},$$

(5-1)

where F_c is Faraday's constant. By measuring $\Delta\psi$, k, and χ, we can determine the c^F of tissue. The hydraulic permeability (k) can be determined by:

$$k = \frac{Qh}{\Delta p A}$$

(5-2)

where Q is volumetric flow rate (volume per unit time), h is the thickness of sample, Δp is the pressure difference across the sample, and A is the cross-sectional area of the sample. Hydraulic permeability is an important transport property of avascular cartilaginous tissues. Its magnitude governs the rates of fluid flow. Because the value of hydraulic permeability of cartilaginous tissue is very low, a precise measurement of the hydraulic permeability is always a challenge. The hydraulic permeability of the sample can be determined by applying a constant volumetric flow and measuring the pressure difference across the sample in a 1-D permeation test (Gu et al., 1999b; Maroudas et al., 1968; Weiss and Maakestad, 2006).

The electrical conductivity (χ) of a sample is defined as:

$$\chi = \frac{h}{\Omega A}$$

(5-3)

where Ω is the resistance of the sample, h is the sample thickness, and A is the cross-sectional area of the sample. Therefore, the conductivity of the sample can be determined by measuring the resistance. Electrical conductivity (a material property) plays an important role in mechanical-electrical transduction phenomena observed in cartilaginous tissues, such as streaming potential (Gu et al., 1999c; Maroudas, 1968; Gu et al., 1993; Chen et al., 1997; Grodzinsky, 1983; Grodzinsky et al., 1978; Lee et al., 1981; Lotke et al., 1974; Garon et al., 2002). The electrical conductivity of cartilaginous tissues has been studied and in general, has been found to be dependent on fixed charge density (FCD), ion diffusivities, ionic strength and pH values of the bathing solution, hydraulic permeability, and tissue water content (Gu et al., 1998; Gu et al., 2002; Maroudas, 1968; Helfferich, 1962; Chammas, 1989; Gu et al., 1999a; Hasegawa et al., 1983).

Several studies have investigated the relationship between conductivity and water volume fraction (i.e., porosity) for biological soft tissues (Gu et al., 2002; Schepps and Foster, 1980; Smith and Foster, 1985). It was found that for high water content tissues and protein solutions, there exists a linear correlation between conductivity and water volume fraction (Gu et al., 2002; Schepps and Foster, 1980; Bull and Breese, 1969). Because of the mechano-electrokinetic coupling effect, the value of conductivity of a tissue with fluid flow condition and the measured electrical conductivity (χ) of a tissue in NaCl solution is related to ion diffusivities (D^i, $i = +,-$) by (Maroudas, 1968; Helfferich, 1962; Katchalsky and Curran, 1975):

$$\chi = \frac{F_c^2 \phi^w \left(c^+ D^+ + c^- D^- \right)}{RT},$$

(5-4)

where R is the universal gas constant and T is the absolute temperature. When the resistance of a sample is measured in a physiological medium that usually comprises of two major salt components, Na$^+$ and Cl$^-$, the Na$^+$ concentration (c^+) and Cl$^-$ concentration (c^-) are related through the electroneutrality condition: $c^+ = c^- + c^F$. The ion concentrations within the tissues can be calculated using the ideal Donnan equation.

$$C^+ = \frac{C^F + \sqrt{\left(C^F\right)^2 + 4C^{*2}}}{2},$$

$$C^- = \frac{-C^F + \sqrt{\left(C^F\right)^2 + 4C^{*2}}}{2}$$

(5-5)

where C^* is the concentration of bathing solution.

The tissue diffusivity of ions Na$^+$ and Cl$^-$ can be calculated from a previously developed constitutive relation (Gu et al., 2004):

$$\frac{D^i}{D_o^i} = exp\left[-\alpha\left(\frac{r_s^i}{\sqrt{K}}\right)^\beta\right],$$

(5-6)

where D_o is ion diffusivity in free solution, r^s is the solute size (i.e., hydrodynamic radius), K is the Darcy permeability, and α and β are parameters based on material properties of the tissue. Note, the hydrodynamic radius of solute can be calculated with

$$r_s^+ = \frac{k_b \cdot T}{6\pi\eta D_0}$$

(5-7)

where k_b is Boltzmann's constant, D_0 is the diffusivity in solution, T is the absolute temperature, and η is the solvent viscosity.

5.3 MATERIALS AND METHODS

An apparatus was designed and developed for characterizing the fixed charge density (or PG content) and water content of tissue in real time (Figure 5-1). The apparatus consists of a custom-made acrylic perfusion chamber, a central system, and a flow-rate monitoring system. The central system is defined as: a voltage measurement system, an electrical current supply system, and a pressure applying system. The aforementioned systems are connected to a laptop in order to control input parameters and record experimental data (Figure 5-2).

Perfusion chamber. The development of a perfusion chamber was based on the design of the oxygen diffusion chamber from Chapter 2. The perfusion chamber was composed of three parts: an upstream compartment (2.3 ml), a downstream compartment (1 ml), and a center compartment. The upstream compartment was interfaced with a pressure transducer (PX5500CL-050AV, Omega Engineering Inc, Stamford, CT), a syringe pump (PHD 2000, Harvard Apparatus, Holliston, MA), and a custom-made electrode assembly (Ag/AgCl electrode and stainless-steel current electrode). The downstream compartment was connected to a second pressure transducer (PX5500CL-050AV, Omega Engineering Inc, Stamford, CT), a second electrode assembly, and a digital flow meter (SLG1430-150, Sensirion, Westlake Village, CA) (Figure 5-3). The center compartment of the perfusion chamber was designed and fabricated to accommodate a disc-shaped tissue sample. The concept of the center compartment was designed to be used on different sized tissue samples and also to apply different compressive strain to the tissue sample. Two stainless steel porous plates (Mott Corp., Farmington, CT) with 100 μm pore size and 50% porosity were placed in the center and

downstream compartments to hold the tissue sample. The tissues sample was placed in between porous plates and sealed with an o-ring. The compressive strain of tissues is calculated from the tissues thickness compressed inside the chamber compared to tissue thickness without compression.

Central system. The voltage measurement system consisted of two Ag/AgCl electrodes and an electrometer (Model 6514, Keithley Instruments Inc., Cleveland, OH). The electrical current supply system consisted of two stainless-steel electrodes and a digital sourcemeter (Model 2400, Keithley Instruments Inc., Cleveland, OH). The pressure applying system consisted of both upstream and downstream pressure transducers along with the syringe pump. All of these systems were connected to the central control system, a custom LabView program (version 8.2, National Instruments Corp., Austin, TX) to regulate and monitor fluid pressure, flow rate, electrical current, and voltage within the perfusion chamber, which can determine the streaming potential, electrical conductivity, and hydraulic permeability of the tissue sample by using equations (5-1) and (5-4) simultaneously.

Specimen preparation. To validate the new measurement method, the water content and fixed charge density of tissue samples were determined by real-time, non-invasive tests within the system and then verified by chemical assay (invasive methods). Bovine knee articular cartilage and lumbar annulus fibrosus (AF), from the intervertebral disc, were used for this study. Five cartilage and five axial AF samples were prepared using 6 mm and 8 mm corneal trephines (Biomedical Research Instruments, Inc., Silver Spring, MD) and sledge microtome (Model SM2400, Leica Instruments, Nussloch, Germany) with freezing stage (Model BFS-30, Physitemp Instruments, Inc., Clifton, NJ).

The cartilage samples had a diameter of 6 mm and a thickness of approximately 0.95 mm, while the AF samples were 8 mm in diameter and approximately 0.95 mm in thickness.

Silver/Silver Chloride electrodes. Ag/AgCl voltage electrodes were prepared before the experiment. The Ag/AgCl electrodes were chosen because they satisfy three main requirements for reference electrode system: (1) they are nonpolarizable or reversible; (2) they are easily fabricated; (3) they also offer a great deal of stability and durability. Moreover, they do not significantly contaminate the medium in which they are used; and most importantly, they provide a way to measure the activity of chloride ion in solution without significant junction potentials (Janz and Ives, 1968). The fabrication of the Ag/AgCl electrode is governed by the equilibria:

$$\text{Ag}_{(solid)} \Leftrightarrow \text{Ag}^+_{(solution)} + \text{e}^-_{(metal\ phase)} \tag{5-8}$$

$$\text{Ag}^+_{(solution)} + \text{Cl}^-_{(solution)} \Leftrightarrow \text{AgCl}_{(solid)} \tag{5-9}$$
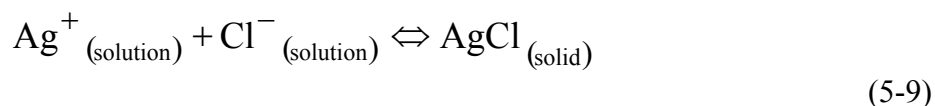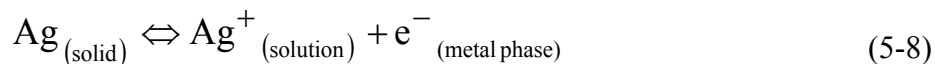
Silver ions and chloride ions are formed by passing an electric current through the electrolyte KCl; this process is known as electrolysis. A silver wire (1 mm in diameter, World Precision Instruments Inc., Sarasota, FL) with length around 10 cm was used as an anode in a solution of 0.1M KCl (P4504, Sigma-Aldrich Corp., St. Louis, MO) and separated from a large stainless steel rod (cathode) in 1M NaCl (S7653, Sigma-Aldrich Corp., St. Louis, MO) by a salt bridge (Figure 5-4). The salt bridge, contained 0.1M KCl in 2% agar (05040, Sigma-Aldrich Corp., St. Louis, MO), allowed the flow of charges but restricts the transfer of solution. The silver wire was insulated by heat-shrink tubing (polyolefin tubing, 3M, St. Paul, MN), so only the end of the 1 mm silver was actually

coated with silver chloride. A magnetic stir bar was using to continuously stir the electrolyte to prevent chloride gas (Cl_2) from impeding the coating process. A current density of 1.0 mA/cm^2 for 45 minutes was used (Gu and Justiz, 2002).

Apparatus validation. The apparatus was calibrated before the experiment in order to verify the apparatus was working properly. A hole (~2 mm) was made in the center of the porous plates. The porous plates were then placed inside of the chamber. Afterwards, the electrodes were carefully inserted through the center holes of the porous plates until they slightly protruded from the surface of the porous plate. The electrodes protruded enough so that when the sample was placed in the chamber, the electrodes would touch both sides of the sample. The perfusion chamber was filled with conductivity standard solution (0.1 M KCl, 12.9mS/cm @ 25 °C) (990106, ThermoFisher Scientific, Waltham, MA) to calibrate the distance between the two electrodes. The four-wire sense mode and the offset-compensation ohm method of the digital sourcemeter were used to minimize the effect of the changes in electrodes impedance on the conductivity measurements. The resistance of the conductivity standard in the perfusion chamber was calculated using the equation (5-3).

In order to calibrate the distance between two electrodes, the initial condition (h, A and χ) must be known. Then a reference Ω was calculated from the equation (5-3). Once the electrodes were in the perfusion chamber, the measured value of Ω was determined. The position of the electrodes were adjusted so that the reference and measured Ω values were equal. The solution was then replaced with phosphate buffered saline (PBS, pH 7.4, Sigma-Aldrich, St. Louis, MO) to be used in the tissue experiment. The conductivity of the PBS solution was measured by the Orion conductivity meter

(Model 125Aplus, ThermoFisher Scientific, Waltham, MA). The PBS conductivity was measured in the perfusion chamber to verify the electrodes.

Experiment protocol. Prior to the experiment, the samples were loaded in the chamber, and the appropriate compression level was applied; for cartilage samples, a 10% compressive strain was applied, while a 50% compressive strain was applied to the AF samples. The structure of AF is described as concentric lamellae that run in transverse directions. With an axial excision of AF tissue, there is inevitably some destruction of the peripheral collagen interconnections. Therefore, a higher degree of compression was necessary to seal the tissue within the o-ring. After equilibrium was established, the electrical conductivity was measured using a four-wire method; a 10 μA current was applied via current electrodes and the resultant tissue resistance was measured via Ag/AgCl electrodes (Gu and Justiz, 2002). Subsequently, the hydraulic permeability and streaming potential tests were conducted simultaneously by applying a fluid pressure difference of 15 psi across the sample. The resultant fluid flow and electrical potential were measured via a digital flow meter and Ag/AgCl electrodes, respectively (Gu et al., 1999b; Gu et al., 1999c).

After the experiment, the samples were extracted from the chamber, weighed, and dried by freezing in a high vacuum lyophilizer (CentriVap benchtop centrifugal concentrators and systems, Labconco, Kansas City, MO) for the direct measurement of water content (Gu and Justiz, 2002; Gu et al., 2002). The water volume fraction (Φ^w) was determined using a density-determination-kit and an analytical balance (Model YDK 01 LP and Model LA 120S, Satorius, Goettingen, Germany) (Figure 5-5). According to Archimedes' principle and biphasic assumption, the water volume fraction of samples

was calculated by the following equation (Gu and Justiz, 2002; Gu et al., 2002; Gu et al., 1996; Yao and Gu, 2002):

$$\phi^w = \frac{W_{wet} - W_{dry}}{W_{wet} - W_{solution}} \frac{\rho_{solution}}{\rho_w} \tag{5-10}$$

where W_{wet} is the specimen wet weight, $W_{solution}$ is the weight of specimen measured in PBS solution (including buoyancy effect); W_{dry} is the lyophilized sample weight, $\rho_{solution}$ is the mass density of PBS solution (1.005 g/ml), and ρ_w is the mass density of water.

The lyophilized samples were digested for 24 hours at 60°C in 1 ml buffer of 100 mM sodium phosphate (S9390, Sigma-Aldrich, St. Louis, MO), and 10 mM EDTA (E5134, Sigma-Aldrich, St. Louis, MO), 10 mM cysteine HCl (pH 7.0) (C1276, Sigma-Aldrich, St. Louis, MO) containing 250 μg/ml papain solution (P4762, Sigma-Aldrich, St. Louis, MO) to analyze the total sulfated glycosaminoglycan (GAG) content of the sample. 1 ml papain solution per 4-40 mg dry weight of lyophilized samples was used. The fixed charge density was calculated based on the total GAG content of the sample. The total sulfated GAG content of the lyophilized samples was determined on a spectrophotometer (SmartSpecTM Plus Spectrophotometer, BioRad, Hercules, CA) using a dimethylmethylene blue (DMMB) dye method (Huang et al., 2007). One hundred microliters of the papain-digested sample was reacted with 2 ml of DMMB dye solution [dissolve 4mg DMMB (03610, Polysciences, Inc., Warrington, PA) in 1.25 ml 100% ethanol (PHARMCO-AAPER, Brookfield, CT), mix it with a stir bar for at least 4 hours at room temperature] in a disposal cuvette and the total GAG content was measured spectrophotometrically at 525 nm. A standard curve was constructed using bovine

chondroitin sulfate A (C9819, Sigma-Aldrich, St. Louis, MO). By assuming 2 moles of charge per mole of GAG in the tissue and a molecular weight of 502.5 g/mole GAG, the c^F can be calculated based on the GAG content from:

$$c^F = B \frac{W_{GAG}}{V_{water}},$$

(5-11)

where $B = \dfrac{2\ mol\ charges}{502.5\ g\ GAG}$, W_{GAG} is the GAG content in the sample, and V_{water} is the volume of water in the sample.

Since the tissue samples were compressed in the perfusion chamber, the water volume decreased and the FCD increased compared to the uncompressed samples. Therefore, the values of water volume and FCD measured within the perfusion chamber need to be converted back to their original status (without compression). For infinitesimal deformation, the water volume fraction is related to the deformation by (Gu et al., 1998; Lai et al., 1991):

$$\phi^w = \frac{\phi_0^w + e}{1 + e},$$

(5-12)

where e is the dilatation related to the infinitesimal strain tensor of the solid matrix E by $e = \text{tr}(E)$; ϕ_0^w is the water volume fraction at the reference configuration (i.e., at $e=0$). In the current study, ϕ^w is the water volume measured in the perfusion chamber, e is the corresponding compressive strain and ϕ_0^w is the water volume at 0% compression. For

infinitesimal deformation, the fixed charge density can be expressed along the tissue deformation as:

$$c^F = \frac{c_0^F \phi_0^w}{1 + e},$$
(5-13)

where c_0^F is the FCD at the reference configuration (e=0). From equation (5-12) and (5-13), conservation of the fixed charge can also be expressed as:

$$c^F = \frac{c_0^F \left(1 - \phi^w\right)\phi_0^w}{\left(1 - \phi_0^w\right)\phi^w},$$
(5-14)

In the current study, c^F is the water volume measured in the perfusion chamber, e is the corresponding compressive strain and c_0^F is the water volume at 0% compression.
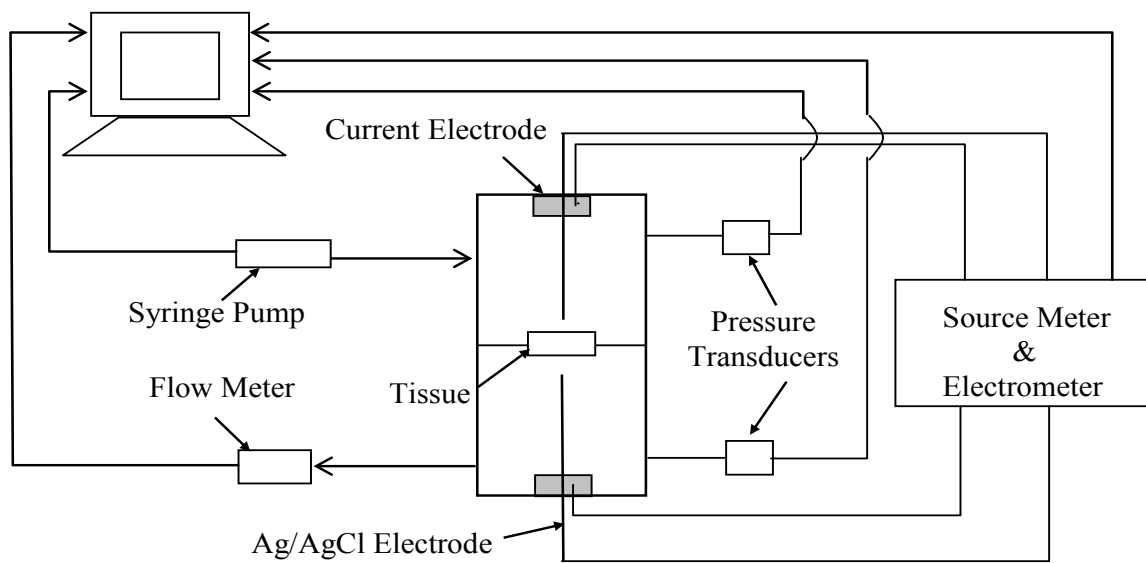
Figure 5-1: Schematic of the apparatus for online monitoring tissue properties.
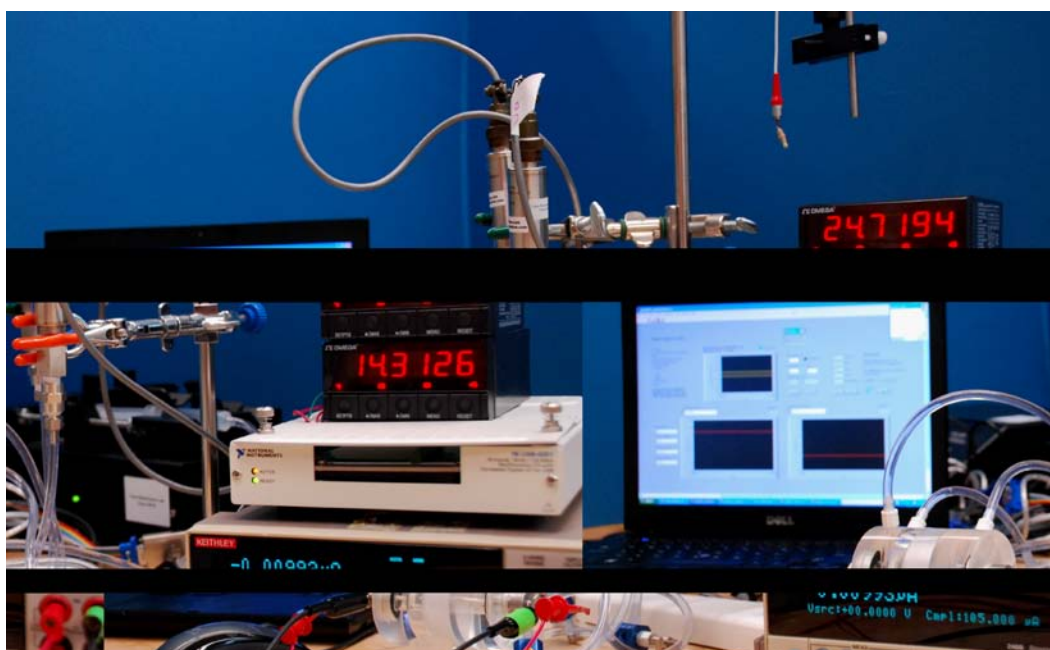
Figure 5-2: photograph of set up of experiment
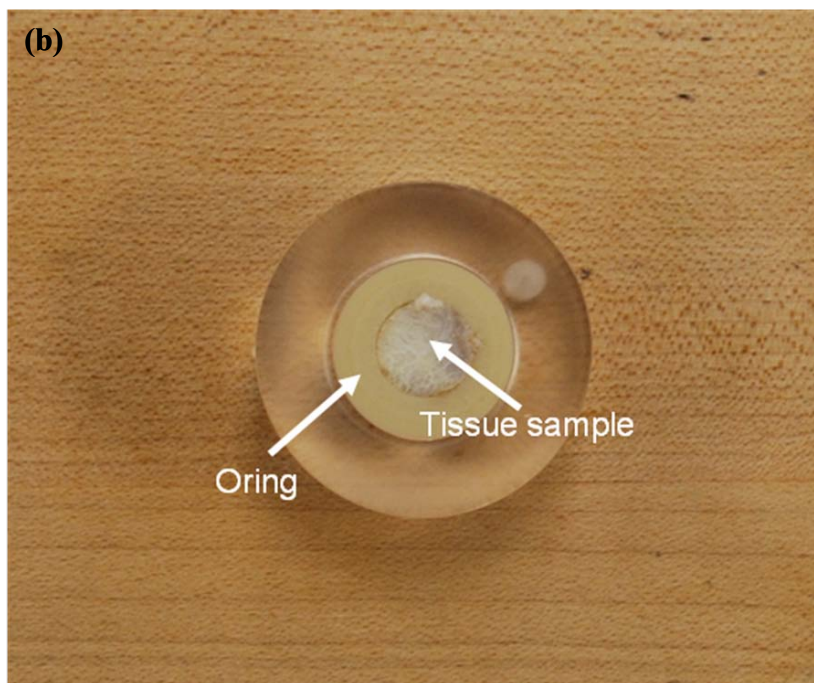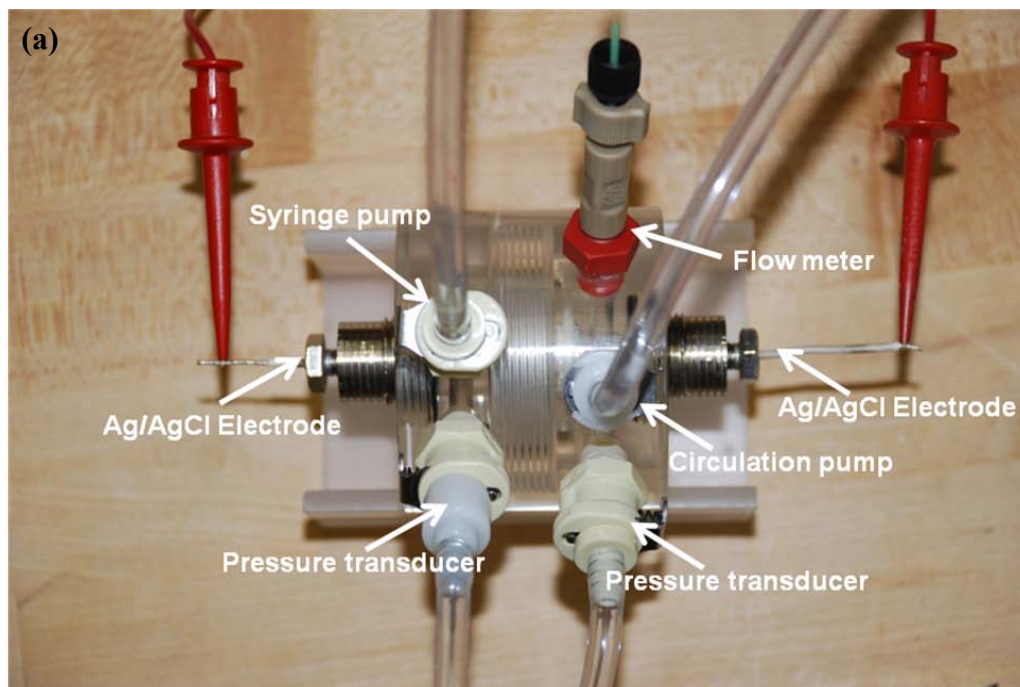
Figure 5-3: (a) photograph of custom-made perfusion chamber with connections to voltage measurement system, electrical current supply system, pressure applying system, and flow-rate monitoring system. (b) photograph of custom-made perfusion chamber center compartment.
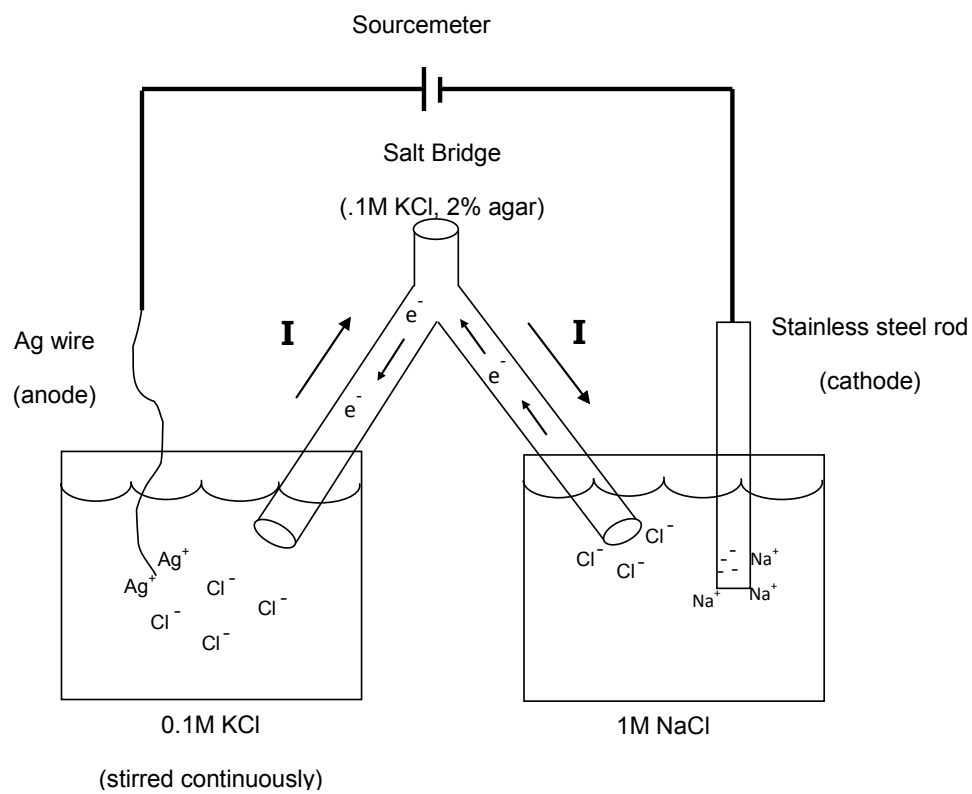
Figure 5-4: Schematic for the manufacture of Ag/AgCl electrodes.
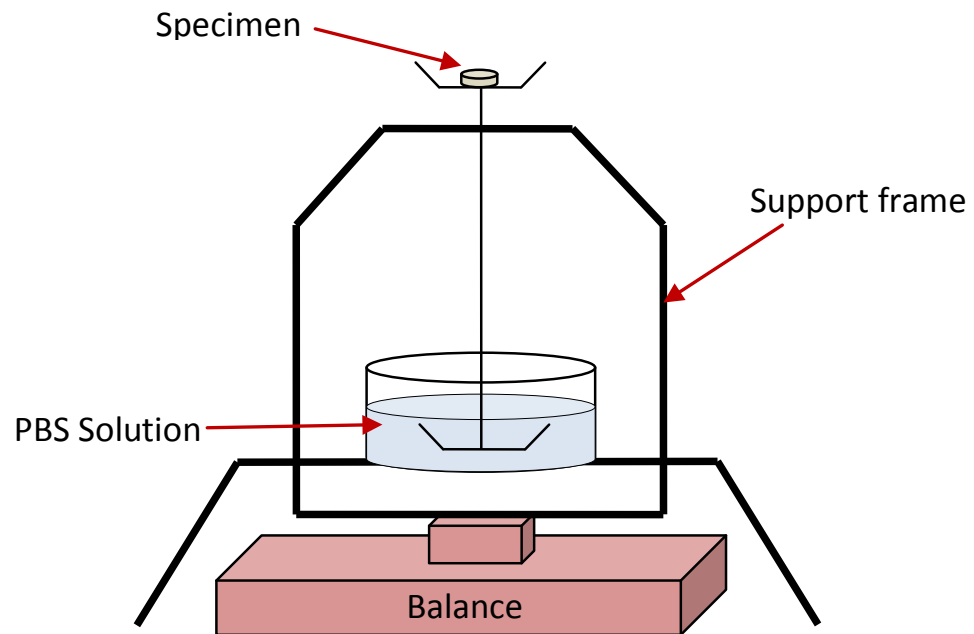
Figure 5-5: Schematic showing setup for analytical balance with density determination kit used for measuring tissue water content.

5.4 RESULTS

Results for hydraulic permeability, electrical conductivity and streaming potential of AC and AF measured using the newly developed apparatus are shown in Table 5.1. Using these measurements, the FCD and water volume fraction of specimens were calculated based on equations (5-1) and (5-4), and converted to the values corresponding to the state of zero-strain (i.e., reference state).

Using this new technique, the values of tissue water content (mean ± standard deviation) at reference state were 0.87 ± 0.04 (n=5) and 0.76 ± 0.02 (n=5) for AC and AF, respectively. The values of water content determined by lyophilization were 0.84 ± 0.01 (n=5) and 0.76 ± 0.02 (n=5) for AC and AF, respectively. A one-way analysis of variance (ANOVA) test was used to analyze the data. No statistical difference was found between the values determined by these two methods (Figure 5-6).

At reference state, the values of FCD determined using streaming potential method were 115.18 ± 37.32 mole/m^3 (n=5) and 76.96 ± 32.05 mole/m^3 (n=5) for AC and AF, respectively. The values of FCD determined by DMMB method were 138.18 ± 57.36 mole/m^3 (n=5) and 69.43 ± 18.62 mole/m^3 (n=5) for AC and AF, respectively. No statistical difference was found between the values determined by these two methods (Figure 5-7).

Table 5.1: Measured and Calculated Values for Material Properties of Cartilage and Annulus Fibrosus (AF) Samples

	Articular Cartilage	Annulus Fibrosus (AF)
χ (S/m)	1.05 ± 0.06	0.39 ± 0.05
k (m^4/Ns) $\times 10^{16}$	7.76 ± 0.77	1.18 ± 0.268
$\Delta\psi$ (mV)	0.92 ± 0.23	0.668 ± 0.242
Calculated c^F (mole/m^3)	115.18 ± 37.32	76.96 ± 32.05
Measured c^F (mole/m^3)	138.18 ± 57.36	69.43 ± 18.62
Calculated ϕ^w	0.87 ± 0.036	0.76 ± 0.028
Measured ϕ^w	0.84 ± 0.0049	0.76 ± 0.015
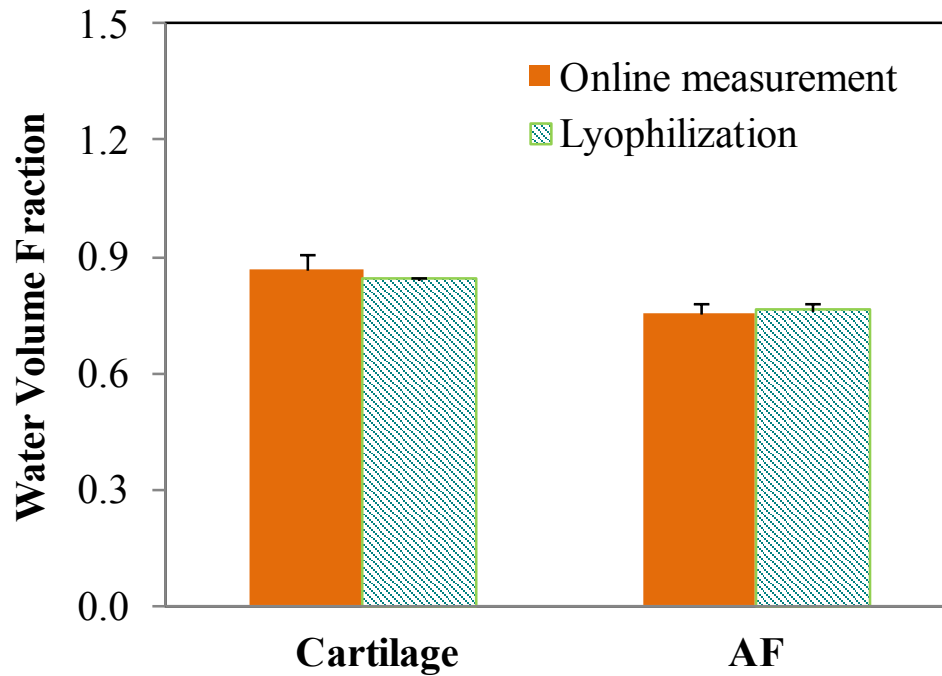
Figure 5-6: Comparison of water volume of cartilage and AF using two methods, (1) using the online-characterization method in the chamber to invasively calculate water volume, (2) lyophilizing the samples after experiments to directly measure the water volume.
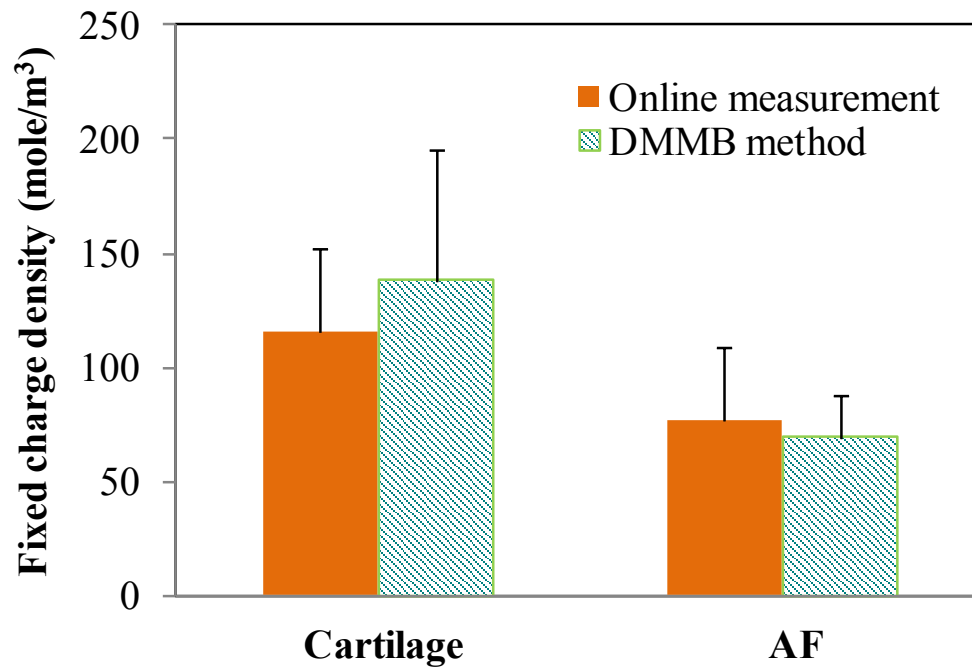
Figure 5-7: Comparison of calculated FCD and directly measured GAG of cartilage and AF. FCD was calculated from online-characterization in the chamber. GAG was measured directly from samples using DMMB method after experiments.

5.5 DISCUSSION

In this study, new bioreactor technology capable of online characterization of tissue water content, FCD, hydraulic permeability, electrical conductivity, and streaming potential was developed. The new technique for nondestructively monitoring water content and FCD of tissue in a bioreactor system was validated using the lyophilizaton method (for water content) and the DMMB method (for FCD). Articular cartilage and annulus fibrosus tissues were used to demonstrate the diverse application and accuracy of this technique for different types of cartilaginous tissues. The new technique is able to accurately determine the water content of tissues nondestructively (less than 3% disparity), and can be used to monitor the water content of tissue in the bioreactor in real time.

The experimental data demonstrated that the recently developed method could accurately determine the water volume fraction and FCD within cartilaginous tissues. The variation between direct water volume fraction measurement and online-characterization was negligible, presenting less than a 3% disparity. Additionally, the FCD measurements for both cartilage and AF tissues varied by less than 16.7%. These results are noteworthy and confirm that this is a viable method for non- destructively determining tissue properties.

The values of FCD for AC and AF tissues determined using this method (i.e., the streaming potential method) varied by less than 16.7% from those obtained by the conventional (destructive) DMMB method. One possible source for higher discrepancies in FCD measurements may be an error in measuring streaming potential, whereby the measured voltage is affected by the concentration polarization effect during the

permeation test.(Helfferich, 1962) This phenomenon stems from the accumulation of electrolytes on the high pressure side of the tissue, resulting in an ion concentration gradient across the sample that can adversely influence the measured streaming potential. While the streaming potential method for FCD is not new(Maroudas, 1968; Maroudas et al., 1969), the incorporation of this technique into a bioreactor system for online monitoring tissue biochemical properties is innovative.

The innovative method designed in this project offers many opportunities to develop applications for cartilaginous tissue engineering. The primary goal in this sector of tissue engineering is to repair or reproduce a functional cartilaginous tissue. Bioreactors are unique tools that allow us to create optimal conditions that model the *in vivo* environment of tissues and cells. Cells cultured in engineered constructs respond to their environment by altering rates and mechanisms by which important matrix molecules are synthesized and deposited (Wilson et al., 2002). During long-term culture, this cell activity can change the material properties of the construct to correctly model the target tissue. Conventionally, the progression of material remodeling is monitored invasively by removing constructs at various times during the culture period. By employing the recently developed method described here, bioreactors will have the capability to noninvasively online-characterize the material properties of engineered constructs in real time. Ultimately, the bioreactor will have the ability to precisely control different chemical and mechanical signals to provide the optimum culture conditions.

In summary, a new measurement method was developed. This method allows for the online characterization of material properties and biochemical signals in a tissue construct. By comparing calculated values of fixed charge density and water volume

fraction with those measured directly, the results have shown that this method can reliably determine important properties of cartilaginous tissues noninvasively. This study provides important insight for future development of bioreactor technology as well as successful tissue engineering strategies.

CHAPTER 6. TENSION-COMPRESSION NONLINEARITY BEHAVIOR IN ARTICULAR CARTILAGE

6.1 BACKGROUND

The mechanical function of cartilaginous tissues is to bear and transmit the load from one end of the tissue to the other. As previously mentioned in Chapter 2, the primary mechanical function of IVDs is to transmit loads arising from body weight and muscle activity through the spinal column (Urban and Roberts, 2003). For articular cartilage, the primary mechanical function is to transmit loads across diarthrodial joints while maintaining low friction and wear (Soltz and Ateshian, 2000). It is important to understand and be able to measure the mechanical properties of cartilaginous tissues in order to create functional cartilaginous substitutes.

Cartilaginous tissue is composed of many components. In general, cartilaginous tissue is seen as a biphasic material composed of an elastic solid matrix phase and an inviscid fluid phase (Mow et al., 1980; Armstrong et al., 1984; Cohen et al., 1998; Soltz and Ateshian, 2000; Huang et al., 2001). Many studies have investigated the mechanical behavior of cartilaginous tissues experimentally and theoretically. The mechanical response of hydrated cartilaginous tissue has been successfully described in confined compression creep and stress relaxation by the biphasic mixture theory of Mow et al. (Mow et al., 1980) and the electromechanical model of Frank and Grodzinsky (Frank and Grodzinsky, 1987b). These models can appropriately explain the time-dependent viscoelastic response of cartilage resulting primarily from the dissipative drag of interstitial fluid flowing through the porous solid matrix.

These early developed theories are the foundation for future models; however, they are somewhat less successful in curve-fitting the early time response in unconfined compression stress-relaxation between two impermeable plates (Soltz and Ateshian, 2000; Armstrong et al., 1984). This is due to the fact that the biphasic mixture theory and the electromechanical model have been employed most frequently under the assumption of a linear isotropic solid matrix undergoing infinitesimal deformation (Soltz and Ateshian, 2000). In reality, cartilaginous tissue is an anisotropic and inhomogeneous material. The cartilaginous tissues exhibit different mechanical properties in compression and tension, and respond differently to compression and tension (Kempson et al., 1968; Woo et al., 1979; Roth and Mow, 1980; Akizuki et al., 1987; Laible et al., 1994; Schinagl et al., 1997). This difference in response behavior has been referred to as tension-compression nonlinearity or bimodular response (Soulhat et al., 1999; Soltz and Ateshian, 2000). For that reason, Soltz and Ateshian integrated the Conewise Linear Elasticity (CLE) model with the biphasic mixture theory to describe the tension-compression nonlinearity behavior (Soltz and Ateshian, 2000; Curnier et al., 1995). Huang et al. combined the quasilinear viscoelasticity (QLV) with biphasic-CLE model to further take into account the intrinsic viscoelasticity of solid matrix (Huang et al., 2001). Both biphasic-CLE and biphasic-CLE-QLV models can successfully describe the unconfined response of cartilaginous tissue properties.

In this study, hydraulic permeability was obtained from direct measurement in the previous chapter and the biphasic-CLE-QLV model was used to investigate the mechanical properties of cartilaginous tissue (tensile aggregate modulus, compressive

aggregate modulus, and compressive Young's modulus) under unconfined stress-relaxation compression.

6.2 THEORETICAL BACKGROUND

Cartilaginous tissue is modeled as a binary mixture of an intrinsically incompressible solid matrix and an interstitial fluid in the biphasic mixture theory of Mow et al. (Mow et al., 1980). The relationship between the total stress tensor σ inside the tissue, the interstitial fluid pressure p and the viscoelastic stress tensor σ^{ve} resulting from deformation of the solid matrix can be expressed as:

$$\sigma = -pI + \sigma^{ve},$$
(6-1)

where I is the identity tensor. The momentum equation of the mixture, under quasi-static conditions and the absence of body forces is given by:

$$\nabla \cdot \sigma = -\nabla p + \nabla \cdot \sigma^{ve} = 0,$$
(6-2)

where $\nabla \cdot$ denotes the divergence operator, and ∇ is the gradient operator. The continuity equation for the mixture is given by

$$\nabla \cdot \left(v^s + w \right) = 0,$$
(6-3)

where $w = \phi^f(v^f - v^s)$ is the flux of fluid relative to the solid, ϕ^f is the fluid volume fraction (tissue porosity) and v^f and v^s are the fluid and solid phase velocities, respectively.

In QLV theory, the viscoelastic stress tensor σ^{ve} can be related to the stress tensor under equilibrium conditions, σ^e, through:

$$\sigma^{ve}(t) = g(t)\sigma^e[E(0)] + \int_0^t g(t-\tau)\frac{\partial\sigma^e}{\partial\tau}[E(\tau)]d\tau, \tag{6-4}$$

where the E is the infinitesimal strain tensor, which is related to the solid displacement u through:

$$E = \frac{1}{2}\left(\nabla u + \nabla u^T\right), \tag{6-5}$$

and the displacement to the solid velocity is:

$$v^s = \frac{D^s u}{Dt}, \tag{6-6}$$

The reduced relaxation function, $g(t)$, is given by (Huang et al., 2001):

$$g(t) = 1 + c\left[E_i\left(\frac{t}{\tau_2}\right) - E_i\left(\frac{t}{\tau_1}\right)\right], \tag{6-7}$$

where $E_i(\cdot)$ represents the exponential integral function, and c, τ_1, τ_2 are material properties of the QLV theory. Physically, $\left[\frac{1}{\tau_2}, \frac{1}{\tau_1}\right]$ represents the frequency range over which most of the intrinsic viscoelastic energy dissipation occurs under dynamic loading, whereas $1 + c\ln\frac{\tau_2}{\tau_1}$ is the ratio of instantaneous to equilibrium moduli resulting from the intrinsic viscoelasticity alone.

The tension-compression nonlinearity response of solid matrix can be described by Conewise Linear Elasticity model of Curnier et al (Curnier et al., 1995; Soltz and Ateshian, 2000; Huang et al., 2001):

$$\sigma^e(E) = \sum_{a=1}^{3} \left\{ \lambda_1 [A_a : E] tr(A_a E) A_a + \sum_{\substack{b=1 \\ b \neq a}}^{3} \lambda_2 tr(A_a E) A_b \right\} + 2\mu E,$$

(6-8)

where $tr(\cdot)$ is the trace operator that yields the first invariant of its tensorial argument, and

$A_a : E = tr\left(A_a^T E\right)$. A is a texture tensor corresponding to each of the three preferred material directions defined by the unit vector a_a ($a_a \cdot a_a = 1$, no sum over a, $\cdot$ denoting the dot product), with, $A_a = a_a \otimes a_a$ ($\otimes$ denoting the dyadic product of vectors, no sum over a). For cubic material symmetry, $a_a \cdot a_b = 0$ when $b \neq a$, and the three directions are generally taken to be: a_1 parallel to the split line direction, a_2 perpendicular to the split line direction, and a_3 normal to the articular cartilage surface. The term $A_a : E$ represents the component of normal strain along the preferred direction a_a. Tension-compression nonlinearity is embodied in the fact that

$$\lambda_1[A_a : E] = \begin{cases} \lambda_{-1,} A_a : E < 0 \\ \lambda_{-1,} A_a : E > 0 \end{cases},$$

(6-9)

This signifies that the material property λ_1 differ whether the normal strain component along the direction a_a is compressive or tensile. The physical meaning of these elastic constants is as follows: $H_{-A} = \lambda_{-1} + 2\mu$ is the equilibrium compression modulus of the tissue, $H_{+A} = \lambda_{+1} + 2\mu$ is the equivalent modulus in tension, and λ_2 is the "off-diagonal" modulus, which could be determined from the equilibrium ratio of radial stress to axial strain in confined compression. This model can be reduced to the isotropic biphasic

poroviscoelastic model of Mak (Mak, 1986) by letting $\lambda_{-1} = \lambda_{+1} = \lambda_2 \equiv \lambda_1$ (and noting that $A_1 + A_2 + A_3 = I$).

The reduction of the general biphasic equations to the unconfined compression of biphasic-CLE-QLV model for the radial displacement is given by (Huang et al., 2001):

$$\frac{\partial^2 \overline{u_r}}{\partial r^2} + \frac{1}{r}\frac{\partial \overline{u_r}}{\partial r} - \frac{\overline{u_r}}{r^2} - f^{\pm}\overline{u_r} = \frac{rf^{\pm}}{2}\overline{\varepsilon}(s),$$

(6-10)

whereas the boundary conditions reduce to

$$\overline{u_r}\big|_{r=0} = 0, \qquad H_{\mp A}\frac{\partial \overline{u_r}}{\partial r} + \lambda_2\left(\frac{\overline{u_r}}{r} + \overline{\varepsilon}(s)\right)\bigg|_{r=r_0} = 0,$$

(6-11)

The solution then reduces to

$$\overline{u_r^{\pm}}(r,s) = \frac{r_0}{2}\left[\frac{\left(1 - \frac{\lambda_2}{H_{\mp A}}\right)I_1\left(\sqrt{f^{\pm}}\,\frac{r}{r_0}\right)}{\sqrt{f^{\pm}}I_0\left(\sqrt{f^{\pm}}\right) - \left(1 - \frac{\lambda_2}{H_{\mp A}}\right)I_1\left(\sqrt{f^{\pm}}\right)} - \frac{r}{r_0}\right]\overline{\varepsilon^{\pm}}(s),$$

(6-12)

$$\frac{\overline{F^{\pm}}(s)}{\pi r_0^2} = H_{\mp A}\left(1 + c\ln\frac{1 + \tau_2 s}{1 + \tau_1 s}\right)\left\{\frac{\left(\frac{2H_{\pm} - 3\lambda_2 + H_{\mp A}}{2H_{\mp A}}\right)\sqrt{f^{\pm}}I_0\left(\sqrt{f^{\pm}}\right) + \left(1 - \frac{\lambda_2}{H_{\mp A}}\right)\left(\frac{2\lambda_2 - H_{\pm A} - H_{\mp A}}{H_{\mp A}}\right)I_1\left(\sqrt{f^{\pm}}\right)}{\sqrt{f^{\pm}}I_0\left(\sqrt{f^{\pm}}\right) - \left(1 - \frac{\lambda_2}{H_{\mp A}}\right)I_1\left(\sqrt{f^{\pm}}\right)}\right\}\overline{\varepsilon^{\pm}}(s),$$

(6-13)

where

$$f^{\pm} = \frac{r_0^2 s}{H_{\mp A}k\left(1 + c\ln\frac{1 + \tau_2 s}{1 + \tau_1 s}\right)},$$

(6-14)

In these equations, r is the radial coordinate, u_r refers to the radial displacement, ε is the axial strain, F is the total axial force across the specimen. I_0 ($\cdot$) and I_1 ($\cdot$) are modified Bessel functions of the first kind, of order 0 and 1, respectively. Overbars indicate Laplace transform variable. Superscripted $\pm$ on these parameters refer to the solution for tension (+) or compression (-). Note that the solution does not depend on the axial dimension (thickness or length) of the cylindrical specimen. A slow strain rate was used in this study. For slow strain rate, the intrinsic viscoelasticity of solid matrix is negligible. Therefore, the biphasic CLE-QLV model is reduced to Biphasic CLE model by assuming c =0 in the equation (6-13).

The equilibrium compressive Young's modulus (E_{-Y}) can be obtained from:

$$E_{-Y} = H_{-A} - \frac{2\lambda_2^2}{H_{+A} + \lambda_2}$$

(6-15)

6.3 MATERIALS AND METHODS

To investigate the tension-compression nonlinearity behavior of bovine articular cartilage, a custom-made loading apparatus was designed and constructed (Figure 6-1). This apparatus consisted of two parts: the main frame and the compressive chamber. The main frame consisted of a servo motor (SM23165D, Animatics Motor, Santa Clara, CA), a digital encoder (tonic encoder, Renishaw, New Mills, UK), and a linear actuator (KR2602A, THK, Tokyo, Japan).
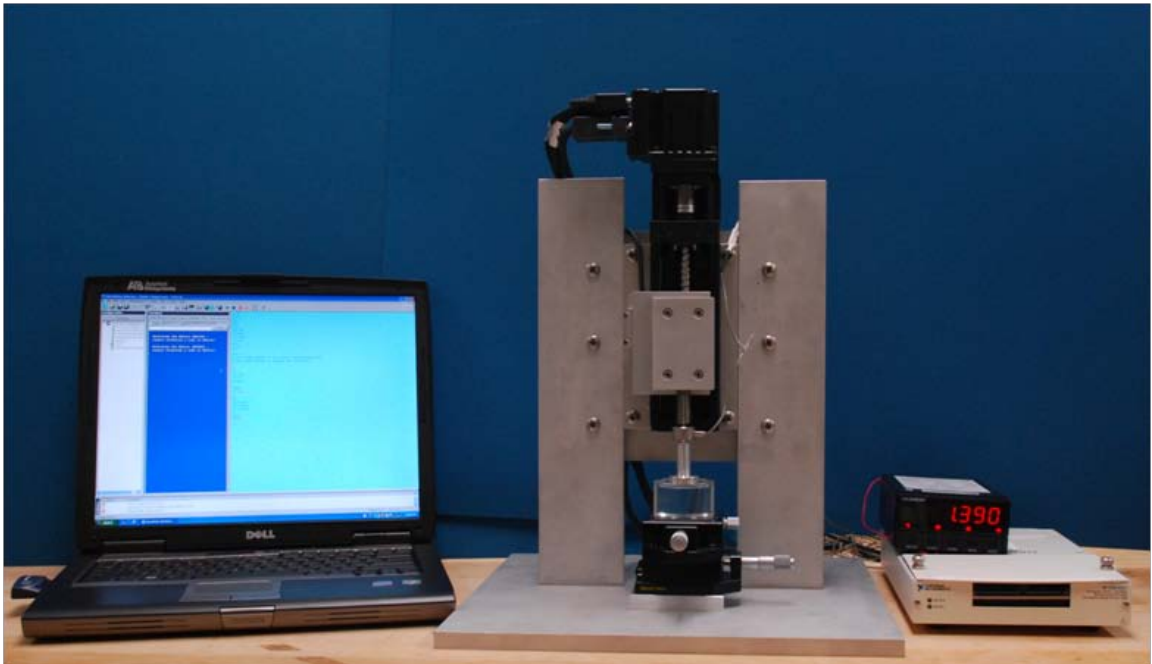
Figure 6-1: Photograph of loading device. The loading device connected with a laptop through a data acquisition board.

Conventionally, stepping motors are chosen to build a similar loading apparatus. A stepping motor is an electromechanical-driven rotary device (Figure 6-2). The rotating shaft in a stepping motor moves in discrete mechanical movements by converting electrical pulses from a switched DC supply. As its name implies, the stepping motor moves in discrete "steps" or "increments." Each shaft revolution can be expressed in terms of a number of discrete identical steps or increments. However, the application in current study required movements at the micron level and using a stepping motor could result in inaccurate movements and/or low repeatability.

A stepping motor operates in an open loop control system, which means there is no feedback information on the position of the shaft. The position of the shaft simply relies on tracking the input step pulses. In other words, one cannot know the exact position of a step motor. On the other hand, a servo motor produces continuously movement where speed or rotation can be easily controlled (Figure 6-3).

The most significant advantage of the servo motor is that it operates in a closed loop control system. A servo motor consists of a DC/AC motor, an encoder, and a controller. When the DC/AC motor rotates, the encoder detects the input signal and compares it with the feedback signal from the DC/AC motor output. If the output signal does not match with the expected input signal, the encoder will send the information to the controller and the controller will correct the DC/AC motor movement until the output signal matches with input signal. A stepping motor would not be able to detect or fix this movement error. Therefore, a servo motor was chosen to build the loading device.
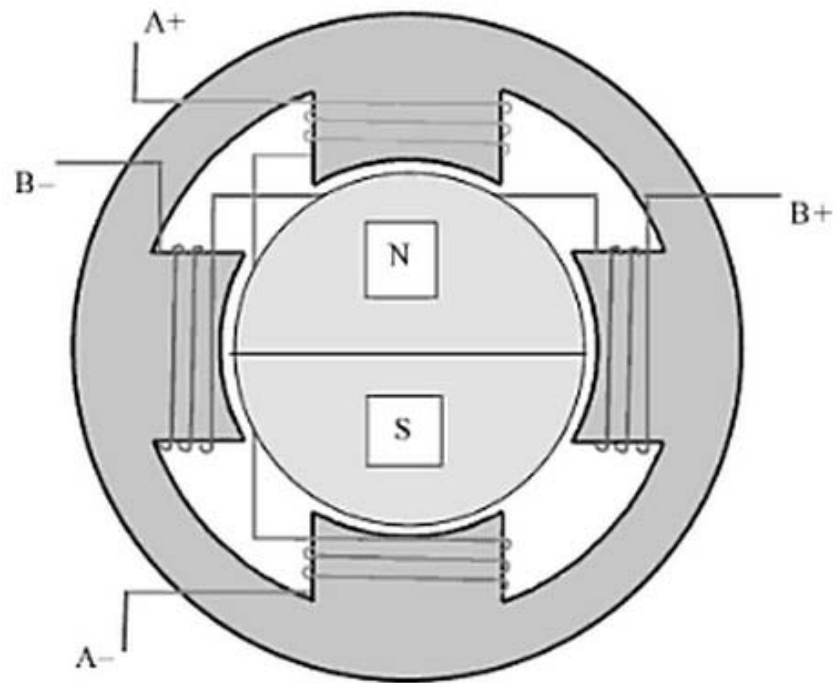
Figure 6-2: Schematic of a permanent-magnet stepping motor (Paul Acarnely, 2002).
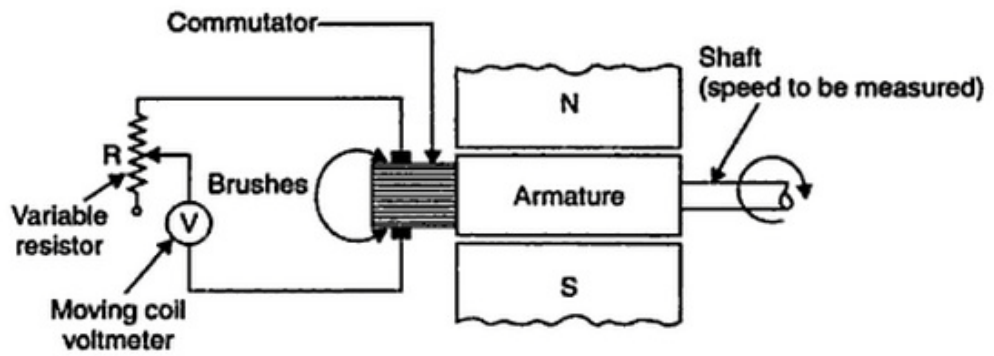
Figure 6-3: Schematic of a DC servo motor (R.K.Rajput, 2005).

Before the experiment, the Animatics servo motor had to be "tuned" to the optimal conditions. The purpose of tuning is to adjust the features of the servo motor so that it follows the input signal as closely as possible. Proportional-integral-derivative (PID) control was applied to tune the Animatics servo motor. PID control is the most widely used control for tuning servo motors today. It is estimated that over 90% of control loops employ PID control (Knospe, 2006). The proportional gain adjusts the output proportional to the current control error. The integral gain is proportional to the integral of both the magnitude of the error and the duration of the error. The derivative gain predicts future values of the control error (Antonio Visioli, 2006). Manual PID tuning was applied to the Animatics servo motor. The typical manual PID control system tuning is represented in Figure 6-4. The controller receives the input signal, and the signal is manipulated with PID control. This produces an output signal that is compared with the input signal. If there is no error between output and input signals, the motor will keep moving. However, if the output and input signals do not match, the controller will adjust the motor until the output and input signals match .

Compression chamber. A custom-made compression chamber was made of acrylic. The compression chamber was designed with a hole in the center to hold the tissue and PBS. The center hole was 1.26" (~32mm) in diameter and 0.15" (~3.8mm) deep. The compression chamber was mounted in a two-way linear translation stage (Melles Griot, Albuquerque, NM). The tissue sample can easily be placed in the center of the compression axis by manipulating the two-way linear translation stage. This compression chamber can be modified to a confined chamber to perform confined compression experiments in the future.

Experiment protocol. Knee articular cartilage from a 6-month-old cow was used in this study. Samples of cartilage with bone were first punched out using corneal trephines (Biomedical Research Instruments, Inc., Silver Spring, MD). Sledge microtome (Model SM2400, Leica Instruments, Nussloch, Germany) with freezing stage (Model BFS-30, Physitemp Instruments, Inc., Clifton, NJ) were then used to remove bone and cartilage deep zone from samples. After measuring the cartilage samples with the custom-designed current sensing micrometer, the samples were microtomed to the desired thickness (see section 2.3). Five cylindrical cartilage samples with a diameter of 6 mm and a thickness of approximately 1 mm were prepared. Samples were stored at -20°C until the experiment was performed.

The Animatics servo motor was controlled by the SmartMotor Interface software (Animatics Motor, Santa Clara, CA). Before placing the cartilage sample inside of the compression chamber, the bottom of the chamber was set as the zero reference point. The chamber was filled with PBS after the cartilage sample was placed into the compression chamber. A flat impermeable platen made of aluminum alloy was attached to the linear actuator. The impermeable platen was used to touch off the cartilage sample in order to acquire the thickness of the cartilage sample. The thickness acquired in the chamber was used as the height to calculate the compressive strain later. Before the test was performed, each sample received a preload of 50 kPa (2.5N). The preload was maintained until the sample reached equilibrium (fluid pressure reducing to zero) which was set as the zero point (Soltz and Ateshian, 2000; Huang et al., 2003). The criterion for establishing equilibrium was that the change in load did not fall below the resolution of the load cell (0.067N) over a period of at least 300 seconds (Huang et al., 2003). Following the

establishment of equilibrium, the unconfined stress-relaxation test was performed. The top impermeable flat platen was lowered with a constant velocity of 0.25 μm/s until 5 percent tissue strain was reached. The displacement was then held constant until equilibrium was established and the test was concluded (Soltz and Ateshian, 2000). The unconfined compression reaction force was recorded with a custom LabView program (version 8.2, National Instruments Corp., Austin, TX) as a function of time. The experimental data was curve-fit with equation 6-13 using MATLAB (R2010b, MathWorks, Natick, MA) to obtain the material properties of samples. The experiment was conducted at room temperature. A least squares curve-fitting algorithm was used to find the best-fit material parameters by matching the experimentally measured force with the corresponding theoretical response.

6.4 RESULTS

The material properties were obtained by curve fitting the experimental results and have been summarized in Table 6.1. The mean ± standard deviation values of the material properties of bovine knee articular cartilage were found to be: $H_{+A} = 13.2 \pm 3.27$ MPa, $H_{-A} = 0.93 \pm 0.67$ MPa, $\lambda_2 = 0.76 \pm 0.36$ MPa, $E_{-Y} = 0.83 \pm 0.62$ MPa. A sample of raw experimental data and its corresponding curve-fitting are also plotted in Figure 6-5. The R-squared value for the curve-fitting of the unconfined compression load response is 0.96 ± 0.02.
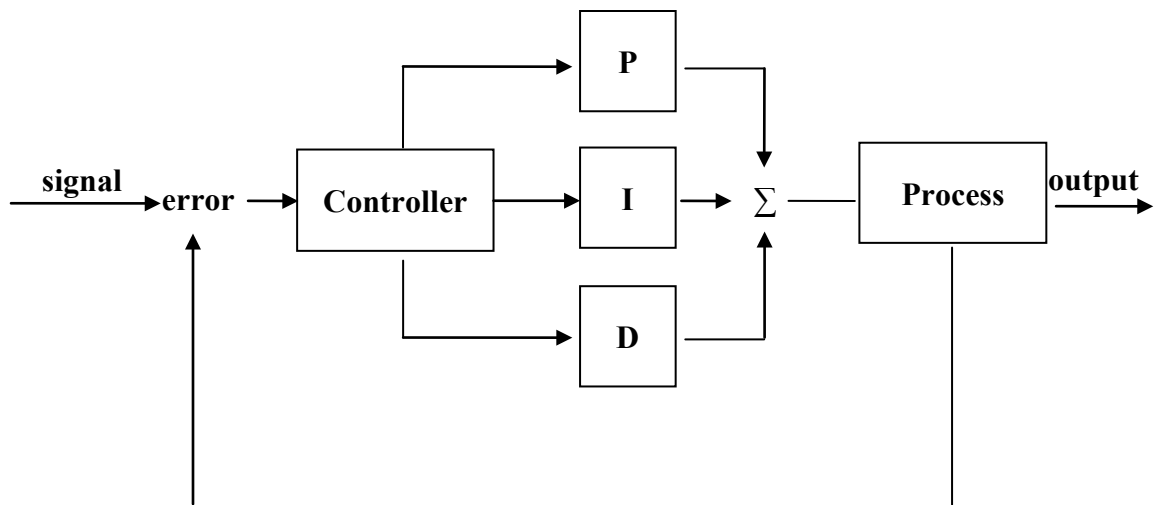
Figure 6-4: Block diagram of a typical PID control loop.

Table 6.1: Results for mean ± standard deviation values of the material properties of bovine knee articular cartilage.

Samples	H_{+A} (MPa)	H_{-A} (MPa)	λ_2 (MPa)	E_{-Y} (MPa)
1	16	1.43	1.2	1.26
2	17	1.78	1.1	1.65
3	10	0.82	0.56	0.75
4	10	0.3	0.56	0.23
5	13	0.3	0.39	0.28
Mean ± STDEV	13.2 ± 3.27	0.93 ± 0.67	0.83 ± 0.62	0.83 ± 0.62
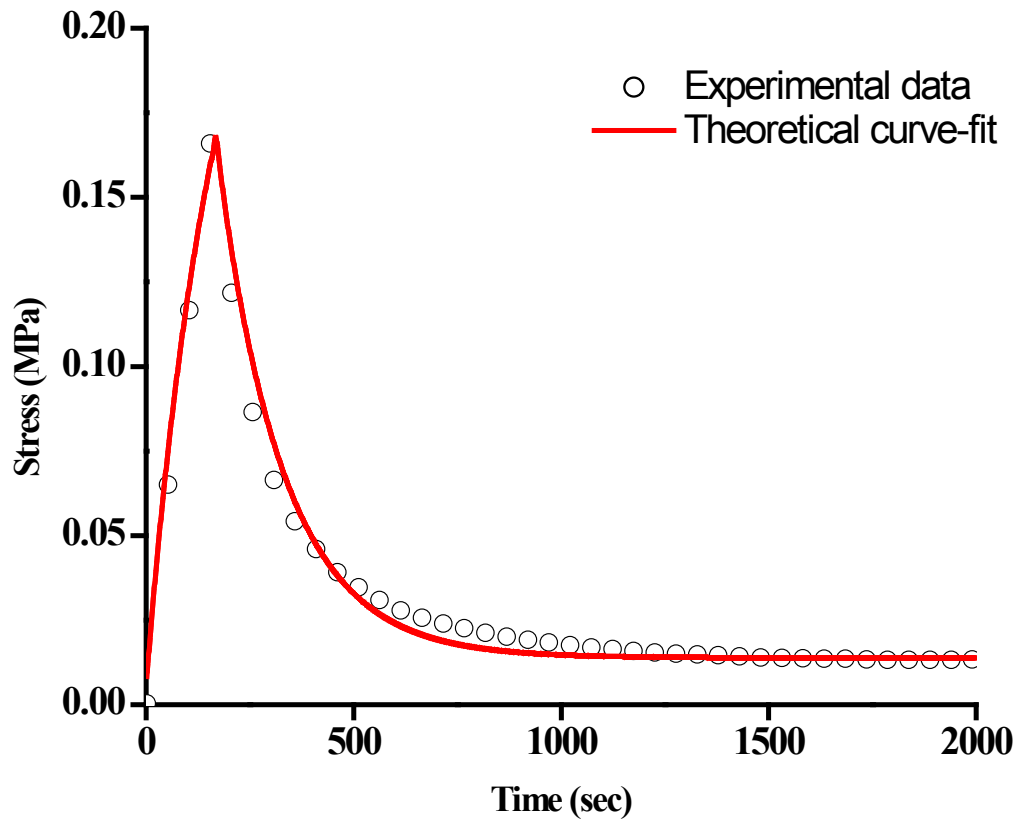
Figure 6-5: Unconfined compression stress-relaxation response of the biphasic-CLE-QLV model, to a ramp strain (0.25 μm/s) of magnitude $\varepsilon_0 = 0.05$ (5 percent).

6.5 DISCUSSION

The primary mechanical function of cartilaginous tissues is loading support. Under conditions of infinitesimal strain, the biphasic mixture theory and the electromechanical model can successfully determine the time-dependent viscoelastic response of cartilage under assumption of linear biphasic material. The cartilaginous tissue is a biphasic mixture with anisotropic and inhomogeneous tissue properties in reality. They exhibit different responses to tension and compression in different directions.

In this study, a custom loading apparatus was developed to investigate the mechanical properties of bovine knee articular cartilage. The biphasic-CLE-QLV model was used to predict the time-dependent stress-relaxation response in the cartilage samples during the unconfined experiment. The biphasic-CLE model and the biphasic-CLE-QLV model can accurately predict the unconfined compression response. Under the fast strain rate (10 percent compression in 3 seconds), there is a large magnitude unconfined compression transient response because of the intrinsic viscoelasticity of the solid matrix of articular cartilage (Huang et al., 2001). The biphasic-CLE-QLV model can accurately calculate this transient response. However, the effect on intrinsic viscoelasticity of the solid matrix is negligible under the slow strain rate. As a result, the intrinsic viscoelasticity can be neglected (by assuming the $c = 0$). The biphasic-CLE-QLV model will then reduce to the biphasic-CLE model.

In previous studies (Soltz and Ateshian, 2000; Huang et al., 2001), in order to determine the values of hydraulic permeability and other material properties (H_{+A}, H_{-A}, λ_2 and E_{-Y}) of cartilage, confined and unconfined compression testing configurations were

performed. In the current study, the values of hydraulic permeability were determined through the direct measurement previously discussed in Chapter 5. This, combined with the results obtained from the unconfined compression test, allowed for the determination of the compression and tension modulus. This is the first study to combine 1-D permeation direct measurement and unconfined compression to determine the hydraulic permeability and mechanical properties of cartilaginous tissue.

A typical experimental dataset and its corresponding theoretical curve-fit are plotted in Figure 6-5. The results suggest that the biphasic-CLE-QLV model can estimate the response of cartilage successfully. The model predicts the stress-relaxation response with an R-squared of 0.96 ± 0.02 in the unconfined compression test, providing further support toward the validation of this model.

The values of mechanical properties have been summarized in Table 6-1. The values from each cartilage sample were obtained by curve-fitting the experimental results with equation (6-13). The results from the current study are also compared with previous studies found in the literature. The tensile aggregate modulus (H_{+A}) found in the current study was 13.2 MPa. Previous studies show that the tensile aggregate modulus (H_{+A}) is around 13.2 MPa in bovine humeral head articular cartilage (Soltz and Ateshian, 2000; Huang et al., 2001). The tensile aggregate modulus in this study was found comparable with these studies. A previous study used bovine knee articular cartilage to determine the equilibrium confined compressive aggregate modulus and found that the compressive aggregate modulus from the middle layer of bovine knee articular cartilage was 1.14 MPa (Schinagl et al., 1997). Mow et al. (1989) also found that the compressive aggregate modulus was 0.9 MPa in young bovine femoral condylar cartilage. The result from the

current study (H_A = 0.93 MPa) shows a good agreement with studies in the literature. One study found that compressive Young's modulus was 0.6 MPa (Soltz and Ateshian, 2000), compared to 0.83 MPa in the current study. The difference may be due to the use of cartilage from different locations of the joint. Overall, the mechanical properties determined in the current study were found to be similar to studies in the literature.

In summary, a loading apparatus was developed to conduct the unconfined compression stress relaxation experiment. The hydraulic permeability was determined from the method developed in Chapter 5. The mechanical properties are comparable to previous studies. The current study demonstrates that the stress-relaxation response can be successfully predicted by the biphasic-CLE-QLV model.

CHAPTER 7. CONCLUSION AND RECOMMENDATIONS

Low back pain is one of the major health concerns in the US. Unfortunately, the cause of low back pain is still not fully understood. However, current studies show that low back pain is strongly associated with degeneration of intervertebral discs. There are many different types of treatments for disc degeneration currently. But none of them are targeting the source --- degeneration of intervertebral discs.

At present, researchers are trying to apply tissue engineering methods to improve or even restore the function of degenerated discs. The ultimate goal will be utilizing these tissue engineering approaches to create a biological substitute for total disc replacement in the near future. Before we can create biological substitutes, we need to understand the properties and functions of the native tissue. Researchers are currently using bioreactors to develop different types of biological substitutes. A drawback of the current approaches to determine the status within these substitutes is that they are invasive. This means we have to destroy substitutes in the bioreactor in order to know their status. Therefore, in this dissertation, methods were developed to characterize tissues properties noninvasively and in real-time.

7.1 OXYGEN TRANSPORT PROPERTY

Intervertebral disc cells only make up around 1% of disc volume, but they play a crucial role in the disc. They produce PG, collagen and other agents to breakdown the extracellular matrix. Therefore, they are responsible for maintaining the disc composition and turnover. It is important to understand how they acquire nutrients such as oxygen and glucose. In chapter 3, a new method was developed to determine the oxygen diffusivity and found that the oxygen diffusivity values in human AF at 0% compression were found

to be: 1.22, 1.33 and 1.23×10^{-5} cm^2/s in the axial, circumferential, and radial directions, respectively To our knowledge, this is the first study to investigate the strain-dependent behavior of oxygen diffusivity in human AF tissue. This study demonstrates that the mechanical load plays an important role in the transport of oxygen. The knowledge of the response of transport properties to disc degeneration is important for understanding the etiology of disc degeneration, because the failure of the nutrient supply to the disc cells is thought to be one of the primary causes of disc degeneration. Moreover, the results from this study provide information needed to develop future theories and numerical models for quantitatively investigating the mechanisms and pathways of nutritional transport in the IVD subjected to mechanical loads.

7.2 OXYGEN CONSUMPTION RATE

The oxygen concentration and the rate of cell metabolism have a great influence on the gradient of oxygen throughout the disc. In Chapter 4, results showed that the rate of oxygen consumption of NP and AF cells remained more or less constant at high oxygen tension but fell steeply as oxygen tension decreased to 5% or below. The rate of oxygen consumption of NP cells was not regulated by the glucose concentration. The outer AF cells cultured in the high glucose medium (25 mM glucose) exhibited a lower oxygen consumption rate whereas there were no significant differences in oxygen consumption rate among the outer AF cells cultured at physiological levels of glucose (i.e., 1 mM, 2.5 mM, 5 mM).

This is the first investigation of the rate of oxygen consumption of AF cells under different levels of glucose concentration including physiological levels of glucose. A new method was used to determine the rate of oxygen consumption. The analytical solution

was derived from Michaelis-Menten equation. This model can accurately determine the oxygen consumption, and there were very good agreements found between the experimental data and theoretical curve fitting for AF ($R^2=0.994\pm0.005$) and NP ($R^2=0.997\pm0.003$) cells.

The experimental protocols and new method for determining the rate of oxygen consumption established for porcine AF and NP cells in current study could be applied to human IVD cells. Samples tested in this study were made of agarose; thus, samples made of alginate could also be investigated. Different passages could also exhibit different rates of oxygen consumption; therefore, this should also be investigated in the future.

7.3 MECHANO-ELECTROCHEMICAL PROPERTY

One of the tissue engineering approaches is to use bioreactors for developing the biological substitutes to replace injured or degenerated tissues. Knowledge of the mechano-electrochemical signals around the cells and solute transport within a tissue is crucial to understanding cell biology, tissue growth and remodeling in vivo or in vitro (Mow et al., 1999). Therefore, it is important to measure the mechano-electrochemical properties within the substitutes during their growth in the bioreactors. While monitoring the current status of the substitute, we can control the chemical, electrical and mechanical environment. As a result, they can be cultured in the most optimal conditions.

The existing methods to investigate the mechano-electrochemical properties of tissues or engineered substitutes are invasive. As discussed in Chapter 5, a new measurement method was developed to determine the mechano-electrochemical properties noninvasively and in real-time. The recently developed system can measure the hydraulic permeability, electrical conductivity, streaming potential, and ion

diffusivity within the cartilaginous tissues. Different types of tissue (bovine AF and knee articular cartilage) and conditions (different compressive strains and different size of samples) were used to verify recently developed system. The results show that calculated FCD and water volume of AF and cartilage tissues within current systems are comparable to direct measurement methods. A percent error of 16.7% and 3% for FCD and water volume, respectively, suggests that this newly developed system is capable of characterizing the tissue properties.

If we can combine the current system with feed-back control to build a bioreactor system in the future, we can grow engineered tissue in vitro for implantation in vivo. The results from this study can also help to develop a numerical method for predicting the mechano-electrochemical signals within the tissue in the bioreactor.

7.4 MECHANICAL PROPERTY

The primary mechanical function of cartilaginous tissues is to support and transmit load between cartilaginous tissue and adjacent joints. Cartilaginous tissue is a biphasic mixture with anisotropic and inhomogeneous material properties. It is important to assess the tension-compression nonlinearity response of cartilaginous tissue because the tissue experiences various degrees of tension and compression.

In Chapter 6, a custom loading apparatus was built to perform unconfined stress-relaxation compression tests in bovine knee articular cartilage. Using the biphasic CLE-QLV model combined with the hydraulic permeability determined in Chapter 4, the tensile aggregate modulus (H_{+A}), the compressive aggregate modulus (H_{-A}), the compressive young's modulus (E_{-Y}) and λ_2 in the middle layer of bovine knee articular cartilage were obtained from curve fitting the stress-relaxation response under the

infinitesimal deformation condition (H_{+A} = 13.6 ± 3.36 MPa, H_{-A} = 1.03 ± 0.59 MPa, λ_2 = 1.16 ± 0.05 MPa, E_{-Y} = 0.84 ± 0.61 MPa) The model shows that it can predict the stress-relaxation response successfully (R^2 = 0.96 ± 0.01).

The long term goals for this research are to elucidate the etiology of human disc degeneration and apply an engineering approach to develop the biological substitutes to replace degenerated discs. In this dissertation, measurement methods were developed to determine the transport, mechano-electrochemical and mechanical properties within the tissue. These innovative methods will not only provide new tools for investigating the response of tissues to their environment, but also provide information for developing the theoretical models for quantitatively investigating the mechanisms and pathways during the growth of engineering substitutes.

Reference List

Acaroglu, E. R., Iatridis, J. C., Setton, L. A., Foster, R. J., Mow, V. C., Weidenbaum, M., (1995). Degeneration and aging affect the tensile behavior of human lumbar anulus fibrosus. Spine 20, 2690-2701.

Adams, M. A., Hutton, W. C., (1983). The effect of posture on the fluid content of lumbar intervertebral discs. Spine 8, 665-671.

Adams, M. A., Hutton, W. C., (1986). The effect of posture on diffusion into lumbar intervertebral discs. J Anat. 147, 121-134.

Adams, M. A., McNally, D. S., Dolan, P., (1996). 'Stress' distributions inside intervertebral discs. The effects of age and degeneration. J Bone Joint Surg Br. 78, 965-972.

Aguiar, D. J., Johnson, S. L., Oegema, T. R., (1999). Notochordal cells interact with nucleus pulposus cells: regulation of proteoglycan synthesis. Exp.Cell Res. 246, 129-137.

Akizuki, S., Mow, V. C., Muller, F., Pita, J. C., Howell, D. S., (1987). Tensile properties of human knee joint cartilage. II. Correlations between weight bearing and tissue pathology and the kinetics of swelling. J Orthop Res 5, 173-186.

Antonio Visioli, (2006). Practical PID Control (Advances in Industrial Control). Springer.

Antoniou, J., Steffen, T., Nelson, F., Winterbottom, N., Hollander, A. P., Poole, R. A., Aebi, M., Alini, M., (1996). The human lumbar intervertebral disc: evidence for changes in the biosynthesis and denaturation of the extracellular matrix with growth, maturation, ageing, and degeneration. J Clin Invest 98, 996-1003.

Armstrong, C. G., Lai, W. M., Mow, V. C., (1984). An analysis of the unconfined compression of articular cartilage. J Biomech Eng 106, 165-173.

Armstrong, C. G., Mow, V. C., (1982a). Biomechanics of normal and osteoarthritic articular cartilage. In: Wilson, P. D., Straub, L. R. (Eds.), Clinical Trends in Orthopaedics. Thiem-Stratton Inc., pp. 189-197.

Armstrong, C. G., Mow, V. C., (1982b). Variations in the intrinsic mechanical properties of human articular cartilage with age, degeneration, and water content. J Bone Joint Surg 64A, 88-94.

Arosarena, O., (2005). Tissue engineering. Curr.Opin.Otolaryngol.Head Neck Surg. 13, 233-241.

Bancroft, G. N., Sikavitsas, V. I., Mikos, A. G., (2003). Design of a flow perfusion bioreactor system for bone tissue-engineering applications. Tissue Eng 9, 549-554.

Bancroft, G. N., Sikavitsas, V. I., van den, D. J., Sheffield, T. L., Ambrose, C. G., Jansen, J. A., Mikos, A. G., (2002). Fluid flow increases mineralized matrix deposition in 3D perfusion culture of marrow stromal osteoblasts in a dose-dependent manner. Proc.Natl.Acad.Sci.U.S.A 99, 12600-12605.

Bayliss, M. T., Johnstone, B., (1992). Biochemistry of the intervertebral disc. In: JIV Malcom (Ed.), The Lumbar Spine and Back Pain. Churchill Livingstone, New York, pp. 111-132.

Beckstein, J. C., Sen, S., Schaer, T. P., Vresilovic, E. J., Elliott, D. M., (2008). Comparison of animal discs used in disc research to human lumbar disc: axial compression mechanics and glycosaminoglycan content. Spine (Phila Pa 1976.) 33, E166-E173.

Bibby, S. R., Fairbank, J. C., Urban, M. R., Urban, J. P., (2002). Cell viability in scoliotic discs in relation to disc deformity and nutrient levels. Spine 27, 2220-2228.

Bibby, S. R., Jones, D. A., Lee, R. B., Yu, J., Urban, J. P. G., (2001). The pathophysiology of the intervertebral disc. Joint Bone Spine 68, 537-542.

Bibby, S. R. S., Jones, D. A., Ripley, R. M., Urban, J. P., (2005). Metabolism of the intervertebral disc: effects of low levels of oxygen, glucose, and pH on rates of energy metabolism of bovine nucleus pulposus cells. Spine 30, 487-496.

Bogduk, N., (2004). Management of chronic low back pain. Med.J.Aust. 180, 79-83.

Boos, N., Wallin, A., Gbedegbegnon, T., Aebi, M., Boesch, C., (1993). Quantitative MR imaging of lumbar intervertebral disks and vertebral bodies: influence of diurnal water content variations. Radiology 188, 351-354.

Buckwalter, J. A., (1995). Aging and degeneration of the human intervertebral disc. Spine 20, 1307-1314.

Bull, H. B., Breese, K., (1969). Electric conductance of protein solutions. Journal of Colloid and Interface Science 29, 492-495.

Burstein, D., Gray, M. L., Hartman, A. L., Gipe, R., Foy, B. D., (1993). Diffusion of small solutes in cartilage as measured by nuclear magnetic resonance (NMR) spectroscopy and imaging. J Orthop Res 11, 465-478.

Cassinelli, E. H., Hall, R. A., Kang, J. D., (2001). Biochemistry of intervertebral disc degeneration and the potential for gene therapy applications. Spine J. 1, 205-214.

Chammas, P., (1989). Electromechanical coupling in articular cartilage: and electromechanical micromodel and experimental results. MS Boston University.

Chen, A. C., Nguyen, T. T., Sah, R. L., (1997). Streaming potentials during the confined compression creep test of normal and proteoglycan-depleted cartilage. Ann.Biomed.Eng 25, 269-277.

Chen, J., Yan, W., Setton, L. A., (2006). Molecular phenotypes of notochordal cells purified from immature nucleus pulposus. Eur.Spine J. 15 Suppl 3, S303-S311.

Chiu, E. J., Newitt, D. C., Segal, M. R., Hu, S. S., Lotz, J. C., Majumdar, S., (2001). Magnetic resonance imaging measurement of relaxation and water diffusion in the human lumbar intervertebral disc under compression in vitro. Spine 26, E437-E444.

Cohen, B., Lai, W. M., Mow, V. C., (1998). A transversely isotropic biphasic model for unconfined compression of growth plate and chondroepiphysis. J.Biomech.Eng 120, 491-496.

Cole, T. C., Ghosh, P., Taylor, T. K., (1986). Variations of the proteoglycans of the canine intervertebral disc with ageing. Biochim.Biophys.Acta 880, 209-219.

Concaro, S., Gustavson, F., Gatenholm, P., (2009). Bioreactors for tissue engineering of cartilage. Adv.Biochem.Eng Biotechnol. 112, 125-143.

Cs-Szabo, G., Ragasa-San, J. D., Turumella, V., Masuda, K., Thonar, E. J., An, H. S., (2002). Changes in mRNA and protein levels of proteoglycans of the anulus fibrosus and nucleus pulposus during intervertebral disc degeneration. Spine (Phila Pa 1976.) 27, 2212-2219.

Curnier, A., He, Q.-C., Zysset, P., (1995). Conewise Linear Elastic Materials. J.Elasticity 37, 1-38.

Darling, E. M., Athanasiou, K. A., (2003). Articular cartilage bioreactors and bioprocesses. Tissue Eng 9, 9-26.

Deyo, R. A., (1998). Low-back pain. Sci.Am. 279, 48-53.

Donnan, F. G., (1924). The theory of membrane equilibria. Chem Rev 1, 73-90.

Drew, S. C., Silva, P., Crozier, S., Pearcy, M. J., (2004). A diffusion and T2 relaxation MRI study of the ovine lumbar intervertebral disc under compression in vitro. Phys Med Biol 49, 3585-3592.

Eisenberg, S. R., Grodzinsky, A. J., (1985). Swelling of articular cartilage and other connective tissues: electromechanochemical forces. J Orthop Res 3, 148-159.

Eisenberg, S. R., Grodzinsky, A. J., (1987). The kinetics of chemically induced nonequilibrium swelling of articular cartilage and corneal stroma. J Biomech Eng 109, 79-89.

Errico, T. J., (2005). Lumbar disc arthroplasty. Clin.Orthop.Relat Res. 106-117.

Eyre, D. R., Benya, P., Buckwalter, J., Caterson, B., Heinegard, D., Oegema, T., Pearce, R., Pope, M., Urban, J., (1989). Intervertebral disk: Basic science perspectives. In: Frymoyer, J. W., Gordon, S. L. (Eds.), New Perspectives on Low Back Pain. American Academy of Orthopaedic Surgeons, Park Ridge, IL, pp. 147-207.

Ferguson, S. J., Steffen, T., (2003). Biomechanics of the aging spine. Eur.Spine J. 12 Suppl 2, S97-S103.

Frank, E. H., Grodzinsky, A. J., (1987a). Cartilage electromechanics--I. Electrokinetic transduction and the effects of electrolyte pH and ionic strength. J.Biomech. 20, 615-627.

Frank, E. H., Grodzinsky, A. J., (1987b). Cartilage electromechanics--II. A continuum model of cartilage electrokinetics and correlation with experiments. J.Biomech. 20, 629-639.

Frank, E. H., Grodzinsky, A. J., Koob, T. J., Eyre, D. R., (1987). Streaming potentials: a sensitive index of enzymatic degradation in articular cartilage. J.Orthop.Res. 5, 497-508.

Frank, E. H., Jin, M., Loening, A. M., Levenston, M. E., Grodzinsky, A. J., (2000). A versatile shear and compression apparatus for mechanical stimulation of tissue culture explants. J Biomech 33, 1523-1527.

Freed, L. E., Hollander, A. P., Martin, I., Barry, J. R., Langer, R., Vunjak-Novakovic, G., (1998). Chondrogenesis in a cell-polymer-bioreactor system. Exp.Cell Res. 240, 58-65.

Freed, L. E., Vunjak-Novakovic, G., (1995). Cultivation of cell-polymer tissue constructs in simulated microgravity. Biotechnol.Bioeng. 46, 306.

Freyria, A. M., Cortial, D., Ronziere, M. C., Guerret, S., Herbage, D., (2004). Influence of medium composition, static and stirred conditions on the proliferation of and matrix protein expression of bovine articular chondrocytes cultured in a 3-D collagen scaffold. Biomaterials 25, 687-697.

Freyria, A. M., Yang, Y., Chajra, H., Rousseau, C. F., Ronziere, M. C., Herbage, D., El Haj, A. J., (2005). Optimization of dynamic culture conditions: effects on biosynthetic activities of chondrocytes grown in collagen sponges. Tissue Eng 11, 674-684.

Garon, M., Legare, A., Guardo, R., Savard, P., Buschmann, M. D., (2002). Streaming potentials maps are spatially resolved indicators of amplitude, frequency and ionic strength dependant responses of articular cartilage to load. J Biomech. 35, 207-216.

Grodzinsky, A. J., (1983). Electromechanical and physicochemical properties of connective tissue. Crit Rev.Biomed.Eng 9, 133-199.

Grodzinsky, A. J., Lipshitz, H., Glimcher, M. J., (1978). Electromechanical properties of articular cartilage during compression and stress relaxation. Nature 275, 448-450.

Gruber, H. E., Fisher, E. C., Jr., Desai, B., Stasky, A. A., Hoelscher, G., Hanley, E. N., Jr., (1997). Human intervertebral disc cells from the annulus: three-dimensional culture in agarose or alginate and responsiveness to TGF-beta1. Exp.Cell Res 235, 13-21.

Gruber, H. E., Hanley, E. N., Jr., (1998). Analysis of aging and degeneration of the human intervertebral disc. Comparison of surgical specimens with normal controls. Spine (Phila Pa 1976.) 23, 751-757.

Gruber, H. E., Hanley, E. N., Jr., (2002). Ultrastructure of the human intervertebral disc during aging and degeneration: comparison of surgical and control specimens. Spine 27, 798-805.

Gruber, H. E., Leslie, K., Ingram, J., Hoelscher, G., Norton, H. J., Hanley, E. N., Jr., (2004). Colony formation and matrix production by human anulus cells: modulation in three-dimensional culture. Spine 29, E267-E274.

Gu, W. Y., Justiz, M. A., (2002). Apparatus for measuring the swelling dependent electrical conductivity of charged hydrated soft tissues. J Biomech Engng 124, 790-793.

Gu, W. Y., Justiz, M. A., Yao, H., (2002). Electrical conductivity of lumbar annulus fibrosis: Effects of porosity and fixed charge density. Spine 27, 2390-2395.

Gu, W. Y., Lai, W. M., Mow, V. C., (1993). Transport of fluid and ions through a porous-permeable charged-hydrated tissue, and streaming potential data on normal bovine articular cartilage. J Biomech 26, 709-723.

Gu, W. Y., Lai, W. M., Mow, V. C., (1997a). A triphasic analysis of negative osmotic flows through charged hydrated soft tissues. J Biomech 30, 71-78.

Gu, W. Y., Lai, W. M., Mow, V. C., (1998). A mixture theory for charged-hydrated soft tissues containing multi- electrolytes: passive transport and swelling behaviors. Journal of Biomechanical Engineering 120, 169-180.

Gu, W. Y., Lai, W. M., Mow, V. C., (1999a). Transport of multi-electrolytes in charged hydrated biological soft tissues. Transport in Porous Media 34, 143-157.

Gu, W. Y., Lewis, B., Saed-Nejad, F., Lai, W. M., Ratcliffe, A., (1997b). Hydration and true denstiy of normal and PG-depleted bovine articular cartilage. Trans Orthop Res Soc 22, 826.

Gu, W. Y., Lewis, B., Lai, W. M., Ratcliffe, A., Mow, V. C., (1996). A technique for measuring volume and true density of the solid matrix of cartilaginous tissues. Advances in Bioengineering, ASME BED33, 89-90.

Gu, W. Y., Mao, X. G., Foster, R. J., Weidenbaum, M., Mow, V. C., Rawlins, B. A., (1999b). The anisotropic hydraulic permeability of human lumbar anulus fibrosus. Influence of age, degeneration, direction, and water content. Spine 24, 2449-2455.

Gu, W. Y., Mao, X. G., Rawlins, B. A., Iatridis, J. C., Foster, R. J., Sun, D. N., Weidenbaum, M., Mow, V. C., (1999c). Streaming potential of human lumbar anulus fibrosus is anisotropic and affected by disc degeneration. J Biomech 32, 1177-1182.

Gu, W. Y., Yao, H., Huang, C.-Y., Cheung, H. S., (2003). New insight into deformation-dependent hydraulic permeability of gels and cartilage, and dynamic behavior of agarose gels in confined compression. J Biomech 36, 593-598.

Gu, W. Y., Yao, H., Vega, A. L., Flagler, D., (2004). Diffusivity of ions in agarose gels and intervertebral disc: Effect of porosity. Annals of Biomed Engng 32, 1710-1717.

Guilak, F., Ting-Beall, H. P., Baer, A. E., Trickey, W. R., Erickson, G. R., Setton, L. A., (1999). Viscoelastic properties of intervertebral disc cells. Identification of two biomechanically distinct cell populations. Spine 24, 2475-2483.

Guiot, B. H., Fessler, R. G., (2000). Molecular biology of degenerative disc disease. Neurosurgery 47, 1034-1040.

Harvey Lodish, Arnold Berk, Paul Matsudaira, Chris A.Kaiser, Monty Krieger, Matthew P.Scott, S.Lawrence Zipursky, James Darnell, (2003). Molecular cell biology. Sara Tenney.

Hasegawa, I., Kuriki, S., Matsuno, S., Matsumoto, G., (1983). Dependence of electrical conductivity on fixed charge density in articular cartilage. Clin Orthop 283-288.

Haselgrove, J. C., Shapiro, I. M., Silverton, S. F., (1993). Computer modeling of the oxygen supply and demand of cells of the avian growth cartilage. Am.J.Physiol 265, C497-C506.

Heinegard, D., Paulsson, M., Inerot, S., Carlstrom, C., (1981). A novel low-molecular weight chondroitin sulphate proteoglycan isolated from cartilage. Biochem.J. 197, 355-366.

Helfferich, F., (1962). Ion Exchange. McGraw Hill Book Company, Inc, New York.

Hendry, N. G. C., (1958). The hydration of the neuclus pulposus and its relation to intervertebral disc derangement. J Bone Joint Surg 40 B, 132-144.

Heywood, H. K., Bader, D. L., Lee, D. A., (2006). Rate of oxygen consumption by isolated articular chondrocytes is sensitive to medium glucose concentration. J.Cell Physiol 206, 402-410.

Hickey, D. S., Hukins, D. W. L., (1980). Relation between the structure of the anulus fibrosus and the function and failure of the intervertebral disc. Spine 5, 106-116.

Hilibrand, A. S., Robbins, M., (2004). Adjacent segment degeneration and adjacent segment disease: the consequences of spinal fusion? Spine J. 4, 190S-194S.

Himmelblau D.M., (1964). Diffusion of dissolved gases in liquids. Chem.Rev 64, 527-550.

Holm, S., Maroudas, A., Urban, J. P., Selstam, G., Nachemson, A., (1981). Nutrition of the intervertebral disc: solute transport and metabolism. Connect.Tissue Res 8, 101-119.

Holm, S., Nachemson, A., (1982). Nutritional changes in the canine intervertebral disc after spinal fusion. Clin.Orthop 243-258.

Horner, H. A., Roberts, S., Bielby, R. C., Menage, J., Evans, H., Urban, J. P., (2002). Cells from different regions of the intervertebral disc: effect of culture system on matrix expression and cell phenotype. Spine 27, 1018-1028.

Horner, H. A., Urban, J. P., (2001). 2001 Volvo Award Winner in Basic Science Studies: Effect of nutrient supply on the viability of cells from the nucleus pulposus of the intervertebral disc. Spine 26, 2543-2549.

Hsu, E. W., Setton, L. A., (1999). Diffusion tensor microscopy of the intervertebral disc anulus fibrosus. Magn Reson.Med 41, 992-999.

Huang, C. Y., Deitzer, M. A., Cheung, H. S., (2007). Effects of fibrinolytic inhibitors on chondrogenesis of bone-marrow derived mesenchymal stem cells in fibrin gels. Biomech.Model.Mechanobiol. 6, 5-11.

Huang, C. Y., Mow, V. C., Ateshian, G. A., (2001). The role of flow-independent viscoelasticity in the biphasic tensile and compressive responses of articular cartilage. J Biomech Eng 123, 410-417.

Huang, C. Y., Soltz, M. A., Kopacz, M., Mow, V. C., Ateshian, G. A., (2003). Experimental verification of the roles of intrinsic matrix viscoelasticity and tension-compression nonlinearity in the biphasic response of cartilage. J.Biomech.Eng 125, 84-93.

Iatridis, J. C., ap Gwynn, I., (2004). Mechanisms for mechanical damage in the intervertebral disc annulus fibrosus. J Biomech 37, 1165-1175.

Ishihara, H., Urban, J. P., (1999). Effects of low oxygen concentrations and metabolic inhibitors on proteoglycan and protein synthesis rates in the intervertebral disc. J Orthop Res 17, 829-835.

Jackson, A. R., Yao, H., Brown, M. D., Gu, W. Y., (2006). Anisotropic ion diffusivity in intervertebral disc: an electrical conductivity approach. Spine 31, 2783-2789.

Jackson, A. R., Yuan, T. Y., Huang, C. Y., Travascio, F., Gu, W. Y., (2008). Effect of compression and anisotropy on the diffusion of glucose in annulus fibrosus. Spine 33, 1-7.

Jahnke, M. R., McDevitt, C. A., (1988). Proteoglycans of the human intervertebral disc. Electrophoretic heterogeneity of the aggregating proteoglycans of the nucleus pulposus. Biochem.J 251, 347-356.

Janz, G. J., Ives, D. J. G., (1968). Silver, silver chloride electrodes. Annals of the New York Academy of Sciences 148, 210-221.

Johnstone, B., Urban, J. P., Roberts, S., Menage, J., (1992). The fluid content of the human intervertebral disc. Comparison between fluid content and swelling pressure profiles of discs removed at surgery and those taken postmortem. Spine 17, 412-416.

Kalson, N. S., Richardson, S., Hoyland, J. A., (2008). Strategies for regeneration of the intervertebral disc. Regen.Med. 3, 717-729.

Katchalsky, A., Curran, P. F., (1975). Nonequilibrium Thermodynamics in Biophysics. Harvard University Press, Cambridge, MA.

Katz, M. M., Hargens, A. R., Garfin, S. R., (1986). Intervertebral disc nutrition. Diffusion versus convection. Clin.Orthop 243-245.

Kelsey, J. L., Mundt, D. F., Golden, A. L., (1992). Epidemiology of low back pain. In: Malcolm, J. I. V. (Ed.), The Lumbar Spine and Back Pain. Churchill Livingstone, New York, pp. 537-549.

Kelsey, J. L., Pastides, H., Bisbee, G. E., (1978). Musculoskeletal Disorders: Their Frequency of Occurrence and Their Impact on the Population of the United States. Prodist, New York.

Kelsey, J. L., White, A. A., (1980). Epidemiology and impact of low-back pain. Spine 5, 133-142.

Kelsey, J. L., White, A. A., III, Pastides, H., Bisbee, G. E., Jr., (1979). The impact of musculoskeletal disorders on the population of the United States. J Bone Joint Surg Am. 61, 959-964.

Kempson, G. E., Freeman, M. A., Swanson, S. A., (1968). Tensile properties of articular cartilage. Nature 220, 1127-1128.

Knospe, C., (2006). PID control. IEEE Control Systems Magazine 26, 30-31.

Kraemer, J., Kolditz, D., Gowin, R., (1985). Water and electrolyte content of human intervertebral discs under variable load. Spine 10, 69-71.

Lai, W. M., Hou, J. S., Mow, V. C., (1989). A triphasic theory for articular cartilage swelling. Proc Biomech Symp ASME AMD98, 33-36.

Lai, W. M., Hou, J. S., Mow, V. C., (1991). A triphasic theory for the swelling and deformation behaviors of articular cartilage. J Biomech Eng 113, 245-258.

Laible, J. P., Pflaster, D., Simon, B. R., Krag, M. H., Pope, M., Haugh, L. D., (1994). A dynamic material parameter estimation procedure for soft tissue using a poroelastic finite element model. J Biomech Eng 116, 19-29.

Langer, R., Vacanti, J. P., (1993). Tissue engineering. Science 260, 920-926.

LeBaron, R. G., Athanasiou, K. A., (2000). Ex vivo synthesis of articular cartilage. Biomaterials 21, 2575-2587.

Lee, R. C., Frank, E. H., Grodzinsky, A. J., Roylance, D. K., (1981). Oscillatory compressional behavior of articular cartilage and its associated electro-mechanical properties. J.Biomech Eng 103, 280-292.

Lotke, P. A., Black, J., Richardson, S. J., (1974). Electromechanical properties in human articular cartilage. J Bone Joint Surg 56A, 1040-1046.

Lundon, K., Bolton, K., (2001). Structure and function of the lumbar intervertebral disk in health, aging, and pathologic conditions. J Orthop Sports Phys.Ther. 31, 291-303.

Lyons, G., Eisenstein, S. M., Sweet, M. B., (1981). Biochemical changes in intervertebral disc degeneration. Biochim.Biophys.Acta 673, 443-453.

Macpherson, J. V., O'Hare, D., Unwin, P. R., Winlove, C. P., (1997). Quantitative spatially resolved measurements of mass transfer through laryngeal cartilage. Biophysical Journal 73, 2771-2781.

Mahmoudifar, N., Doran, P. M., (2005). Tissue engineering of human cartilage and osteochondral composites using recirculation bioreactors. Biomaterials 26, 7012-7024.

Mak, A. F., (1986). The apparent viscoelastic behavior of articular cartilage--the contributions from the intrinsic matrix viscoelasticity and interstitial fluid flows. J.Biomech.Eng 108, 123-130.

Malda, J., Rouwkema, J., Martens, D. E., Le Comte, E. P., Kooy, F. K., Tramper, J., van Blitterswijk, C. A., Riesle, J., (2004). Oxygen gradients in tissue-engineered PEGT/PBT cartilaginous constructs: measurement and modeling. Biotechnol.Bioeng. 86, 9-18.

Maldonado, B. A., Oegema, T. R., Jr., (1992). Initial characterization of the metabolism of intervertebral disc cells encapsulated in microspheres. J.Orthop.Res. 10, 677-690.

Marchand, F., Ahmed, A. M., (1990). Investigation of the laminate structure of lumbar disc anulus fibrosus. Spine 15, 402-410.

Maroudas, A., (1968). Physicochemical properties of cartilage in the light of ion exchange theory. Biophys.J 8, 575-595.

Maroudas, A., (1975). Biophysical chemistry of cartilaginous tissues with special reference to solute and fluid transport. Biorheology 12, 233-248.

Maroudas, A., (1979). Physicochemical properties of articular cartilage. In: Freeman, M. A. R. (Ed.), Adult Articular Cartilage. Pitman Medical, pp. 215-290.

Maroudas, A., Bullough, P., Swanson, S. A., Freeman, M. A., (1968). The permeability of articular cartilage. J Bone Joint Surg Br. 50, 166-177.

Maroudas, A., Muir, H., Wingham, J., (1969). The correlation of fixed negative charge with glycosaminoglycan content of human articular cartilage. Biochim.Biophys.Acta 177, 492-500.

Maroudas, A., Stockwell, R. A., Nachemson, A., Urban, J., (1975). Factors involved in the nutrition of the human lumbar intervertebral disc: cellularity and diffusion of glucose in vitro. J Anat. 120, 113-130.

Marsano, A., Wendt, D., Raiteri, R., Gottardi, R., Stolz, M., Wirz, D., Daniels, A. U., Salter, D., Jakob, M., Quinn, T. M., Martin, I., (2006). Use of hydrodynamic forces to engineer cartilaginous tissues resembling the non-uniform structure and function of meniscus. Biomaterials 27, 5927-5934.

Martin, I., Obradovic, B., Freed, L. E., Vunjak-Novakovic, G., (1999). Method for quantitative analysis of glycosaminoglycan distribution in cultured natural and engineered cartilage. Ann.Biomed.Eng 27, 656.

Martin, I., Obradovic, B., Treppo, S., Grodzinsky, A. J., Langer, R., Freed, L. E., Vunjak-Novakovic, G., (2000). Modulation of the mechanical properties of tissue engineered cartilage. Biorheology 37, 141-147.

Martin, I., Wendt, D., Heberer, M., (2004). The role of bioreactors in tissue engineering. Trends Biotechnol. 22, 80-86.

Miller, J. A. A., Schmatz, C., Schultz, A. B., (1988). Lumbar disc degeneration: Correlation with age, sex, and spine level in 600 autopsy specimens. Spine 13, 173-178.

Minuth, W. W., Strehl, R., Schumacher, K., de, V. U., (2001). Long term culture of epithelia in a continuous fluid gradient for biomaterial testing and tissue engineering. J.Biomater.Sci.Polym.Ed 12, 353-365.

Mitchell, P. E. G., Hendryand, N. G. C., Billewicz, W. Z., (1961). The chemical background of intervertebral disc prolapse. J Bone Joint Surg 43B, 141-151.

Mizuno, S., Alleman, F., Glowachi, J., (2001). Effects of medium perfusion on matrix production by bovine chondrocytes in three-dimensional collagen sponges. J Biomed Mater Res 56, 368-375.

Mow, V. C., Kuei, S. C., Lai, W. M., Armstrong, C. G., (1980). Biphasic creep and stress relaxation of articular cartilage in compression: Theory and experiments. J Biomech Eng 102, 73-84.

Mow, V. C., Ratcliffe, A., Poole, A. R., (1992). Cartilage and diarthrodial joints as paradiams for hierarchical materials and structures. Biomaterials 13, 67-97.

Mow, V. C., Wang, C. C., Hung, C. T., (1999). The extracellular matrix, interstitial fluid and ions as a mechanical signal transducer in articular cartilage. Osteoarthritis.Cartilage. 7, 41-58.

Muir, H., (1980). The chemistry of the ground substance of joint cartilage. In: Sokolff, L. (Ed.), The Joints and Synovial Fluid. Academic Press, pp. 27-94.

Muir, H., (1983). Proteoglycons as organizers of the extracellular matrix. Biochemistry Society Transactions 613-622.

Myers, E. R., Lai, W. M., Mow, V. C., (1984). A continuum theory and an experiment for the ion-induced swelling behavior of articular cartilage. J Biomech Eng 106, 151-158.

Nachemson, A., Lewin, T., Maroudas, A., Freeman, M. A., (1970). In vitro diffusion of dye through the end-plates and the annulus fibrosus of human lumbar inter-vertebral discs. Acta Orthop Scand. 41, 589-607.

National Institutes of Health., (2004). Low back pain fact sheet for patients and the public. J Pain Palliat.Care Pharmacother. 18, 95-110.

Nerem, R. M., (1991). Cellular engineering. Ann.Biomed.Eng 19, 529-545.

Nerlich, A. G., Boos, N., Wiest, I., Aebi, M., (1998). Immunolocalization of major interstitial collagen types in human lumbar intervertebral discs of various ages. Virchows Arch. 432, 67-76.

Nerlich, A. G., Schleicher, E. D., Boos, N., (1997). 1997 Volvo Award winner in basic science studies. Immunohistologic markers for age-related changes of human lumbar intervertebral discs. Spine 22, 2781-2795.

Ngwa, W., Geier, O., Stallmach, F., Naji, L., Schiller, J., Arnold, K., (2002). Cation diffusion in cartilage measured by pulsed field gradient NMR. Eur Biophys J 31, 73-80.

NIH, (1997). Research on low back pain and common spinal disorders. NIH Guide 26.

O'Halloran, D. M., Pandit, A. S., (2007). Tissue-engineering approach to regenerating the intervertebral disc. Tissue Eng 13, 1927-1954.

O'Hare, D., Winlove, C. P., Parker, K. H., (1991). Electrochemical method for direct measurement of oxygen concentration and diffusivity in the intervertebral disc: electrochemical characterization and tissue-sensor interactions. J Biomed Eng 13, 304-312.

Oegema, T. R., Jr., (1993). Biochemistry of the intervertebral disc. Clin.Sports Med. 12, 419-439.

Ogata, K., Whiteside, L. A., (1981). 1980 Volvo award winner in basic science. Nutritional pathways of the intervertebral disc. An experimental study using hydrogen washout technique. Spine 6, 211-216.

Ohshima, H., Ishihara, H., Urban, J. P., Tsuji, H., (1993). The use of coccygeal discs to study intervertebral disc metabolism. J Orthop Res 11, 332-338.

Ohshima, H., Tsuji, H., Hiarano, N., Ishihara, H., Katoh, Y., Yamada, H., (1989). Water diffusion pathway, swelling pressure, and biomechanical properties of the intervertebral disc during compression load. Spine 14, 1234-1244.

Panagiotacopulos, N. D., Pope, M. H., Krag, M. H., Block, R., (1987). Water content in human intervertebral discs. Part I. Measurement by magnetic resonance imaging. Spine 12, 912-917.

Paul Acarnely, (2002). Stepping Motors: A Guide to Theory and Practice. The Institution of Engineering and Technology.

Pazzano, D., Mercier, K. A., Moran, J. M., Fong, S. S., DiBiasio, D. D., Rulfs, J. X., Kohles, S. S., Bonassar, L. J., (2000). Comparison of chondrogensis in static and perfused bioreactor culture. Biotechnol Prog 16, 893-896.

Pearce, R. H., (1993). Morphologic and Chemical Aspects of Aging. In: Wood, D. O., Goldberg, V. M., Woo, S. L. (Eds.), Musculoskeletal Soft-Tissue Aging: Impact on Mobility. American Academy of Orthopaedic Surgeons, Rosemont, IL, pp. 363-379.

Pei, M., Solchaga, L. A., Seidel, J., Zeng, L., Vunjak-Novakovic, G., Caplan, A. I., Freed, L. E., (2002). Bioreactors mediate the effectiveness of tissue engineering scaffolds. FASEB J. 16, 1691-1694.

Portner, R., Nagel-Heyer, S., Goepfert, C., Adamietz, P., Meenen, N. M., (2005). Bioreactor design for tissue engineering. J.Biosci.Bioeng. 100, 235-245.

Quinn, T. M., Kocian, P., Meister, J. J., (2000). Static compression is associated with decreased diffusivity of dextrans in cartilage explants. Arch Biochem Biophys 384, 327-334.

Quinn, T. M., Morel, V., Meister, J. J., (2001). Static compression of articular cartilage can reduce solute diffusivity and partitioning: implications for the chondrocyte biological response. J Biomech 34, 1463-1469.

R.K.Rajput, (2005). Basic Electrical Engineering. Laxmi Publications.

Roberts, S., Caterson, B., Evans, H., Eisenstein, S. M., (1994). Proteoglycan components of the intervertebral disc and cartilage endplate: an immunolocalization study of animal and human tissues. Histochem.J 26, 402-411.

Roberts, S., Menage, J., Urban, J. P., (1989). Biochemical and structural properties of the cartilage end-plate and its relation to the intervertebral disc. Spine 14, 166-174.

Roth, V., Mow, V. C., (1980). The intrinsic tensile behavior of the matrix of bovine articular cartilage and its variation with age. J.Bone Joint Surg.Am. 62, 1102-1117.

Schepps, J. L., Foster, K. R., (1980). The UHF and microwave dielectric properties of normal and tumour tissues: variation in dielectric properties with tissue water content. Phys.Med.Biol. 25, 1149-1159.

Schinagl, R. M., Gurskis, D., Chen, A. C., Sah, R. L., (1997). Depth-dependent confined compression modulus of full-thickness bovine articular cartilage. J Orthop Res 15, 499-506.

Selard, E., Shirazi-Adl, A., Urban, J., (2003). Finite Element Study of Nutrient Diffusion in the Human Intervertebral Disc. Spine 28, 1945-1953.

Setton, L. A., Zhu, W. B., Mow, V. C., (1993). The biphasic poroviscoelastic behavior of articular cartilage: Role of the surface zone in governing the compressive behavior. J Biomechanics 26, 581-592.

Skalak Richard, Fox C.Fred, (1988). Tissue Engineering.

Smith, S. R., Foster, K. R., (1985). Dielectric properties of low-water-content tissues. Phys.Med.Biol. 30, 965-973.

Soltz, M. A., Ateshian, G. A., (2000). A Conewise Linear Elasticity mixture model for the analysis of tension- compression nonlinearity in articular cartilage. J Biomech Eng 122, 576-586.

Soulhat, J., Buschmann, M. D., Shirazi-Adl, A., (1999). A fibril-network-reinforced biphasic model of cartilage in unconfined compression. J Biomech Eng 121, 340-347.

Stockwell, R. A., (1979). Biology of Cartilage Cells. Cambridge University Press, Cambridge, UK.

Strehl, R., Tallheden, T., Sjogren-Jansson, E., Minuth, W. W., Lindahl, A., (2005). Long-term maintenance of human articular cartilage in culture for biomaterial testing. Biomaterials 26, 4540-4549.

Tognana, E., Chen, F., Padera, R. F., Leddy, H. A., Christensen, S. E., Guilak, F., Vunjak-Novakovic, G., Freed, L. E., (2005). Adjacent tissues (cartilage, bone) affect the functional integration of engineered calf cartilage in vitro. Osteoarthritis.Cartilage. 13, 129-138.

Travascio, F., Gu, W. Y., (2007). Anisotropic diffusive transport in annulus fibrosus: experimental determination of the diffusion tensor by FRAP technique. Ann.Biomed.Eng 35, 1739-1748.

Travascio, F., Jackson, A. R., Brown, M. D., Gu, W. Y., (2009). Relationship between solute transport properties and tissue morphology in human annulus fibrosus. J.Orthop.Res. 27, 1625-1630.

Tsao, Y. D., Gonda, S. R., (1999). A new technology for three-dimensional cell culture: The dynamic focusing bioreactor. Heat Mass Transfer Biotechnol. 363, 37.

Urban, J. P., (2001). The role of the physicochemical environment in determining disc cell behaviour. Biochem.Soc Trans 30, 858-864.

Urban, J. P., Holm, S., Maroudas, A., (1978). Diffusion of small solutes into the intervertebral disc: as in vivo study. Biorheology 15, 203-221.

Urban, J. P., Holm, S., Maroudas, A., Nachemson, A., (1982). Nutrition of the intervertebral disc: Effect of fluid flow on solute transport. Clin Orthop 170, 296-302.

Urban, J. P., Maroudas, A., (1981). Swelling of the intervertebral disc in vitro. Connect Tissue Res 9, 1-10.

Urban, J. P., McMullin, J. F., (1985). Swelling pressure of the intervertebral disc: influence of proteoglycan and collagen contents. Biorheology 22, 145-157.

Urban, J. P., McMullin, J. F., (1988). Swelling pressure of the lumbar intervertebral discs: influence of age, spinal level, composition, and degeneration. Spine 13, 179-187.

Urban, J. P., Roberts, S., (1995). Development and degeneration of the intervertebral discs. Mol.Med Today 1, 329-335.

Urban, J. P. G., Holms, S., Maroudas, A., Nachemson, A., (1977). Nutrition of the intervertebral disc: An in vivo study of solute transport. Clin Orthop 129, 101-114.

Urban, J. P. G., Maroudas, A., (1980). The chemistry of the intervertebral disc in relation to its physiological function and requirements. Clinics in Rheumatic Diseases 6, 51-77.

Urban, J. P. G., Roberts, S., (2003). Degeneration of the intervertebral disc. Arthritis Research & Therapy 5, 120-130.

van der, R. N., Goossens, M. E., Evers, S. M., van Tulder, M. W., (2005). What is the most cost-effective treatment for patients with low back pain? A systematic review. Best.Pract.Res.Clin.Rheumatol. 19, 671-684.

Vunjak-Novakovic, G., Freed, L. E., (1998). Culture of organized cell communities. Adv.Drug Deliv.Rev. 33, 15-30.

Vunjak-Novakovic, G., Freed, L. E., Biron, R. J., Langer, R., (1996). Effects of mixing on the composition and morphology of tissue-engineered cartilage. AIChE Journal 42, 850.

Vunjak-Novakovic, G., Martin, I., Obradovic, B., Treppo, S., Grodzinsky, A. J., Langer, R., Freed, L. E., (1999). Bioreactor cultivation conditions modulate the composition and mechanical properties of tissue-engineered cartilage. J Orthop Res 17, 130-138.

Vunjak-Novakovic, G., Obradovic, B., Martin, I., Bursac, P. M., Langer, R., Freed, L. E., (1998). Dynamic cell seeding of polymer scaffolds for cartilage tissue engineering. Biotechnol Prog 14, 193.

Walker, M. H., Anderson, D. G., (2004). Molecular basis of intervertebral disc degeneration. Spine J. 4, 158S-166S.

Weiss, J. A., Maakestad, B. J., (2006). Permeability of human medial collateral ligament in compression transverse to the collagen fiber direction. J.Biomech. 39, 276-283.

Wendt, D., Marsano, A., Jakob, M., Heberer, M., Martin, I., (2003). Oscillating perfusion of cell suspensions through three-dimensional scaffolds enhances cell seeding efficiency and uniformity. Biotechnol.Bioeng. 84, 205-214.

White, A. A., (1981). Biomechanics of lumbar spine and sacroiliac articulation: relevance to idiopathic low back pain. In: White, A. A., Gordon, S. L. (Eds.), Symposium on Idiopathic Low Back Pain. CV Mosby Co., St. Louis, pp. 296-322.

White, A. A., Panjabi, M. M., (1978). Physical properties and functional biomechanics of the spine. In: White, A. A., Panjabi, M. M. (Eds.), Clinical Biomechanics of the Spine. JB Lippincott, Philadelphia.

Wilson, C. G., Bonassar, L. J., Kohles, S. S., (2002). Modeling the dynamic composition of engineered cartilage. Arch.Biochem.Biophys. 408, 246-254.

Woo, S. L., Lubock, P., Gomez, M. A., Jemmott, G. F., Kuei, S. C., Akeson, W. H., (1979). Large deformation nonhomogeneous and directional properties of articular cartilage in uniaxial tension. J.Biomech. 12, 437-446.

Yao, H., Gu, W. Y., (2002). New insight into deformation-dependent hydraulic permeability of hydrogels and cartilage. Advances in Bioengineering, ASME 53, #32520.

Appendix A
OXYGEN DIFFUSION CHAMBER (UNIT: INCH)
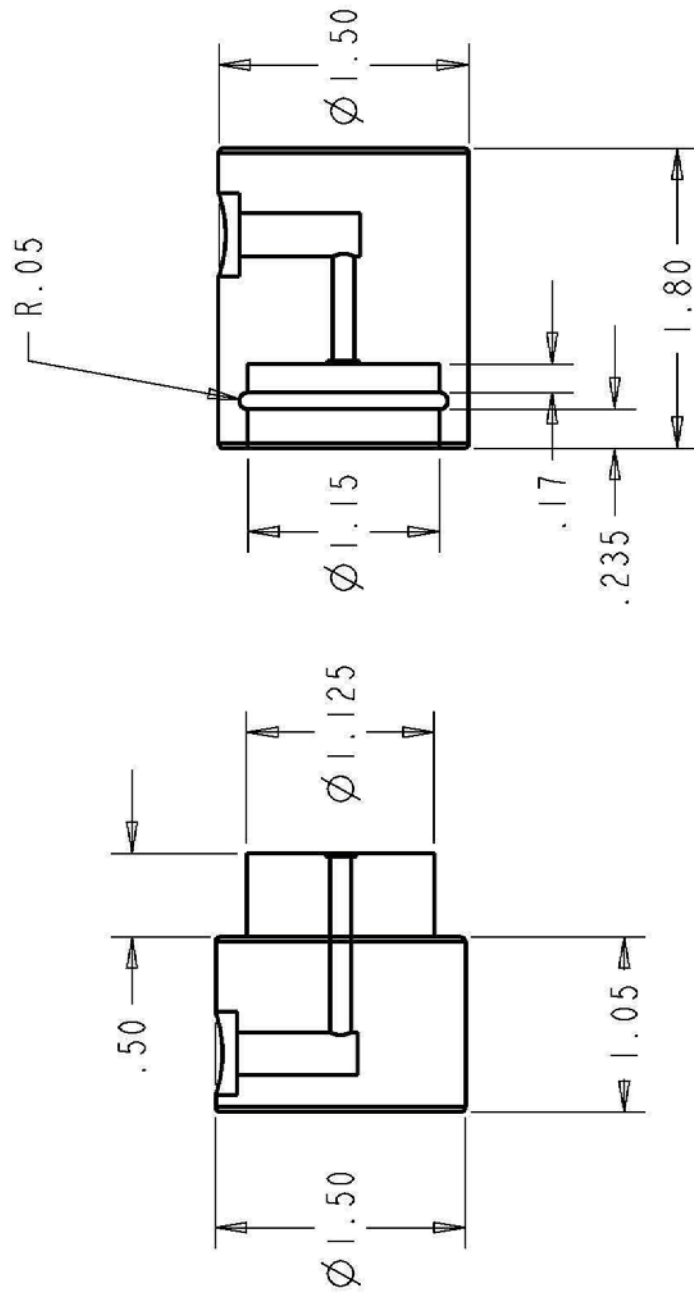
Appendix B

PERFUSION CHAMBER (UNIT: MM)
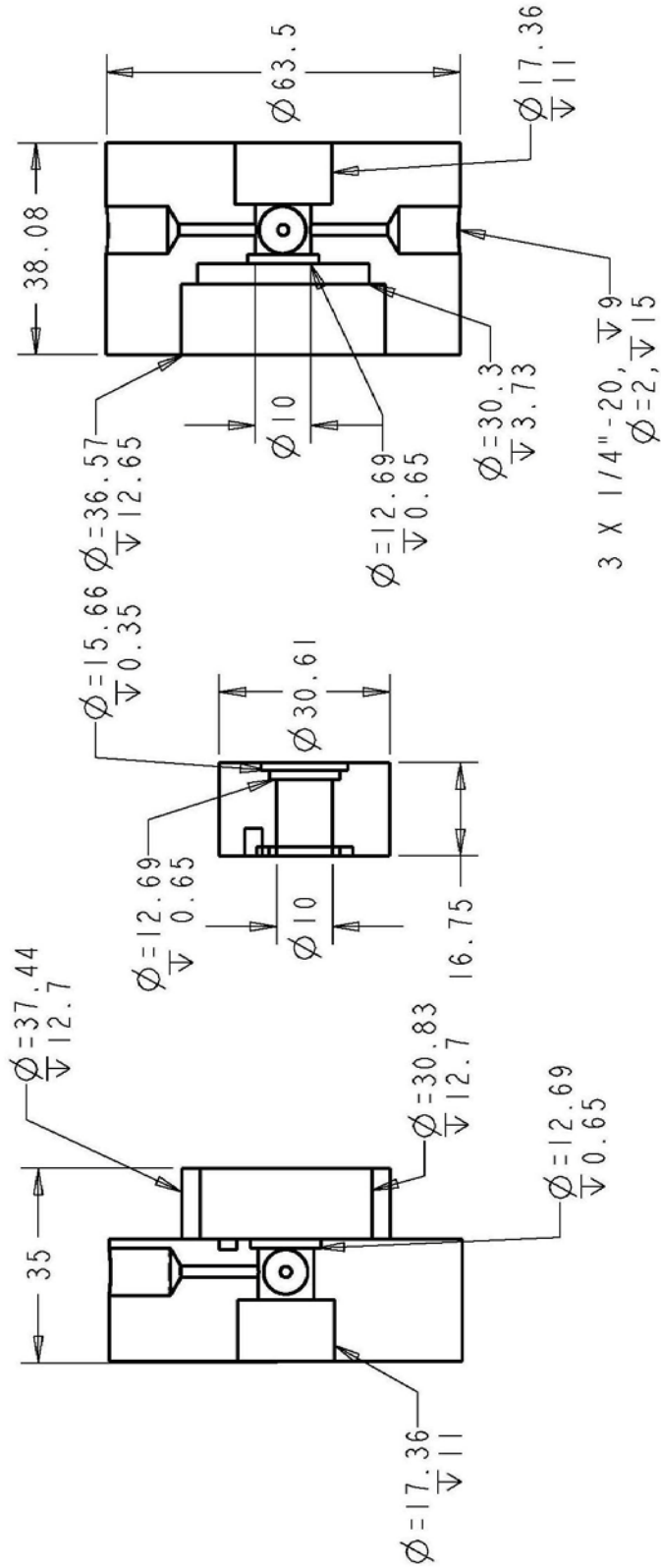
Appendix C

**OPERATIONAL PROCEDURE FOR MECHANO-ELECTROCHEMICAL
MEASUREMENT SYSTEM**

Conductivity calibration and Measurement

1) Turn on Thermo Orion 4 Star meter and connect the conductivity 4 cell carbon
   probe to meter.

2) Press "Line select" until the arrow icon is pointing to the conductivity
   measurement line.

3) Press "calibrate".

4) Rinse the electrode in deionized water. Wipe the electrode with a kimwipe.

5) Place the probe in the conductivity standard (12.9 mS/cm or 1413 µS/cm).

6) Select one of the following options for calibration: Manual, Direct or Auto.

   For manual calibration: The screen will display the cell constant on the bottom
   line and the conductivity value on the middle line. Change the cell constant value
   until the displayed conductivity value matches the value of the conductivity
   standard at the measured temperature. To change the cell constant, press "Digits"
   → scroll to change the value → "Digits" to save and move to the next digit.

   For Direct Calibration: Wait for the **mS/cm** or **µS/cm** icon to stop flashing.
   Repeat the following for each digit of conductivity: press "Digits" → scroll to
   change the value → "Digits" to save and move to the next digit, repeat until the
   displayed conductivity value matches the value of the conductivity standard at the
   measured temperature.

For Auto Calibration: Wait for the **mS/cm** or **µS/cm** icon to stop flashing. The meter will display the temperature corrected value of the conductivity standard.

7) Press "calibrate" to set another calibration point. Repeat steps 4 to 6. When finished with calibration points, press "measure" to save the calibration.

8) For measurements, repeat step 4 and place the electrode in the solution.

9) Press "Line select" until the arrow icon is pointing to the conductivity measurement line.

10) Wait for the **mS/cm** or **µS/cm** icon to stop flashing and record the value.

Distance calibration between the electrodes using conductivity

1) Place the porous plates inside the chamber.

2) Insert the electrodes through the center holes of the porous plates. Make sure they protrude slightly from the surface of the porous plates by adjusting the electrode screws.

3) Make the PBS solution from PBS tablet and measure the conductivity of the PBS solution with conductivity meter. Fill the chamber with PBS solution. Make sure there are no bubbles between the electrodes.

4) Configure the KEITHLEY 2400 sourcemeter :

    i.   Turn on source meter.

    ii.   Press "Config" → "Ω"→ Sense-mode→ four-wire.

    iii.   Press "Config" → "Ω"→ Offset-compensation→enable.

    iv.   Press "Config" → "Ω"→ Source → manual.

5) Using the four-wire sense setting described in the sourcemeter manual as a reference. Connect each "4-WIRE SENSE" terminal (on the sourcemeter panel) from the sourcemeter to the Ag/AgCl electrode. Connect "INPUT/OUTPUT" terminal (on the sourcemeter panel) to the electrode adjustment screw in upstream chamber. Connect the other terminal to the downstream chamber.

6) Set the output current to 10 μA.

7) Turn on the output for few seconds and record the resistance value.

8) Calculate the value of conductivity using the equation below:

$$\chi = \frac{h}{\Omega A}$$

where χ is PBS conductivity, Ω is resistance, h is thickness (or the distance between

electrodes), and A is the effective area (which is 50% with porous plates).

For example, the calibration values are:

χ = 15.9 mS/cm, h = 0.075 cm and A = 0.141 cm^2 (diameter = 6mm)

Replacing the values above in the electrical conductivity equation, the resulting resistance value is 33.45 Ohms.

9) Adjust the electrode screws to a position where the resulting resistance reaches the desired value (ex., with this setup it is 33.45 Ohms).

Conductivity Testing Protocol

1) Place the sample in the O-ring.

2) Fill the downstream and upstream chambers with PBS.

3) Measure the resistance (Ω) of sample with the KEITHLEY 2400 sourcemeter.

4) Continue measuring the resistance in intervals of 10 minutes until the sample reaches equilibrium and the resistance remains constant for two consecutive measurements.

Streaming Potential and Hydraulic Permeability Testing Protocol

1) Turn on the KEITHLEY6514 system electrometer, and push "ZCHK" button. Then measure the voltage on two Ag/AgCl electrodes with KEITHLEY6514 system electrometer.

2) Connect one of the quick-disconnect of the upstream chamber with Hamilton three-way valve.

3) Use a 10 ml syringe to fill the upstream chamber with PBS. Check the tubing and the chamber for air bubbles and gently tap the sides to release them.

4) Connect the other quick-disconnect of upstream compartment to upstream pressure transducer.

5) Connect the top quick-disconnect of downstream chamber to the downstream pressure transducer. Connect the other quick-disconnect of the downstream chamber with Hamilton three-way valve.

6) Use a 10 ml syringe to fill the downstream chamber with PBS. Check the tubing and the chamber for air bubbles and gently tap the sides to release them. Connect the electrometer to the electrodes and turn on voltage measurement. Leave the flow meter connection port open to the air until the sample reaches equilibrium (voltage must be maintained at 0.01 mV for 10 minutes).

7) Connect a 500 µl Hamilton airtight syringe to flow meter.

8) Turn on the flow meter software (Sensiview). Change the sampling rate to 1.5625 Hz, and then click start.

9) Place the syringe into the syringe pump apparatus and set the flow rate.

   a. Syringe Pump Operation:

      i. Turn on syringe pump main power switch located on the rear panel.

      ii. Press "Set" → "Diameter", and then enter the diameter of the syringe being used in millimeters, or choose the syringe from the pump by pressing "Diameter" for 3 seconds. The list of syringe will show up, and then press "enter" to select the desired syringe.

      iii. To select the infuse rate by pressing "Set" → "Infuse Rate".

      iv. Press "Run/Stop" to begin infusion.

10) Run the flow meter first at 6 µl/min.

11) Stop infusion till the PBS comes out from flow meter.

12) Connect the flow meter to downstream chamber on the red fitting.

13) Close the three-way Hamilton valve on the downstream chamber.

14) Using the 10 ml syringe on the upstream to pressurize the chamber until the differential pressure between up and downstream compartments reaches 15 psi.

15) Close the three-way valve connecting the upstream chamber.

16) Fill a 500 μl Hamilton airtight syringe with PBS and connect it to upstream three-way valve.

17) Place the syringe into the syringe pump apparatus and set the flow rate.

18) After setting the flow rate, slowly open the three-way valve connected to the syringe. Begin infusion.

19) Observe the changes in pressure from the two transducer readouts. Adjust the rate of infusion so that the pressure differential remains constant at approximately 15 psi. Once the pressure differential has remained constant (± 0.01 psi) for 10 minutes, the correct infusion rate has been achieved. If the pressure readings do not stabilize, check the chamber for leaks at the valve connection sites.

20) Note the potential difference, pressure difference and the flow meter measurement.

21) Calculate streaming potential (Ag/AgCl electrodes voltage difference) as the potential difference between readings at steps 2) and 19).

22) Calculate the hydraulic permeability, k, using the equation below

$$k = \frac{Qh}{\Delta pA}$$

where Q is volumetric flow rate (flow meter reading), h is thickness, Δp is pressure difference, and A is effective area (50% of the sample area with porous plates).

23) Calculate the fixed charge density of tissue from following equations:

$$\Delta\psi = \frac{-F_c c^F k \Delta\Delta}{\chi}$$

where F_C is Faraday constant, c^F is fixed charge density,

24) Calculate the water volume fraction of tissue from following equations:

$$\chi = \frac{F_C^2 \Phi^w \left(C^+ D^+ + C^- D^-\right)}{RT}$$

where Φ^w is volume fraction of water, C^+ is the cation ion concentration and C^- is the anion concentration.

For negative charged tissues:

$$C^+ = C^- + C^F$$

The ion concentrations within the tissues can be calculated using the ideal Donnan equation.

$$C^+ = \frac{C^F + \sqrt{\left(C^F\right)^2 + 4C^{*2}}}{2},$$

$$C^- = \frac{-C^F + \sqrt{\left(C^F\right)^2 + 4C^{*2}}}{2}$$

Sample Preparation: Tissue

1) Select a section of meniscus tissue to extract a sample from. Allow to defrost slightly for 10 minutes at room temperature.

2) Place the tissue in a plastic weigh boat and place on the drill press stage. Mount a 9.5 mm dye-punch into the drill press chuck. The procedure does not require the

drill press to be turned on. Slowly, but forcefully, lower the dye and plunge through the desired section of tissue.

3) Remove the tissue sample from the dye and set aside.

4) Prepare the microtome for reducing the sample thickness. The sample dimensions for this experiment are diameter = 6 mm and thickness = 0.95 mm.

    a. Microtome Operation:

        i. Turn on water faucet connected to microtome cooling tubes.

        ii. Move the power knob ¾ to the right, increasing the current to 12 A.

        iii. Move the cutting blade guards aside and release the sliding stage lock.

        iv. Pour a small, dime-sized amount of embedding matrix on the stage and allow it to freeze. Once frozen, adjust the height of the stage and cut the embedding matrix until there is a flat plane.

        v. Using the digital current-sensing micrometer, measure the maximum height of the tissue sample.

        vi. Place the sample tissue on this flat plane and adjust the height of the stage so that the tissue is below the blade. Pour enough embedding matrix to completely cover the tissue. Wait until the tissue is frozen to begin cutting.

        vii. Using the adjustment dial on the right side of the microtome, set the cutting height to 40 microns.

        viii. Calculate the height of tissue to be removed. Then calculate how many 40 micron cuts are necessary to reach the desired height.

ix. Begin cutting the frozen specimen until you can see that you have begun cutting tissue. Once this point is reached, cut 80% of the calculated tissue to be removed.

x. Defrost the microtome stage by holding down the silver defrost switch. Remove the tissue and place it in the weigh boat.

xi. Prepare a new flat plane as described in step iv.

xii. Place the side of the tissue that was just cut (it should be flat) face-down onto the flat plane.

xiii. Adjust the height of the stage and cut until the tissue is reached, as in step ix.

xiv. Cut the remaining 20% of the calculated tissue to be removed.

xv. Defrost the stage, place the sample in the current-sensing micrometer and confirm that it is the correct height.

xvi. Move the power knob counter-clockwise to turn off the voltage, clean any tissue that may have been cut, replace the blade guard, and turn off the water faucet.

xvii.

Water volume and sulfated glycosaminoglycan (GAG) content measurements Protocol

1) Take sample out of the chamber.

2) Measure the volume fraction of water using the density determination kit (Sartorius).

3) Calculate water volume fraction (Φ^w) using equation below:

$$\Phi^w = \frac{W_{wet} - W_{dry}}{W_{wet} - W_{solution}} \frac{\rho_{solution}}{\rho_w}$$

where W_{wet} is the wet weight of the specimen, $W_{solution}$ is the weight of the specimen measured in solution, W_{dry} is the dry weight (from lyophilization), $\rho_{solution}$ is the mass density of solution (1.005 g/ml for PBS solution) and ρ_w is the mass density of water.

4) Lyophilizer operation instruction:

    i. Turn on the Centrivap Concentrator and place the sample in. (Tubes with samples should be opened when place in the Centrivap Concentrator.)

    ii. Close the Centrivap Concentrator and press "Run/Stop".

    iii. Close the Centrivap Cold Trap lid and make sure it's tight.

    iv. Close the Centrivap Cold Trap drain valve.

    v. Turn on the Centrivap Cold Trap power and wait for the indicator illuminator goes to "green" light (it takes around 10 mins).

    vi. Turn on the vacuum pump.

    vii. Turn off the vacuum pump first when the samples are ready to be taken out.

    viii. Open the Centrivap Cold Trap drain valve.

    ix. Press "Run/Stop" and open the Centrivap Concentrator.

    x. Open the Centrivap Cold Trap lid and clean the ice inside.

5) Digest lyophilizated sample for 24 hours at 60°C in 1ml papain solution.

    Papain solution contains:

100 mM sodium phosphate (NaH2PO4·H2O M.W.: 137.99)

10 mM EDTA (M.W.:372.24)

10 mM cysteine HCl (M.W.:157.6)

250 µg/ml papain

Therefore every 1 ml of solution must contain the following chemical quantities:

- sodium phosphate (NaH2PO4·H2O M.W.: 137.99): 0.0138 g

- EDTA (M.W.:372.24): 0.0037 g

- cysteine HCl (M.W.:157.6): 0.00158 g

- papain: 0.0025 g

6) Construct a standard curve using bovine chondroitin sulfate A.

Standard curve solution:

i. Make 1mg/ml Chondroitin A in Papain solution.

ii. Dilute to 200 µg/ml Chondroitin A in Papain solution using Papain solution.

7) Mix 100 µl of the papain-digested sample and 2ml of dimethylmethylene blue dye solution (DMMB) in a disposable cuvette and measure the GAG content spectrophotometrically at 525 nm.

DMMB solution:

    i.   Dissolve 4mg dimethymethylene blue (DMMB) in 1.25 ml 100%
ethanol. Mix it with a stir bar for at least 4 hours at room
temperature capped and wrapped in foil.

    ii.   Add the 0.76 g Glycine and 0.593 g NaCl to 200 ml DD H2O.

    iii.   Add the dissolved DMMB to solution.

    iv.   Add the 2.5 ml 1M HCl to solution. (To titrate solution to pH =
3.0±0.05)

    v.   Add DD H2O to solution until total volume of 250 ml is reached.

    vi.   Recheck pH=3.0.

    vii.   Filter the solution with Grade 2 filter paper into a brown bottle (or
bottle in foil). Label with date. Store it at room temperature in a
dark place.

8) Calculate c^F using equation below:

$$c^F = B \frac{W_{GAG}}{V_{water}}$$

where $B = \dfrac{2\,\text{mole charges}}{502.5\text{g GAG}}$, W_{GAG} is the GAG content in the sample, and V_{water} is the

volume of water in the sample.